Functional Magnetic Resonance Imaging

in Rhesus Macaque Monkeys

Thesis by

David J. Dubowitz

In Partial Fulfillment of the Requirements

for the Degree of

Doctor of Philosophy

California Institute of Technology

Pasadena, California

2002

(Submitted 9 April 2002)

Abstract

This thesis presents a method for functional magnetic resonance imaging in the brain of the rhesus macaque monkey, *Macaca mulatta*. Experiments were performed in an awake-behaving animal at 1.5 T in a conventional clinical magnetic resonance system. Strategies to train the animal within the MR environment and to ensure behavioral compliance are described. Limitations of studying macaque functional neuroanatomy at this magnetic field strength are also discussed. Methods to improve signal-to-noise beyond the scope of conventional BOLD imaging at 1.5 T are presented, including the use of very high magnetic fields for functional imaging (11.7 T), as well as novel methods to improve sensitivity using intravascular iron oxide contrast media. Using the techniques developed for this thesis, a series of studies are presented to examine the visual pathways in the primate brain, allowing direct comparison of functional neuroanatomy between nonhuman primates and human cortex. Although the two species are anatomically different, direct functional homology within the visual cortex is demonstrated.

Dedication

For my wife, Miriam, and our children Jennifer, Rebecca and Andrew.

Acknowledgments

If I have seen farther than others, it is because I was standing on the shoulders of giants.

- Sir Isaac Newton (1642-1727)

This thesis is a testimony to the teaching, encouragement and support of many colleagues. I am especially grateful to my advisor, Richard Andersen, who provided me with the opportunity, the resources and the guidance to do this work. None of this would have been possible without the unerring support of Bill Bradley, who saw a future for this research when many doubted it. I am also indebted to the other members of my thesis committee: Scott Fraser, Shinsuke Shimojo, Mark Konishi and Joel Burdick.

It has been my good fortune to work with many talented scientists in the field of MRI. I am particularly grateful to Dennis Atkinson, Rick Buxton, Eric Wong, Mike Tyszka, Eric Ahrens, Russ Jacobs and Dar-Yeong Chen from whom I have profited immensely.

My understanding of electrophysiology, neuroanatomy and the idiosyncrasies of primate behavior was enriched by close collaboration with John Allman, Betty Gillikin, Kelsie Weaver, Bradley Greger and John Pezaris. I am grateful to many other members of the Andersen Lab who gave freely of their time, but in particular, Cierina Marks and Viktor Shcherbatyuk.

During the latter part of this work, I have been especially lucky to have collaborated closely with Kyle Bernheim, a fellow physician scientist with the same love of MR sciences and incredulity over monkey noncompliance in even the simplest of tasks.

This work was supported in part by a generous fellowship grant from Huntington Medical Research Institutes.

Contents

List of Figures

List of Tables

Chapter 1 Introduction

1.1 Background

In 1845 Michael Faraday was the first to investigate the magnetic properties of blood. He almost certainly suspected a difference in the magnetic susceptibility properties between fresh and deoxygenated clotted blood and made a note to himself: "must try fluid blood." However, he did not complete his experiments. This fell instead to Linus Pauling who, almost a century later, noted differences in magnetic susceptibility as large as 20% between paramagnetic deoxyhemoglobin and diamagnetic oxyhemoglobin[1]. These variations in magnetic susceptibility are strong enough to impact the MR parameters T_1 and T_2. Using MRI, differences in relaxation parameters between fresh blood, deoxygenated clotted blood and hemoglobin breakdown products were used in clinical imaging to document the age and resolution of hematomas[2,3]. The discovery that made functional MRI possible was the observation by Ogawa[4] that small dynamic changes in susceptibility could be used to track perturbations in intravascular deoxyhemoglobin associated with neuronal activation. Earlier studies using positron emission tomography (PET) had demonstrated a large change in local blood flow and blood volume accompanying neuronal activity[5]. The hemodynamic change is disproportionately large compared with the metabolic needs of the neurons, and the net effect is to wash out deoxyhemoglobin from the venous side and increase the proportion of oxygenated hemoglobin. The term Blood Oxygen Level-Dependent (or BOLD) contrast was used to

describe this effect on MRI. Most imaging sequences for conventional MRI are designed to minimize the effects of bulk magnetic susceptibility. To observe the changes in deoxyhemoglobin, imaging sequences need to be particularly sensitive to perturbations in magnetic susceptibility. These susceptibility effects are exaggerated at high magnetic field or by using gradient echo imaging techniques, particularly, "fast" gradient echo techniques. Since the first description of functional MRI, a large number of susceptibility-weighted imaging sequences have been proposed. These imaging sequences are also inherently sensitive to susceptibility artifacts unrelated to the hemodynamic changes (e.g., at tissue interfaces between bone, water, fat or air), thus the choice of sequence is frequently an empirical one, as is its optimization for a particular need. The same is true when optimizing sequences for monkey imaging. This thesis describes a series of studies to develop functional MRI as a neuroscience tool for studying macaque monkeys.

1.2 Overview

Most of our understanding about the primate brain comes from half a century of investigation in monkeys. Findings from lower primates have been extrapolated to attempt to explain the workings of the human brain. Invasive studies of the human brain are limited to those done as part of a diagnostic investigation for a particular clinical problem, or as intraoperative studies. By their nature, the subjects for these studies are not normal volunteers. Nonhuman primates thus provide an excellent model for studying human neurophysiology, particularly where direct (often invasive) studies are precluded

in normal human volunteers. The advent of functional MRI, hailed a safe, reproducible, noninvasive tool with which to study the human brain. To bridge the gap between neurophysiological studies (in monkeys) and imaging studies (in humans) we need an intermediate step. This is where there is a specific need for functional imaging studies in monkeys to allow direct comparison with similar imaging studies in humans, and to allow direct comparison with invasive neurophysiology studies in monkeys. Chapters 2–5 describe studies I performed in developing functional MRI in monkeys. These 4 chapters have been published in peer reviewed journals[6-9]. This thesis also contains three appendices. The appendices are unpublished work, but parts have appeared in conference proceedings[10,11].

Chapter 2 outlines many of the technical difficulties in using a conventional clinical scanner for imaging monkeys. This was the first demonstration of stimulus-correlated functional magnetic resonance activation in a macaque monkey. This was significant as previous studies in anesthetized animals had suggested the BOLD signal would be too small for useful functional MRI in monkeys at 1.5 T. There is significantly larger BOLD signal in the absence of anesthetic agents. Prior to this paper, all animal imaging had been done in unconscious animals. This paper showed that the functional MRI was indeed possible in an awake animal. It also demonstrated that a monkey could be acclimated to the MRI environment. In particular that useful maps of functional brain activation could be achieved with the monkey in a prone "sphinx" position, obviating the need for him to be sitting upright (as was the conventional wisdom). While this imposes some constraints with respect to studies of motor function (an animal weight bearing on all 4 limbs is not

so readily able to move them in response to a stimulus), the setup is excellent for studies of visual cortex. This paper provided optimization strategies for both the RF hardware and the imaging pulse sequences for ensuring maximum signal-to-noise ratio (SNR) for monkey imaging.

The third chapter addresses the strength of functional MRI as a noninvasive technique to compare patterns of cortical activation in humans and in nonhuman primates. One of the strengths of functional MRI in monkeys will be to integrate patterns of functional MR activation with the underlying neuronal firing. To bridge the gap between fMRI in humans and direct electrophysiological recordings of neuronal activation in monkeys, we face two challenges. Firstly, we are comparing two very different techniques in terms of their spatial and temporal capabilities, and in terms of the physiological parameters that they are sensitive to. We are also comparing across two different species. This chapter addresses the second part where we compare patterns of functional activation using identical techniques, but in two different species. This paper described the first study of visual cortex activation across species using functional MRI. Using an animated cartoon movie as a visual stimulus, homologous areas of activation are demonstrated in both human and monkey visual cortex.

The next two chapters address the difficulty in achieving high-resolution images in a conventional 1.5 T MRI scanner, and explore ways to improve on this. One of the goals of functional MRI is to achieve comparable resolution to more invasive neuronal recording techniques. In practical terms this would require robust imaging at resolution at

or better than the level of the cortical column. The cortical column is the building-block of cerebral architecture. All neurons within a cortical column share common features in terms of tuning, specialization, and function. Thus, imaging at resolutions that are worse than a single column will tend to superimpose the activation from many differing neurons and the signal becomes less coherent. Imaging a single cortical column is a good representation of the activity of individual neurons within the column. In practical terms this requires a resolution of about 200 μm. This dimension is an order of magnitude smaller than typical fMRI studies at 1.5 T (and the 3-dimensional imaging voxel needs to be three orders of magnitude smaller). An improvement in voxel resolution requires a similar improvement in SNR. Increasing the number of measurements is one approach to increasing SNR; however using conventional BOLD imaging at 1.5 T would require 6 orders of magnitude increase in imaging times to preserve the SNR per voxel. A five-minute study would take more than 10 years (not a practical solution for awake animal imaging). The use of dedicated surface coils and low noise amplifiers goes a long way to increasing the available signal. Other strategies are to address alternate contrast mechanisms to BOLD or to use a much higher applied magnetic field.

The fourth chapter outlines a novel method I developed for functional MRI in monkeys using intravascular magnetite. Magnetite is considerably more paramagnetic than deoxyhemoglobin (the basis of BOLD contrast). Comparisons of this technique with conventional BOLD functional MRI revealed a 3-fold improvement in contrast-to-noise in the primary visual cortex using the magnetite agent. This improved SNR can be used to improve resolution.

The fifth chapter investigates the viability of functional MRI at very high static magnetic field. This is a study of functional MRI at 11.7T - an order of magnitude increase in static magnetic field over conventional clinical imaging, and allows imaging resolution for fMRI of 180 μm (i.e. sufficient for cortical column functional MRI). Engineering constraints limit the size of the MR scanner at this magnetic field strength. These studies were performed using a vertical MR scanner with a usable bore of 30 mm. The animal model for this study was a mouse, using a somatosensory stimulus to the hind paw. These studies represent the first fMRI measurements at this very high magnetic field strength, as well as the first successful fMRI studies in mice.

Appendices A and B outline some of technical developments necessary for the studies in chapters 2–4. To ensure that the neuronal activity recorded in an electrophysiology setup is the same as that producing functional MRI activation measured during an MRI experiment, it is necessary to carefully control both the stimulus as well as the behavioral response of the animal. A number of technological developments were needed to keep the animal immobilized in the scanner, to check appropriate responses (in this, case eye position), and to reward the animal while in the MR scanner. The materials and devices specifically designed to achieve this are presented in Appendix A.

Appendix B describes methods designed for co-registering electrophysiology and functional MRI data. As described above, in bridging the gap between human functional MRI and monkey electrophysiology, one of the important comparisons to be made is between direct recordings of neuronal activity and functional MRI changes in the same

animal under the same experimental and behavioral conditions. There are two approaches to this. One is to make simultaneous electrophysiology and fMRI measurements while the animal is in the MR scanner. This is technologically very challenging as the material requirements for the two techniques are very different. Functional MRI is very sensitive to gross magnetic susceptibility artifacts introduced by external devices, for example, recording electrodes. Similarly, electrophysiology recordings are best achieved in an electrically and magnetically shielded environment, rather than in the presence of strong oscillating magnetic fields and eddy currents found inside an MR scanner. The second approach is to perform both investigations separately in their own optimum environments. For the data to be comparable, the two studies must be accurately co-registered. Appendix B outlines the techniques I developed specifically for this.

Appendix C lists the abbreviations used in this thesis.

1.3 References

1. Pauling, L. and Coryell, C. D. The magnetic properties and structure of hemoglobin, oxyhemoglobin and carbonmonoxyhemoglobin. *Proc. Natl. Acad. Sci. USA* **22**, 210-216 (1936).

2. Clark, R. A., Watanabe, A. T., Bradley, W. G., Jr. and Roberts, J. D. Acute hematomas: effects of deoxygenation, hematocrit, and fibrin-clot formation and retraction on T2 shortening. *Radiology* **175**, 201-6. (1990).

3. Bradley, W. G., Jr. MR appearance of hemorrhage in the brain. *Radiology* **189**, 15-26. (1993).

4. Ogawa, S., Lee, T. M., Kay, A. R. and Tank, D. W. Brain magnetic resonance imaging with contrast dependent on blood oxygenation. *Proc. Natl. Acad. Sci. USA* **87**, 9868-9872 (1990).

5. Fox, P. T. and Raichle, M. E. Focal physiological uncoupling of cerebral blood flow and oxidative metabolism during somatosensory stimulation in human subjects. *Proc. Nat.l Acad. Sci. U SA* **83**, 1140-4. (1986).

6. Dubowitz, D. J. et al. Functional magnetic resonance imaging in macaque cortex. *Neuroreport* **9**, 2213-2218 (1998).

7. Dubowitz, D. J. et al. Direct comparison of visual cortex activation in human and nonhuman primates using functional magnetic resonance imaging. *Journal of Neuroscience Methods* **107**, 71-80 (2001).

8. Dubowitz, D. J. et al. Enhancing fMRI contrast in awake-behaving primates using intravascular magnetite dextran nanoparticles. *Neuroreport* **12**, 2335-40 (2001).

9. Ahrens, E. T. and Dubowitz, D. J. Peripheral somatosensory fMRI in mouse at 11.7 T. *NMR Biomed.* **14**, 318-24. (2001).

10. Dubowitz, D. J., Martinez, A. and McDowell, J. A simple setup for tracking eye position during fMRI. *Proc. of. Int. Soc. Magn. Res. Med.* **3**, 1691 (1999).

11. Pezaris, J. S. and Dubowitz, D. J. MRI Localization of Extracellular Electrodes Using Metallic Deposition at 1.5 T. *Proc. of. Int. Soc. Magn. Res. Med.* **2**, 968 (1999).

Chapter 2 Magnetic Resonance Imaging in Macaque Cortex

This chapter describes the first experiments using fMRI to study functional neuroanatomy in an awake-behaving macaque monkey. It represents the first ever demonstration of stimulus-correlated functional magnetic resonance activation in a macaque monkey. This is significant, as previous attempts by other investigators in anesthetized animals had suggested there was insufficient BOLD signal at 1.5 T to allow meaningful studies. The current set of experiments were performed in an awake animal, habituated to the noise of the scanner, and trained to watch a stimulus, while remaining still within the MR scanner. This paper was important in demonstrating that functional MRI in macaque monkeys was indeed possible, and could be developed as a valuable neuroscience tool.

2.1 Abstract

The ability to use fMRI in a monkey model would bridge the gap between the fMRI demonstration of cerebral activation in humans and the cumulative wealth of monkey data on the functional organization of the brain from single electrode mapping, radio-isotope and histology studies. We report a new technique for fMRI in an awake co-

operative rhesus macaque (*Macaca mulatta*) in a conventional clinical 1.5 T MR scanner and present the first fMRI images from a macaque. Good resolution, signal-to-noise ratio and BOLD response (2.6-4.6%) have been achieved using the manufacturer's standard volume knee coil. T_1 values of macaque gray and white matter (1490 ms, 1010 ms respectively) are higher than those in human brain, whereas T_2 values are lower (55 ms, 48 ms respectively). An MR-compatible design for restraining the monkey is also described along with a suitable EPI sequence for BOLD images, optimized for monkey T_2, with voxel sizes from 29-65 μl, and MPRAGE sequence for anatomical studies with 0.8 mm isotropic resolution, optimized for monkey T_1.

2.2 Introduction

The advent of blood oxygen level dependent (BOLD) contrast and Functional Magnetic Resonance Imaging (fMRI)[1] has provided a new noninvasive technique in behavioral neuroscience for studying brain function. This technique has seen much development in medical and neuroscience application in human subjects[2-6]. However, the necessity of a co-operative and motionless subject has, to-date, prevented a monkey model for awake fMRI from being realized. fMRI studies in anesthetized animals offer only limited value in behavioral neuroscience.

Rhesus macaques (*Macaca mulatta*) are readily trained to perform complex tasks for reward and have formed the basis of much of our understanding about primate visual pathways. There is a wealth of knowledge on the macaque visual cortex from

microelectrode mapping, radioisotope tracers and anatomical studies[7-16]. The ability to perfect a nonhuman primate model for fMRI studies would lead to better understanding about the complex relationship between cerebral fMRI activation (a blood flow change) and the underlying cortical activation (an electrical event). It would also provide a new noninvasive tool to study functional neuroanatomy and CNS interconnections in the nonhuman primate brain, and allow a more direct comparison with their human homologues. In this report we describe a new technique for performing functional magnetic resonance imaging in awake, co-operative, rhesus macaques in a conventional 1.5 T clinical MRI scanner[17], and present the first fMRI images from macaque brain.

2.3 Materials and Methods

2.3.1 Animal Model

All studies were performed in a healthy, 4.5 kg, 4-year-old male rhesus macaque. Approval for this research was obtained from the Institutional Animal Care and Use Committee, and Epidemiology and Biosafety Committees. The monkey was trained to lie prone with his head erect ("sphinx" position) in a mockup of the bore of a clinical MR scanner. His head was restrained by means of a custom-built MRI-safe headcap. The monkey was trained to look at a viewing screen placed 200 cm in front of him, allowing +/- 12 degrees field of view (Figure 2.1). For the data presented in this report the monkey

was required only to look passively at the screen. During initial training within the MRI, a small dose of acepromazine (50 μg/kg i.m.) was occasionally needed to reduce anxiety in the monkey. With further training this was usually not required.

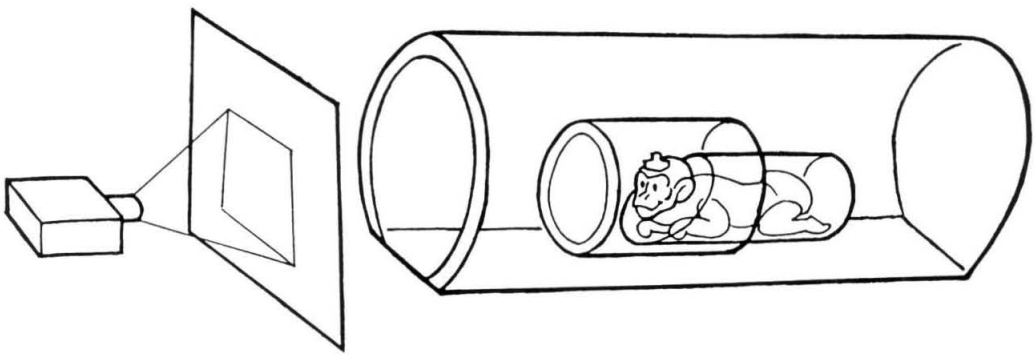

Figure 2.1 The monkey lies within the MRI in a sphinx position, with his head restrained in the RF coil. A visual stimulus is provided by a video projector on a screen at the opening to the MRI bore.

2.3.2 Stimulus

A visual stimulus was provided using an LCD video projector connected to a PC computer. For the experiments presented in this report, a 4-minute sequence of animated film, chosen to include rapidly changing colors, contrast levels, faces and movement (*Aladdin*, Walt Disney Company.), was presented to the monkey in 25 seconds clips. Each film clip was preceded by a period of complete darkness for 25 seconds. The 50-

second cycle was repeated 4 times plus an additional period of 25 seconds darkness at the end (Figure 2.2). At the conclusion of each experiment, the monkey was rewarded with sugar water.

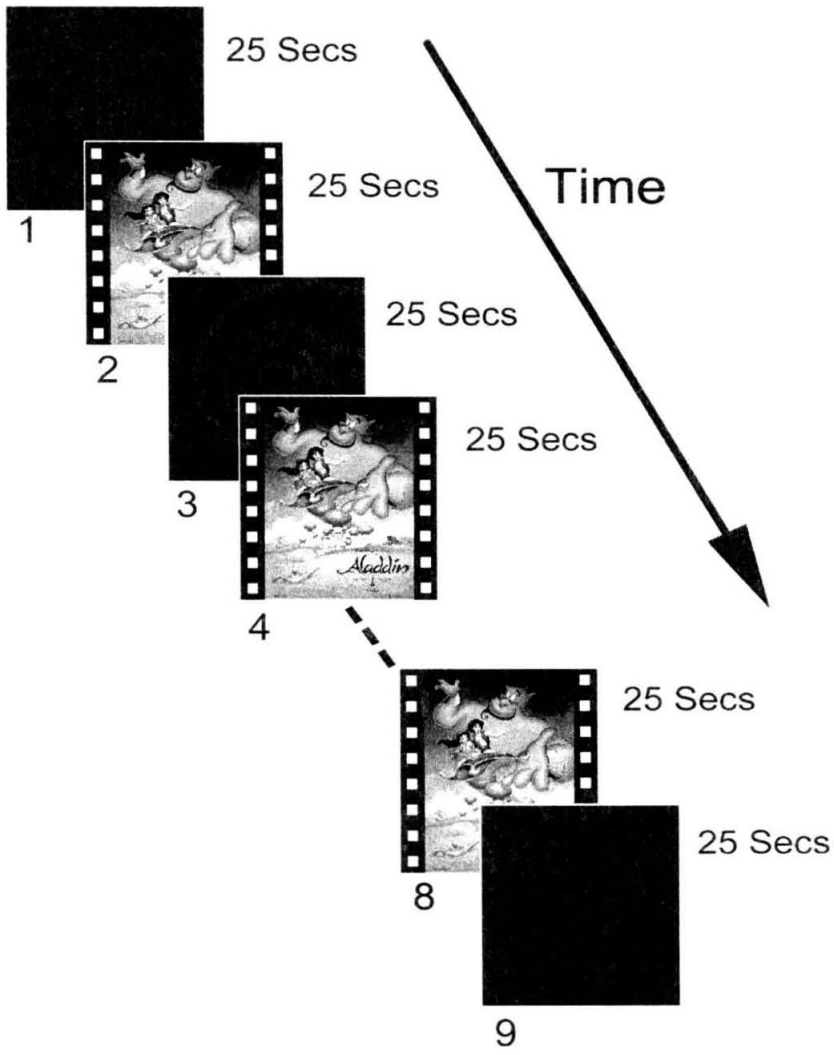

Figure 2.2 The visual stimulus comprised 25 seconds of animated movie alternated with complete darkness.

2.3.3 Surgical Technique and Experimental Setup

The monkey's head was held motionless for the duration of the experiment by means of a custom-built plastic headcap, which was surgically attached under general anesthesia. Details are shown in Figure 2.3. The screws and central post were constructed from machined polyetherimide. Four screw heads were positioned epidurally by means of a key-hole shaped trephine in the skull and secured with nylon nuts. The central post was positioned with the monkey's head held in a stereotaxic frame (Kopf Instruments), with its long axis parallel to the z-axis of the head (cranio-caudal direction). The screws and headpost were secured to each other with a polymethylmethacrylate headcap fashioned insitu. The scalp was closed in layers around the headcap.

The monkey was transported to the MRI facility in an MR-safe plastic travel cage which had been modified to allow continuous filtered air flow. An acrylic (Plexiglas) tube was attached to the transport cage, and the monkey then crawled into the tube, from which only his head protruded. The acrylic tube with monkey was then positioned in the MRI machine. The head post was secured to the window in the receive/transmit coil of the MRI with a 2-part headpost locator machined out of glass-filled phenolic (Figure 2.3). This allowed the head to be secured during experiments, but could be loosened to allow the monkey to raise or lower his head freely between experiments for comfort. A circular spirit level on the locator ensured experiments could be repeated with the head in the same position. The monkey wore a diaper for the duration of the study, and all areas with which the monkey could come into contact were covered in polythene sheet.

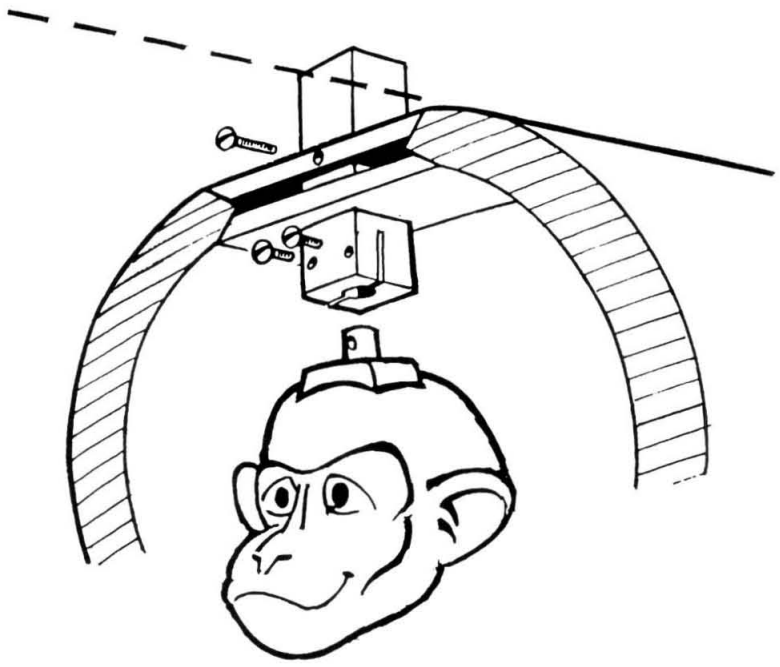

Figure 2.3 Cross section through the RF coil showing details of the monkey's headcap with headpost and the headcap locator.

2.3.4 MR System

All imaging was done on a conventional 1.5 T Siemens VISION MR scanner equipped with 25 mT/m gradients employing 300 μsec rise times. Signal-to-noise ratio (SNR) characteristics were measured for 3 different coils supplied with the MR scanner; circularly polarized (CP) transmit/receive head coil (26 cm diameter), CP transmit/receive knee coil (19 cm diameter), and a receive-only flexible surface coil (37 x 17 cm). For our purposes it was preferable to be able to examine the whole head.

Optimum coverage, SNR and coil loading were best achieved with the CP knee coil (see results).

Spin-echo T_1 and T_2 weighted images were performed with varying repetition (TR) and echo times (TE) in order to calculate T_1 and T_2 of macaque gray matter and white matter (TE=22, 60, 120 msec, TR=300, 600, 900, 1200, 1500 msec).

Anatomical imaging was done with a 3-D Magnetization-Prepared Gradient Echo (MPRAGE) sequence. The T_1 values of monkey cortex were used to simulate approximate parameters[18]. The sequence was further optimized empirically for tissue contrast via a series of algorithmic models. Optimal parameters were found to be TR/TE = 11.4 / 4.4 msec, flip angle 12 degrees, inversion time (TI) 250 ms and delay time (TD) 600 ms. A 100 mm field of view (FOV) was acquired onto a 128 x 128 matrix, giving an isotropic resolution of 0.8 mm. 100% oversampling was used in the phase, read and slab directions to reduce "wrap" artifacts and increase SNR. The total acquisition time was 13 minutes.

For BOLD weighted images, a low bandwidth (833 Hz/pixel) echo-planar (EPI FID) sequence was found to give the best resolution, allowing a FOV as low as 140 mm to be collected onto a 128 x 128 matrix. TE of 40 msec was chosen to approximate the T_2 of monkey cortex for maximal functional contrast[19]. Eight coronal slices of 3 mm were collected in the monkey's occipital cortex per repetition of 2500 msec. Ninety-five repetitions of the 8 slices were acquired, the whole run taking less than 4 minutes. The

first 5 repetitions were included to ensure steady state and were not used in data analysis[19]. Optimum voxel size was determined empirically to allow maximum SNR per pixel without excessive partial volume averaging. The monkey's head was positioned at the center of the radio frequency (RF) coil for maximum SNR. This caused asymmetry in the coil loading, and the need for local shimming, which was achieved using an experimental volume-shim algorithm[20].

2.3.5 Image Processing

The time-dependent echo-planar images were processed off line on a Sun/Sparc workstation with AFNI software[21]. Functional images were generated using a cross-correlation technique[19]. A series of phase-shifted trapezoids were used as the reference waveforms (Figure 2.4). Each trapezoid function was correlated on a pixel-by-pixel basis with the time course series by a least-squares fit. Functional images were generated with intensity representing the magnitude of the best fit. Gram-Schmidt orthogonalization was used to remove linear drift in the time series[19]. To remove spurious pixels, the functional intensity map was thresholded at a correlation-coefficient value of 0.61 ($p < 1x10^{-5}$ Bonferroni corrected for multiple comparisons). Only pixels belonging to a nearest-neighbor cluster of at least 3 significant pixels were displayed. Images were manually checked for in-plane motion. In the data presented, no in-plane spatial registration was needed. MPRAGE and functional images were co-registered using AFNI software.

Post-processing of spin-echo images for tissue contrast optimization was done using NIH-Image software (U.S. National Institutes of Health, http://rsb.info.nih.gov/nih-image/). Ten regions of interest were drawn around anatomically gray and white matter for each value of TE/TR. To calculate T_1 and T_2 values, mean signal (S) for gray and white was fitted to the relaxation curve:

$$S = S_o e^{TE/T_2} (1-e^{-TR/T_1}) \qquad [1]$$

NIH-Image was also used to calculate SNR characteristics of the 3 coils. Pixel values were combined for 6 regions of interest in a mid-coronal slice from a MPRAGE dataset, and compared with background (air) noise for each coil. Mean SNR values for each coil were calculated.

2.4 Results

Relative SNR calculations for 3 standard RF coils are shown in Table 1. The knee coil was the preferred coil for monkey imaging, having almost double the SNR characteristics of the head coil and a 50% improvement over the flex coil.

Measured values of T_1 and T_2 relaxation times for macaque cortex are shown in Table 2. The T_2 values are lower than in humans, and the T_1 values higher. These T_1 and T_2 values

were used as a first approximation in optimizing the MPRAGE and BOLD weighted sequences respectively.

	ROI	Area	MR Signal	Relative SNR
Head coil	brain	379	181.82 ±12.17	**7.6**
	background	5000	23.89±5.92	
Knee coil	brain	408	227.76±11.66	**14.8**
	background	5000	15.41±4.34	
Flex coil	brain	435	111.85±7.02	**9.9**
	background	5000	11.29±3.06	

Table 2.1 Signal-to-noise measurements for three standard Siemens RF coils; circularly polarized head coil, circularly polarized knee coil, and surface flex coil. Measurements made in regions of interest (ROI) including both gray and white matter in a mid-coronal slice. Noise measurements made in the air signal in the periphery of the image. Areas are measured in pixels, mean signal and standard deviation are in arbitrary intensity units.

	GM	WM
T_1 (msec)	**1490** (920)	**1010** (790)
T_2 (msec)	**55** (101)	**48** (92)

Table 2.2 T_1 and T_2 values for macaque brain (typical values for human brain are shown in parentheses).

The functional intensity maps are presented in Figure 2.4. Areas of fMRI activation are clearly seen as discrete areas of activation in the primary visual cortex, and extra-striate visual cortex. These show high correlation with the presented visual stimulus. The fMRI response for 3 runs using differing voxel sizes of 29.4 μl (3.13 x 3.13 x 3 mm), 45.9 μl (3.91 x 3.91 x 3 mm) and 61.2 μl (3.91 x 3.91 x 4 mm) are shown in Figure 2.5. Functional signals at these voxel sizes (as a percentage modulation of the MRI signal) were 4.6%, 2.6%, 3% respectively.

2.5 Discussion

This technique provides high-resolution images of discrete areas of fMRI activation which are comparable to existing visual fMRI studies in humans, but which have not previously been possible in monkeys. Areas of activation are recognizable in primary and extra-striate visual cortex. This has been achieved using a standard Siemens RF volume coil. The volume knee coil was found to provide the best SNR characteristics for imaging monkeys. It also provided a convenient anchor point for our headpost locator. While surface coils may improve signal-to-noise in imaging the occipital cortex, other practical matters mitigated their use; the large size of the standard Siemens flex coil made it more difficult to use with monkeys and optimum coverage of the whole brain was also difficult.

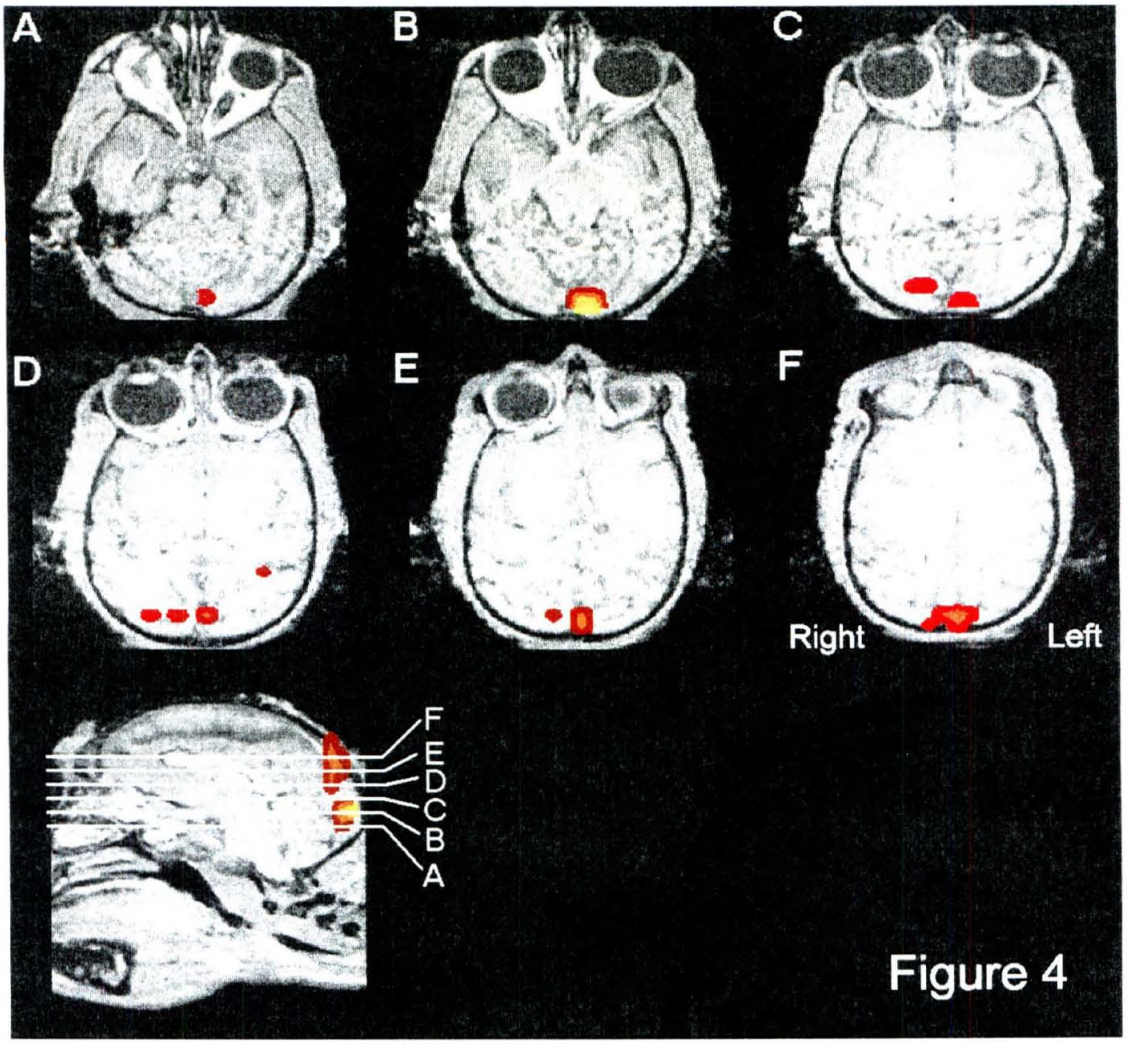

Figure 2.4 Areas showing significantly increased MR signal during the 25-second movie clip compared with total darkness. Anatomical background image has 0.8 mm isotropic resolution. Functional overlay has pixel dimensions 3.91 x3.91 x 3 mm. The positions of the axial slices A-F are shown on the sagittal slice. The unusual ghosting artifact is due to the monkey twitching his ears (not usually seen in human studies), which has since been rectified with a headband.

Better signal-to-noise characteristics are achievable with such a coil in a larger subject (e.g., a human head) particularly areas of cortex that are geometrically closer to the coil (E.C. Wong - personal communication). While some improvement in signal-to-noise may be possible with a custom designed RF volume coil, the added cost and technical expertise for this can be considerable. Our observed BOLD signal change of 2.6-4.6% is comparable with the 1.5-5% change observed in human studies[19].

The percentage modulation of the MRI signal is not a good measure for optimizing voxel sizes; at smaller voxels the high noise may artificially elevate the observed percentage change. With increasing voxel size SNR increases, but the baseline MRI signal may also change unpredictably due to partial volume averaging. Empirically a voxel size from 29.4 to 45.9 μl was preferred, providing adequate SNR and BOLD response, while preserving spatial resolution. Beyond this size, BOLD response was still observed, but the anatomical location was poorly defined.

Functional activation in the left primary visual cortex (V1) showed higher functional intensity than on the right. In addition the area of activation in right and left V1 appear to be a few millimeters displaced craniocaudally. The reason for this discrepancy is not immediately apparent. No attempt has been made to correct for the inevitable warp of EPI images in the phase-encode direction (craniocaudal) by off-resonance effects[22]. The exact location of the activation as mapped onto the MPRAGE anatomical image may be displaced by up to 1-2 pixels. B-field mapping and further signal processing are required

if the area of visualized activation is to be more accurately transformed onto the MPRAGE image (although a 0.5 pixel warp is still inevitable[23]).

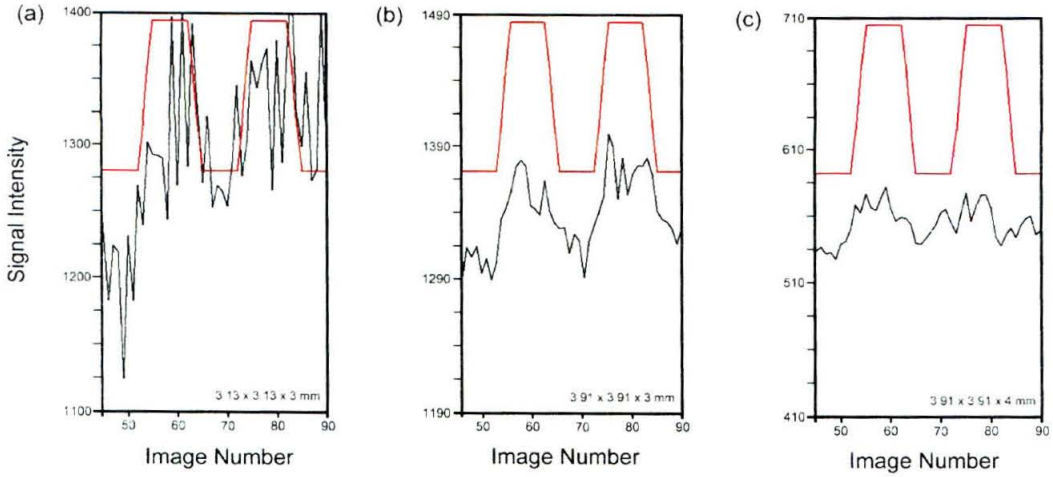

Figure 2.5 fMRI signal change with time for three different voxel sizes, each graph representing a typical active pixel in the occipital cortex. (**a**) 29.4 µl (3.13 x 3.13 x 3 mm), (**b**) 45.9 µl (3.91 x 3.91 x 3 mm) and (**c**) 61.2 µl (3.91 x 3.91 x 4 mm). The lower plot is the time-varying MR signal, the upper plot is the ideal trapezoid reference function of the stimulus vs. time used for correlation analysis. At 29.4 µl MR signal shows good correlation with the stimulus, but poor SNR. With voxel size increased to 45.9 µl and 61.2 µl, SNR improves but absolute BOLD signal diminishes due to partial volume averaging. Empirically optimum voxel size to achieve good SNR and BOLD response is between 29 and 45 µl.

Another possible explanation for the asymmetrical distribution of activation may lie in the global physiological response to the stimulus used. Our paradigm was designed primarily to stimulate as much of the visual system as possible, thus some differential stimulation is to be expected, and has not been controlled for. In these early experiments, control over the animal's behavior was minimal. Thus it is possible that the monkey lapsed in concentration, perhaps becoming inattentive to all or part of the stimulus. The

monkey may also have fixated on a part of the image that caused asymmetrical stimulation of the visual fields. Alternatively, the part of the image that caught the monkey's gaze (a face, for example) may not have been the most potent V1 stimulus, with V1 receiving maximal stimulation from elsewhere in the image. Further studies are planned which include a more refined stimulus paradigm. For these more complex paradigms and for awake-behaving studies, we have developed an infrared system for real-time monitoring of eye position that will enable us to better answer these questions.

Polymethylmethacrylate is commonly used for head fixation in macaque electrophysiological studies, and was thus our first choice material in designing an MR-safe head restraint. Some susceptibility artifact and distortion were observed with polymethylmethacrylate *in vivo* at the high gradient strengths employed for the BOLD weighting. For the studies described here, this presented no problem as the headcap was mounted anterior on the skull and well removed from any areas imaged. To make the technique more versatile, a new modification in which the headcap and head post are all made from a single unit of polyetherimide (machined to the curvature of the monkey's skull) is being evaluated as an alternative for polymethylmethacrylate.

2.6 Conclusion

High-quality fMRI images in *Macaca mulatta* visual cortex have been produced using a conventional 1.5 T clinical MR scanner and a standard RF volume coil. The basic technique can be easily modified to allow imaging of other areas of the macaque cortex,

and, with further training, awake-behaving studies are also possible. This paves the way for fMRI to be extended to include the study of the nonhuman primate cortex. With direct correlation with macaque electrophysiological studies now possible, we may also be able to gain further insight into the nature of the fMRI response.

2.7 References

1. Ogawa, S., Lee, T. M., Kay, A. R. and Tank, D. W. Brain magnetic resonance imaging with contrast dependent on blood oxygenation. *Proc. Natl. Acad. Sci. USA* **87**, 9868-9872 (1990).
2. Tootell, R. B. et al. Functional analysis of human MT and related visual cortical areas using magnetic resonance imaging. *J. Neurosci.* **15**, 3215-30 (1995).
3. DeYoe, E. A., Bandettini, P., Neitz, J., Miller, D. and Winans, P. Functional magnetic resonance imaging (FMRI) of the human brain. *J. Neurosci. Methods.* **54**, 171-187 (1994).
4. Sereno, M. I. et al. Borders of multiple visual areas in humans revealed by functional magnetic resonance imaging. *Science* **268**, 889-893 (1995).
5. Stapleton, S. R. et al. Combined utility of functional MRI, cortical mapping, and frameless stereotaxy in the resection of lesions in eloquent areas of brain in children. *Pediatr. Neurosurg.* **26**, 68-82 (1997).
6. Mueller, W. M. et al. Functional magnetic resonance imaging mapping of the motor cortex in patients with cerebral tumors. *Neurosurgery* **39**, 515-520 (1996).

7. Andersen, R. A. Encoding of intention and spatial location in the posterior parietal cortex. *Cereb. Cortex* **5**, 457-469 (1995).

8. Snyder, L. H., Batista, A. P. and Andersen, R. A. Coding of intention in the posterior parietal cortex. *Nature* **386**, 167-170 (1997).

9. Andersen, R. A. Neural mechanisms of visual motion perception in primates. *Neuron* **18**, 865-872 (1997).

10. Hubel, D. H. and Wiesel, T. N. Receptive fields and functional architecture of monkey striate cortex. *J. Physiol. (Lond.)* **195**, 215-43 (1968).

11. Hubel, D. H. Exploration of the primary visual cortex, 1955-78. *Nature* **299**, 515-24 (1982).

12. Felleman, D. J. and Van Essen, D. C. Distributed hierarchical processing in the primate cerebral cortex. *Cereb. Cortex* **1**, 1-47 (1991).

13. Tootell, R. B., Switkes, E., Silverman, M. S. and Hamilton, S. L. Functional anatomy of macaque striate cortex. II. Retinotopic organization. *J. Neurosci.* **8**, 1531-1568 (1988).

14. Maunsell, J. H. The brain's visual world: representation of visual targets in cerebral cortex. *Science* **270**, 764-769 (1995).

15. Maunsell, J. H. and Newsome, W. T. Visual processing in monkey extrastriate cortex. *Annu. Rev. Neurosci.* **10**, 363-401 (1987).

16. Takechi, H. et al. Mapping of cortical areas involved in color vision in nonhuman primates. *Neurosci. Lett.* **230**, 17-20 (1997).

17. Dubowitz, D. J. et al. Functional MR neuroimaging in an awake-behaving macaque. *Proc. of Int. Soc. Magn. Res. Med.* **2**, 1417 (1998).

18. Epstein, F. H., Mugler, J. P., 3rd and Brookeman, J. R. Optimization of parameter values for complex pulse sequences by simulated annealing: application to 3D MP-RAGE imaging of the brain. *Magn. Reson. Med.* **31**, 164-177 (1994).

19. Bandettini, P. A., Jesmanowicz, A., Wong, E. C. and Hyde, J. S. Processing strategies for time-course data sets in functional MRI of the human brain. *Magn. Reson. Med.* **30**, 161-173 (1993).

20. Heid, O. H. Noniterative localized in vivo shimming in <15s. *Proc of Int Soc Magn. Res. Med.* **1**, 363 (1996).

21. Cox, R. W. and Hyde, J. S. Software tools for analysis and visualization of fMRI data. *NMR Biomed.* **10**, 171-178 (1997).

22. Farzaneh, F., Riederer, S. J. and Pelc, N. J. Analysis of T_2 limitations and off-resonance effects on spatial resolution and artifacts in echo-planar imaging. *Magn. Reson. Med.* **14**, 123-139 (1990).

23. Cox, R. W. AFNI: software for analysis and visualization of functional magnetic resonance neuroimages. *Comput. Biomed. Res.* **29**, 162-173 (1996).

2.8 Acknowledgment

We thank Chris Headrick for the illustrations, Antigona Martinez for assistance with functional image analysis, Yale Cohen and Boris Breznen for helpful discussion, Rick Paniagua for workshop and technical assistance, Sohaib Kureshi for surgical assistance. This research was supported by the National Eye Institute (RAA) and the Pasadena Neurosciences Fellowship of Huntington Medical Research Institutes (DJD).

Chapter 3 Direct Comparison of Visual Cortex Activation in Human and Nonhuman Primates Using Functional Magnetic Resonance Imaging

The true strength of nonhuman primate functional MRI as a neuroscience tool is to bridge the gap between functional MRI studies of the human brain and our insights of the working of the brain from the more invasive electrophysiology studies in nonhuman primates. There are two parts to this comparison: firstl to establish the link between functional MRI activation and neuronal activity; second, to study patterns of functional MRI activation in humans and in monkeys to bridge the gap between the two species. For these studies the technique remains the same, only the species under investigation varied. This chapter looks at this latter comparison using functional MRI across species. This is the first direct visualization of functional homology between primate species using fMRI.

3.1 Abstract

We report a technique for functional magnetic resonance imaging (fMRI) in an awake, co-operative, rhesus macaque (*Macaca mulatta*) in a conventional 1.5 T clinical MR scanner, thus accomplishing the first direct comparison of activation in visual cortex between humans and nonhuman primates with fMRI. Activation was seen in multiple

areas of striate and extra-striate visual cortex and in areas for motion, object and face recognition in the monkey and in homologous visual areas in a human volunteer. This article describes T_1, T_2 and T_2* values for macaque cortex, suitable MR imaging sequences, a training schedule, stimulus delivery apparatus and restraining hardware for monkey fMRI using a conventional 19 cm knee coil. Much of our understanding of the functional organization of the primate brain comes from physiological studies in monkeys. Direct comparison between species using fMRI, such as those described here, will help us to relate the wealth of existing knowledge on the functional organization of the nonhuman primate brain to human fMRI.

3.2 Introduction

This paper describes a novel application of functional magnetic resonance imaging (fMRI) for use in an awake-behaving macaque monkey, so that direct comparisons can now be made between rhesus macaque and human functional neuroanatomy. Suitable apparatus to position the monkey within the MRI scanner, and sequence parameters appropriate for macaque functional and anatomical imaging on a conventional 1.5 T scanner are presented, as well as discussion on visual stimulus paradigms and animal handling and training. This report presents the first direct comparison of patterns of visual cortex activation between human and nonhuman primate species using fMRI under the same conditions, performing the same paradigm.

Since its initial description[1], fMRI has seen much development in human subjects for psychology, neuroscience[2,3], and more recently for clinical applications[4,5], allowing us to delineate areas of functional deficit (rather than merely structural deficit) or to track functional recovery[6]. The technique produces images of activated brain regions by detecting the indirect effect of neural activity on local blood flow and oxygen saturation — the BOLD or Blood Oxygen Level Dependent effect.

The application of fMRI has advanced ahead of our understanding of the underlying physiological activities we are studying. fMRI appears to be related to spiking activity of large ensembles of neurons and to local field potentials. The ability of fMRI to represent the population activity of whole ensembles of neurons is a significant contribution to the study of neurophysiology[7-10] and could consequently improve the efficacy of human fMRI as a neuroscience and clinical tool. Macaques are readily trained to perform complex tasks, and with the aid of microelectrode mapping, radioisotope tracers and anatomical studies, have formed the basis of much of our current understanding about primate visual pathways[11-15]. Previous studies have addressed the potential value of fMRI in awake macaque monkeys for investigating visual neuroscience[8,16-18] and basal ganglia function[19]. Evaluating the BOLD effect and correlating it with the underlying neural event is a complex process. Previous approaches have involved co-registration of event-related potentials (ERP), magnetoencephalography (MEG) and electroencephalography (EEG) data with fMRI[20,21] which helps elucidate the underlying temporal trends, but lacks spatial specificity. Another approach has been to compare neural activity in monkeys with functional MRI in humans, however, this often proves confusing as both

inter-species and inter-technique variability need to be considered[9,22,23]. Using a monkey model for fMRI[16] would bridge this gap in two ways. Firstly, allowing comparison of behavioral electrophysiological and fMRI changes in the same animal (direct comparison of fMRI with electrophysiological recordings in humans being limited ethically to cases with preexisting pathology). Secondly, the ability to make direct comparisons between the human and macaque brain using the same imaging technique, and while performing the same paradigm has the potential to greatly improve our understanding of the human brain, allowing us to make direct inferences about human neurophysiology based on our existing wealth of knowledge from macaque neurophysiology.

3.3 Materials and Methods

3.3.1 Experimental Setup

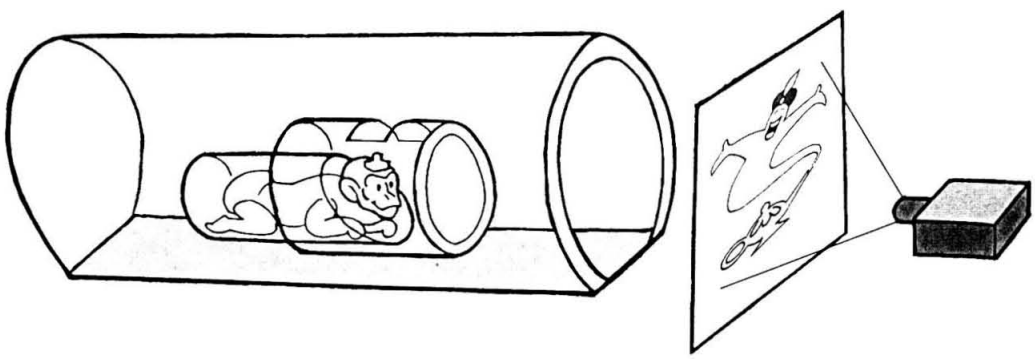

Figure 3.1 The monkey lies within the MRI in a sphinx position in the RF knee coil. A visual stimulus is provided by a video projector on a screen at the opening to the MRI bore.

3.3.1.1 Animal Studies

All animal studies were performed in a healthy, 6.5 kg, adolescent 5-year-old male rhesus macaque. Approval for this research was obtained from the Institutional Animal Care and Use Committee, and Epidemiology and Biosafety Committees. The monkey was trained to lie prone with his head erect ("sphinx" position) in the bore of a clinical MR scanner and to look at a viewing screen placed 200 cm in front of him. The monkey's head was held motionless for the duration of the experiment by means of a surgically attached MR-compatible plastic headcap. To minimize susceptibility artifacts from the restraint, this was machined from a single piece of polyetherimide resin (a material having both good biocompatibility and susceptibility close to that of tissue). The monkey was transported to the MRI facility in an MRI-compatible transport cage. An acrylic (Plexiglas) tube was attached to the transport cage, and the monkey then crawled into the tube, from which only his head protruded. The acrylic tube containing the monkey was then positioned in the MRI machine (Figure 3.1), and the headcap was secured to the window in the receive/transmit coil. This allowed the head to be restrained during experiments, but could be loosened to allow the monkey to raise or lower his head freely between experiments. A tube to supply fruit juice was positioned near the mouth to reward the monkey at the conclusion of each experiment. The monkey wore a diaper for the duration of the study, and all areas of the MRI machine with which the monkey could come into contact (MR table, RF coil) were covered in polythene sheeting. Initial training consisted of habituating the animal to a travel cage and teaching him to crawl into an acrylic tube (taking approximately 2 months). Subsequent training was performed both in a mock-up

of the MRI environment and in the MRI scanner to reward the monkey for keeping still while viewing a visual stimulus (taking approximately 6 months). Rewarding the monkey consisted of positive re-enforcement with treats the monkey enjoyed (in this particular case, fruit juice). Even with head fixation, the monkey was able to move up to 2 or 3 mm. Good behavioral control and the willing co-operation of the monkey was essential to obtain images free from motion artifacts.

3.3.1.2 Human Studies

A young adult male (17-year old) was used as an adolescent "age matched" human control. Informed consent, following Institutional Review Board ethical guidelines, was obtained after detailed explanation of the procedure. The subject lay supine and viewed the same paradigm as the monkey on the screen at his feet via a mirror attached to the head coil (ensuring the same viewing distance and visual field of view as the monkey). His head was restrained with foam pads.

3.3.2 Choice of Stimulus

Macaques, like humans, have a very advanced visual system and use this as their primary sense. For this study a global stimulus which would elicit responses in many parts of the

visual pathways was required, and to which the monkey would readily attend. Preliminary observations were made on two adult male macaques while they watched movie videos in the laboratory to elucidate what sort of visual stimulus would best hold a monkey's attention. Comparison was made between white noise, monochrome movies, color movies and animated cartoons. Attention was judged by recording maximal fixation times. Macaques showed a clear preference for animated cartoons, for which they were capable of maintaining attention, with intermittent short gaps, for up to 35 minutes. They are easily distracted, and a noisy, colorful movie and a regular reward system greatly improve their performance.

3.3.3 Stimulus Paradigm

A visual stimulus was provided using an LCD video projector. For the experiments presented here, sequences from a children's animated film were presented to the monkey in 24-second clips. The film was chosen to include rapidly changing colors, contrast levels, faces and movement. Each film clip was preceded by a period of complete darkness for 24 seconds. The 48-second cycle was repeated 3 times with an additional period of 24 seconds darkness at the end. The whole sequence lasted 3.5 minutes and was repeated 4 times (for signal averaging). For the data presented in this report, the monkey was required only to look passively at the screen. The human subject viewed the same stimulus, but due to superior signal-to-noise ratio (SNR) in fMRI of human brain, only 2 repetitions were needed.

3.3.4 MR System

All imaging was performed on a conventional 1.5 T Siemens VISION MR scanner equipped with 25 mT/m gradients (300 μs rise times). A 19 cm circularly polarized knee coil was used as this was found to have the optimal loading characteristics and 50-100% superiority in SNR over a conventional head coil or flexible surface coil[16]. The monkey's head was positioned at the center of the radio frequency (RF) coil. This provided maximum SNR despite the resulting asymmetrical coil loading by the animal's torso. Local shimming was with an experimental volume-shim algorithm[24].

In order to optimize anatomical and BOLD weighted sequences for monkey cortex, T_1, T_2 and T_2* relaxation times were measured in gray and white matter. A phase-sensitive inversion recovery (IR) sequence was used for T_1 measurements (repetition time (TR), 7666 ms, echo time (TE), 29 ms, Inversion times (TI), 300, 450, 600, 900, 1200, 1500 ms). A 2D Fast Low Angle Shot (FLASH) sequence was used to measure T_2* (TR 1000 ms, TE 5, 7, 10, 12, 15, 18, 20 ms) and T_2 measured by fitting alternate echoes of a Carr-Purcell-Meiboom-Gill (CPMG) multiecho spin echo sequence (TR 8000 ms, TE 22.5 ms - 360 ms in 22.5 ms intervals). Five slices were acquired with 200 x 200 mm FOV and a 256 x 256 matrix with a slice thickness of 5 mm (parameters are summarized in Table 3.1).

	Anatomy (Human)	Anatomy (Monkey)	BOLD (Human)	BOLD (Monkey)	T_1 (Monkey)	T_2 (Monkey)	T_2* (Monkey)
Sequence	**3D-MPRAGE**	**3D-MPRAGE**	**EPI-GE**	**EPI-GE**	**True IR**	**CPMG**	**2D-FLASH**
Bandwidth (Hz) [1]	**33,280 (130)**	**16,640 (130)**	**106,624 (833)**	**106,624 (833)**	**33,280 (130)**	**33,280 (130)**	**33,280 (130)**
Echo Time, TE (ms)	**4.4**	**4.4**	**40**	**40**	**29**	**22.5-360**	**5-20**
Repetition Time, TR (ms)	**11.4**	**11.4**	**2000** [2]	**2000** [2]	**7666**	**8000**	**1000**
Inversion Time, TI (ms)	**20**	**250**	-	-	**300-1500**	-	-
Delay Time, TD (ms)	**0**	**600**	-	-	-	-	-
Flip Angle (degrees)	**10**	**12**	**90**	**90**	**180**	**90**	**90**
Number of Averages	**1**	**1**	**1**	**1**	**1**	**1**	**1**
Field of View, FOV (mm)	**256 x 256**	**90 x 90**	**448 x 448**	**256 x 256**	**200 x 200**	**200 x 200**	**200 x 200**
Imaging Matrix	**256 x 256**	**128 x 128**	**128 x 128**	**128 x 128**	**256 x 256**	**256 x 256**	**256 x 256**
Imaging Plane	**Sagittal**	**Axial**	**Axial**	**Coronal**	**Axial**	**Axial**	**Axial**
Slice (slab) Thickness (mm)	**140** [3]	**80** [3]	**4**	**5**	**5**	**5**	**5**
Number of slices	**140** [4]	**98** [4]	-	-	**5**	**5**	**5**
Voxel Resolution (mm)	**1 x 1 x 1**	**0.7 x 0.7 x 0.8**	**3.5 x 3.5 x 4**	**2 x 2 x 5**	**0.8 x 0.8 x 5**	**0.8 x 0.8 x 5**	**0.8 x 0.8 x 5**
Number of Measurements [5]	-	-	**84 x 2**	**84 x 4**	-	-	-

Table 3.1 Summary of MRI sequence parameters for fMRI, anatomical and relaxation measurements. Notes: (1) Bandwidth per pixel shown in parentheses, (2) effective TR determined by the fMRI experiment repetition time, (3) slab thickness is shown for 3D sequences, (4) Indicates Number of phase encode steps for 3D sequences (5) number of time points measured x number of experiments averaged.

Anatomical imaging was obtained using a 3-D Magnetization-Prepared Rapid Gradient Echo (MPRAGE) sequence. The measured T_1 values of monkey cortex were used to set initial sequence parameters. The sequence was then further refined empirically for best gray/white matter contrast. Optimal parameters for monkey cortex were found to be TR/TE = 11.4 / 4.4 ms, flip angle 12 degrees, inversion time (preparation time) 250 ms and delay time (magnetization recovery time) 600 ms. A 90 x 90 mm field of view (FOV) was acquired with a 128 x 128 matrix, and 98 phase encode steps made through a 80 mm slab (0.7 x 0.7 x 0.8 mm resolution). 100% over-sampling was used in the phase, read and slab directions to reduce "wrap" artifacts and increase SNR. The total acquisition time was 13 minutes.

For BOLD weighted images, a low bandwidth (833 Hz/pixel) echo-planar gradient echo (EPI GE) sequence was found to give the best results (SNR from echo-planar spin echo was observed to be too low at 1.5 T for monkey fMRI). Echo-planar images were collected in the x-y plane within the scanner (i.e. coronal in the prone monkey, and transaxial in the supine human subject). This choice of scan-plane took advantage of the most homogeneous B_0 field direction and minimized EPI warping artifacts. The effective echo time (TE_{eff}) of 40 ms was chosen to approximate the T_2* of monkey cortex for maximal functional contrast[25]. Eight, 5 mm thick coronal slices of the monkey's occipital cortex were acquired per repetition of 2000 ms, thus the effective TR = 2000 ms. Eighty-six repetitions of the 8 slices were acquired, the whole run taking less than 4 minutes. The first 2 repetitions were not used in data analysis allowing 4 seconds (4-times T_1 of gray matter) to ensure steady state. Optimum voxel size for macaque was determined

empirically to allow maximum BOLD contrast-to-noise ratio (CNR) per pixel without excessive partial volume averaging[16]. A voxel volume of 40 μl provided optimal BOLD CNR but was too coarse to define anatomical structures in the small macaque brain. Resolution was improved to 20 μl and SNR elevated with use of 4-fold signal averaging. This resolution was achieved by imaging a FOV of 256 x 256 mm and a 128 x 128 matrix using 5 mm slices (resolution 2 x 2 x 5 mm).

For the human studies, a conventional circularly polarized 26 cm head coil was used. Optimum sequence timing parameters for 3D-MPRAGE were TR/TE = 11.4 / 4.4 ms, flip angle 10 degrees, inversion time 20 ms and delay time 0 ms. A 256 x 256 mm FOV and 256 x 256 matrix was acquired, and 140 phase encode steps taken through a 140 mm slab (isotropic 1 mm resolution). The sequence had been previously optimized for another human fMRI study, and was not re-optimized in this current study[21]. For BOLD studies the same low bandwidth (833 Hz/pixel) was used with TE_{eff} = 40 ms, and effective TR = 2000 ms. Ten axial 4 mm slices with FOV 448 x 448 mm were acquired every 2000 ms with a 128 x 128 matrix to achieve the desired voxel size (resolution 3.5 x 3.5 x 4 mm). Eighty-six repetitions of the 10 slices were taken in under 4 minutes (84 used for image processing). This was repeated twice for signal averaging. Image parameters are summarized in Table 3.1.

3.3.5 Image Post-Processing

The time-dependent echo-planar images were processed off line on a Sun/Sparc unix workstation with AFNI software[26]. Time series were initially corrected for any motion using an AIR technique and Fourier interpolation within AFNI. The multiple repetitions of the time-dependent series (4 for the monkey studies, 2 for the human studies) were averaged into a single series to improve SNR. Functional images were generated using a cross-correlation technique. A series of phase-shifted trapezoids were used as the reference waveforms, which were cross-correlated on a pixel-by-pixel basis with the MR signal time course. Gram-Schmidt orthogonalization was used to remove drift in the time series using a third order polynomial[25]. To remove spurious pixels, the functional intensity map was thresholded at a correlation-coefficient value of $|r| > 0.5$ ($p < 1x10^{-3}$ following conservative Bonferroni correction for multiple comparisons). Only pixels in a cluster of at least 3 contiguous significant pixels were displayed. Functional images were generated by fitting the reference waveform to the MR signal time course by linear fit, with intensity representing the magnitude of the fit coefficient. To reject spurious activation in areas of low signal, the linear fit coefficient was normalized by the baseline MR signal for each pixel. Pixel intensity was thus calibrated as percentage change relative to baseline. MPRAGE and functional maps were co-registered using AFNI software. Discrepancies in the co-registration were corrected by "nudging" the anatomical images (up to one or two pixels). Images were treated as rigid bodies and no unwarping performed. No additional interpolation or resampling was performed. Studies with residual motion artifact, which was not corrected by image re-registration, were

rejected. This was assessed by examining the MR time course of areas of scalp which would be sensitive to stimulus-correlated motion artifact, but would not be expected to have stimulus-correlated BOLD activation.

Borders of functional cortical areas in human brain were defined by areas of significant activation during the fMRI task, and subdivided manually based on previous human fMRI literature[2,22,27-33] and PET literature[34,35]. In the macaque, areas of activation were manually subdivided into distinct retinotopic cortical regions from anatomical studies[12,36] and single unit recording and tracer studies[37-40].

Post-processing of spin-echo and gradient-echo images for tissue relaxometry in macaque brain was done using NIH-Image software (U.S. National Institutes of Health, http://rsb.info.nih.gov/nih-image/). Multiple regions of interest (ROI) were drawn around anatomically defined gray and white matter on the TI = 300 ms phase-sensitive IR images (which had the best gray/white matter contrast) and the ROI copied to all the other images. To calculate T_1 values, MR signal intensity S(TI) for gray matter and white matter was fitted to the inversion-recovery relaxation curve described by equation 1:

$$S(TI) = M_0(1 - e^{-TI/T_1}) + M_Z(0)e^{-TI/T_1} \qquad [1]$$

Where M_0 is the initial longitudinal magnetization, $M_Z(0)$ is the magnetization at TI = 0, *immediately* following the inversion pulse and TI is the inversion time.

T_2 values were calculated from the CPMG sequence by fitting the MR signal S(nτ) in gray and white matter to alternate echoes of the spin-echo relaxation curve described in equation 2:

$$S(n\tau) = \begin{cases} S_{ODD} e^{-n\tau/T_2}(1 - e^{-TR/T_1}) & n = 1,3,5,7,..... \\ S_{EVEN} e^{-n\tau/T_2}(1 - e^{-TR/T_1}) & n = 2,4,6,8,..... \end{cases} \quad [2]$$

τ is the CPMG echo spacing (22.5 ms), n is the echo number, S_{ODD} and S_{EVEN} are the initial signals at n=0 for the odd and even echo trains respectively. The final value for T_2 was the mean of T_2 values calculated from even and odd echo relaxation curves.

T_2* values were calculated by assuming an exponential relationship between the MR signal, S(TE), and the echo time, TE, described by equation 3:

$$S(TE) \approx S'(0) e^{-TE/T_2^*} \quad [3]$$

S′(0) is the initial signal.

The fit optimization was implemented in Matlab (The Mathworks Inc., Natick, MA) using a proprietary large-scale subspace trust-region algorithm based on an interior-reflective Newton method[41]. The algorithm allows specification of upper and lower bounds on each optimized parameter.

	Gray Matter (n=3)	White Matter (n=3)
T_1 (ms)	**1010 ± 8.5** (920)	**790 ± 4.0** (790)
T_2 (ms)	**94 ± 0.8** (101)	**92 ± 2.5** (92)
T_2* (ms)	**49 ± 2.3**	**46 ± 6.5**

Table 3.2 T_1, T_2 and T_2* values for macaque brain in n=3 monkeys expressed as mean ± standard deviation. Typical values for human brain are shown in parentheses[42].

3.4 Results

Measured values of T_1 and T_2 relaxation times for macaque cortex are shown in Table 2. The T_2 values of macaque gray matter were lower than in humans, and the T_1 values higher. White matter results were identical for both species. These T_1 and T_2* values were used as a first approximation in optimizing the MPRAGE and BOLD weighted sequences respectively, as described above.

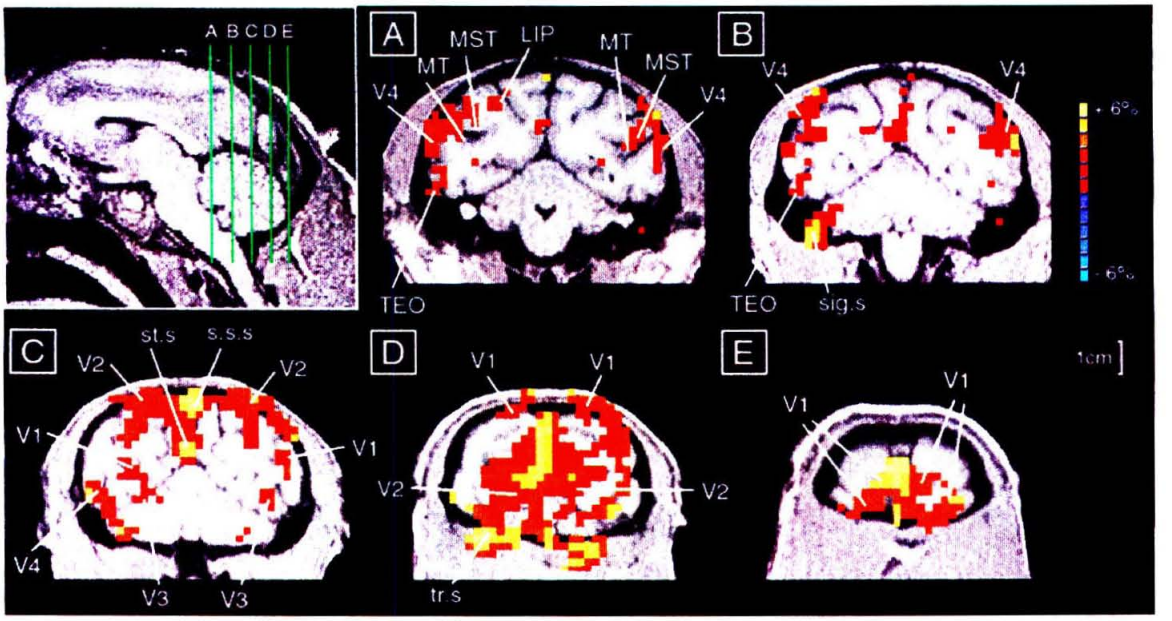

Figure 3.2

Functional activation in macaque brain. Activated pixels are 2 x 2 mm superimposed on T_1 weighted MP-RAGE images of 0.7 x 0.7 mm resolution (coronal images A-E are at 5 mm spacing ranging from 25 to 5 mm anterior to the occipital pole). Labeled areas are visual cortex (V1, V2, V3, V4), medial temporal area (MT), medial superior temporal area (MST), lateral intraparietal area (LIP), superior sagittal sinus (s.s.s), straight sinus (st.s), transverse sinus (tr.s), sigmoid sinus (sig.s).

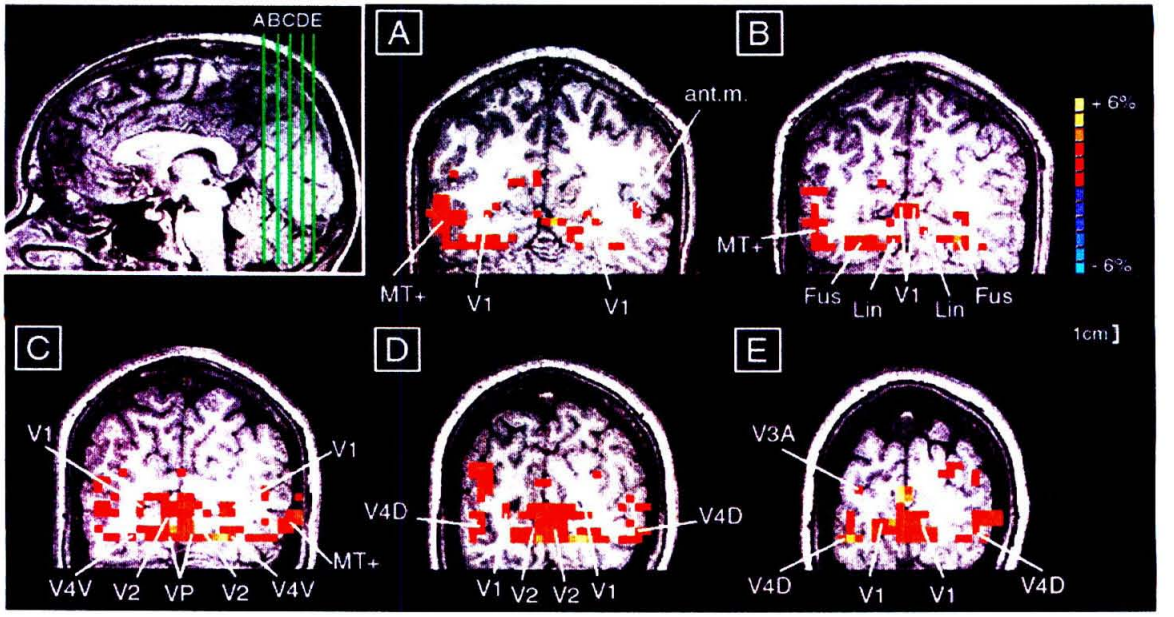

Figure 3.3

Functional activation in human visual cortex. Activated pixels are 3.5 x 4 mm superimposed on T_1 weighted MPRAGE images of 1 mm isotropic resolution. Coronal images A-E are at 7 mm spacing ranging from 44 to 16 mm anterior to the occipital pole. Green bars on the sagittal image indicate the position of coronal images A-E (height of green bars indicates superior-inferior extent over which fMRI data was acquired). Labeled areas are visual cortex (V1, V2, VP, V3A, V4 — dorsal and ventral), medial temporal complex (MT+), fusiform gyrus (Fus), lingual gyrus (Lin), anterior motion area (ant.m).

The functional intensity maps for macaque and human visual cortex show homologous anatomical locations in both species and have been labeled in Figures 3.2 and 3.3. Areas of fMRI activation are clearly seen as discrete areas in the striate and extra-striate visual

cortex. These areas show high correlation with the presented visual stimulus. Activation is observed in the macaque brain in areas corresponding to hierarchical visual cortical areas V1, V2, V3, V4, in parietal area LIP (lateral intraparietal) and temporal areas MT (medial temporal), MST (medial superior temporal) and TEO (temporal occipital area). The central veins draining this area (superior sagittal sinus, straight sinus, transverse sinus and sigmoid sinus) also show activation. Human cortical activation is seen in homologous visual areas V1, V2, VP, V3A, V4, MT-complex (MT+), fusiform, lingual and parahippocampal gyri and anterior visual motion areas.

3.5 Discussion

This technique provides high-resolution images of discrete areas of fMRI activation in the macaque monkey, which are comparable to visual fMRI studies in humans. Areas of activation are recognizable in striate and extra-striate visual cortex consistent with what would be expected from this global stimulus paradigm.

The strong activation in the primary and secondary areas (V1, V2) of macaque retinotopic visual cortex (Figure 3.2) confirms the cartoon movie is stimulating visual pathways. Activation is also noted in ventral and dorsal visual processing streams. This includes area V4 (associated with the vivid colors in a stimulus)[43], also noted is activation in areas V3 and medial temporal area, MT, which are associated with the perception of moving scenes in a stimulus[44]. Activation in medial superior temporal area, MST,

suggests that the stimulus may be providing "optic flow" (the complex visual motion that may be encountered during self-motion)[45,46]. Activation of TEO (architectonic temporal occipital area) has previously been associated with object and face recognition[37] and fMRI activation in area TEO seen in this experiment may indicate that the monkey is recognizing faces and distinct objects in the cartoon. Activation located in the lateral intraparietal area, LIP, is seen with stimuli requiring saccadic movements to different areas of interest on the screen[47] (i.e., a non-fixating stimulus).

The activation in the human visual cortex shows a similar pattern of retinotopic cortical activation, with ventral and dorsal stream activation. The anatomical positions do not correlate structurally across species[22,32,33]; however, functionally homologous areas of activation are identified in both species, and their relative size and position are readily observed. Retinotopic visual areas V1, V2 and VP are activated during the stimulus (Figure 3.3). Human visual cortex also shows V4 activation, which may be associated with the vivid colors of a stimulus[35] and activation in the MT-complex (the human homologue of macaque area MT and MST) similar to that seen in the monkey[3]. Comparison with previous studies of face and object recognition in humans show similar patterns of cortical activation in the lingual and fusiform gyri[29-31] using the current stimulus. These are believed to be homologous to macaque area TEO[31]. Activation in human supplementary anterior visual motion areas is also observed adjacent to auditory cortex, which may correspond to the macaque superior temporal polysensory area[27]. Although the stimulus activated many areas of the visual pathways, the exact feature of the stimulus (e.g., color, motion, objects) that is actually activating each distinct area in

macaque or human cortex is not confirmed from the current study and is the subject of ongoing work. These initial observations of areas of potential cross species homology are currently the subject or more detailed fMRI studies with more directed stimuli than the simple cartoon animation described here.

There are asymmetries in the patterns of visual activation in both the macaque and human fMRI studies. Functional lateralization is well described in humans, particularly language, parietal function and dominant handedness. fMRI studies have described lateral asymmetry in other areas, e.g., MT-complex[27]. Unlike human studies, the macaque's fMRI does not show any lateral asymmetry in MT activation. This is not unexpected, as clinically macaques show considerably less lateralization than humans (and are ambidextrous). Despite this, some asymmetry is seen in the pattern of activation in the macaque (e.g., dorsal V1 in Figure 3.2d). This may be due to the stimulus used. The subject was free to observe the movie without fixating at a particular part of it, thus it is possible that both the monkey and human subjects experienced fluctuations in visual attention, perhaps becoming less attentive to all or part of the stimulus. Visual attention has been shown to modulate fMRI signal in retinotopic visual cortex[21]. Further studies are planned which include a more refined stimulus paradigm to more precisely map known areas of cerebral activation. For these more complex paradigms and for behavioral studies, we have developed an infrared system for real-time monitoring of eye position which will enable us to better answer these questions.

The imaging parameters used to generate these fMRI images of macaque cortex result in a pixel dimension approximating the cross-sectional diameter of the large draining cerebral veins. This tends to exaggerate the signal from these structures, as does our use of a free induction decay EPI sequence for BOLD imaging. These structures are readily apparent in Figure 3.2 (superior sagittal sinus, straight sinus, transverse sinus, and sigmoid sinus). They are easily differentiated from activation in adjacent cortical structures by their anatomical position. Measures to suppress the signal from larger veins (spin echo EPI, diffusion weighting, smaller voxels) would result in lower signal-to-noise and reduced fMRI sensitivity. Any anatomical ambiguity was felt to be minimal, and was outweighed by the overall improved BOLD CNR. Large draining veins are not seen in the human study because the 10 axial slices were centered at the level of the visual cortex and did not extend sufficiently superiorly to include the midline sinuses.

Because of the small overall size of the monkey brain, and the smaller detail with which it needs to be examined, both resolution and SNR need to be maximized. Empirically, a voxel size between 30 and 45 μl was preferred, providing both adequate SNR and BOLD CNR[16]. This resolution was, however, found to be too coarse to define anatomical structures in the small macaque brain. Signal averaging allows some compromise in SNR per run to achieve better resolution (4 averages of a 20 μl have the same effective SNR as a 40 μl voxel).

The percentage modulation provides a useful benchmark when comparing the animal model with human studies, but is not a good measure for optimizing voxel sizes[16]. CNR increases with increasing voxel size, but the baseline MRI signal may also change due to partial volume averaging. With smaller voxels CNR is reduced. Reducing the in-plane resolution at the expense of some through-plane resolution also allowed reduction of susceptibility artifacts from surrounding hardware while retaining overall voxel size and SNR. As with all NMR experiments, this represents a compromise, and the larger through-plane slice profile results in a "staircase" approximation to the posterior curvature of the brain. Thus some cortical pixels are projected beyond the apparent margin of the brain when superimposed on the high-resolution anatomical images (even though they are clearly within cortex on the raw echo-planar images). Improvement in through-plane resolution can be achieved with further repetition and averaging, but this also prolongs the time which the monkey must remain still in the scanner. The parameters described above represent a good compromise in which some trade-off is necessary to retain subject concentration and co-operation. With further training and habituation further improvement is anticipated.

Relaxometry studies of macaque brain show that gray matter T_1 relaxation is longer than human gray matter and T_2 relaxation slightly shorter than human gray matter. White matter values are identical in both species (Table 3.2). T_2 relaxation time reduces with increasing neuronal organization (e.g., T_2 trend in fetal vs. neonatal vs. adult brain)[48]. The comparable T_2 times may indicate a level of structure and organization comparable to human cortex. These results differ from previous values[16], and we believe are more

accurate as the current technique uses a more rigorous methodology and also incorporates n=3 animals. A CPMG multi-echo method was used, which has been shown to give a superior measurement for T_2 compared with conventional spin echo[49,50]. In addition, the alternate echoes were fitted separately to compensate for possible shortfalls in the 180 degree pulse and eddy current effects. The exponential fit for the phase sensitive IR sequence also used a fit parameter for the 180 degree pulse, to allow for shortfalls in the flip angle in different tissues. The curve fitting algorithm used in this study was also superior to that used previously[16] and now incorporates a large-scale subspace trust-region algorithm and allows specification of upper and lower bounds on each optimized parameter which achieves superior convergence. The current results suggest human and macaque relaxation parameters are closer to each other than was previously thought.

Monkey imaging has been achieved using a standard Siemens RF volume knee coil. This was found to provide the best SNR characteristics for imaging monkeys. It also provided a convenient anchor point for our headpost locator. While surface coils may improve signal-to-noise in imaging the occipital cortex, other practical matters precluded their use; the large size of the standard flex coil (37 x 17 cm) made it more difficult to use with monkeys and homogeneous coverage of the whole brain was better with the volume coil. This ability to utilize the manufacturer's standard equipment makes this experimental model versatile. Monkey MRI can be achieved using a clinical scanner and standard clinical knee coil without the necessity or expense of building dedicated RF hardware.

3.6 Conclusion

This technique produces high-quality fMRI images in *Macaca mulatta* visual cortex using a conventional 1.5 T clinical MR scanner and a standard RF volume coil and allows direct comparison with human fMRI. The stimulus paradigm used is simple and non-interactive. It activates large areas of striate and extrastriate visual cortex. The results of this study demonstrate that fMRI data from a macaque monkey can be used as a model for studying the physiology of fMRI in man. The T_1 and T_2 values of macaque brain are similar to humans, and the functional distribution of activation in the visual pathways also appear to be homologous. The existing wealth of understanding of functional organization in macaque cortex can now be more directly correlated with emerging data from human fMRI studies. The basic technique can be easily modified to allow imaging of other areas of the macaque cortex, permitting further comparison with humans.

The technique described here represents a new tool for studying the underlying physiology of functional MRI using a method which can be implemented on any conventional clinical MRI scanner. The true strength of this model will be combining this cross-species fMRI study with animal fMRI and direct electrophysiological studies. This would give us a much better handle on the significance of fMRI activation maps in humans with respect to the underlying neuronal activity. This understanding is one of the next crucial steps in refining fMRI as a neuroscience and clinical tool.

3.7 References

1. Ogawa, S., Lee, T. M., Kay, A. R. and Tank, D. W. Brain magnetic resonance imaging with contrast dependent on blood oxygenation. *Proc. Natl. Acad. Sci. USA* **87**, 9868-9872 (1990).
2. Sereno, M. I. et al. Borders of multiple visual areas in humans revealed by functional magnetic resonance imaging. *Science* **268**, 889-893 (1995).
3. Tootell, R. B. et al. Functional analysis of human MT and related visual cortical areas using magnetic resonance imaging. *J. Neurosci.* **15**, 3215-30 (1995).
4. Stapleton, S. R. et al. Combined utility of functional MRI, cortical mapping, and frameless stereotaxy in the resection of lesions in eloquent areas of brain in children. *Pediatr. Neurosurg.* **26**, 68-82 (1997).
5. Lee, C. C. et al. Assessment of functional MR imaging in neurosurgical planning. *AJNR Am. J. Neuroradiol.* **20**, 1511-1519 (1999).
6. Bilecen, D. et al. Cortical reorganization after acute unilateral hearing loss traced by fMRI. *Neurology* **54**, 765-7 (2000).
7. Logothetis, N. K., Pauls, J., Oeltermann, A., Trinath, T. and Augath, M. The relationship of LFPS, MUA and SUA to the BOLD fMRI signal. *Proc. of Society for Neuroscience* **26**, 820 (2000).
8. Paradiso, M. A. Monkey business builds a bridge to the human brain [news; comment]. *Nat. Neurosci.* **2**, 491-2 (1999).
9. Rees, G., Friston, K. and Koch, C. A direct quantitative relationship between the functional properties of human and macaque V5. *Nat. Neurosci.* **3**, 716-23 (2000).

10. Disbrow, E. A., Slutsky, D. A., Roberts, T. P. and Krubitzer, L. A. Functional MRI at 1.5 tesla: a comparison of the blood oxygenation level-dependent signal and electrophysiology. *Proc. Natl. Acad. Sci. USA* **97**, 9718-23 (2000).

11. Maunsell, J. H. and Newsome, W. T. Visual processing in monkey extrastriate cortex. *Annu. Rev. Neurosci.* **10**, 363-401 (1987).

12. Tootell, R. B., Switkes, E., Silverman, M. S. and Hamilton, S. L. Functional anatomy of macaque striate cortex. II. Retinotopic organization. *J. Neurosci.* **8**, 1531-1568 (1988).

13. Felleman, D. J. and Van Essen, D. C. Distributed hierarchical processing in the primate cerebral cortex. *Cereb. Cortex.* **1**, 1-47 (1991).

14. Andersen, R. A. Neural mechanisms of visual motion perception in primates. *Neuron* **18**, 865-872 (1997).

15. Snyder, L. H., Batista, A. P. and Andersen, R. A. Coding of intention in the posterior parietal cortex. *Nature* **386**, 167-170 (1997).

16. Dubowitz, D. J. et al. Functional magnetic resonance imaging in macaque cortex. *Neuroreport* **9**, 2213-2218 (1998).

17. Logothetis, N. K., Guggenberger, H., Peled, S. and Pauls, J. Functional imaging of the monkey brain. *Nat. Neurosci.* **2**, 555-62 (1999).

18. Stefanacci, L. et al. fMRI of monkey visual cortex. *Neuron* **20**, 1051-7 (1998).

19. Zhang, Z., Andersen, A. H., Avison, M. J., Gerhardt, G. A. and Gash, D. M. Functional MRI of apomorphine activation of the basal ganglia in awake rhesus monkeys. *Brain Res.* **852**, 290-6 (2000).

20. George, J. S. et al. Mapping function in the human brain with magnetoencephalography, anatomical magnetic resonance imaging, and functional magnetic resonance imaging. *J. Clin. Neurophysiol.* **12**, 406-431 (1995).

21. Martinez, A. et al. Involvement of striate and extrastriate visual cortical areas in spatial attention. *Nat. Neurosci.* **2**, 364-369 (1999).

22. Tootell, R. B., Dale, A. M., Sereno, M. I. and Malach, R. New images from human visual cortex. *Trends Neurosci.* **19**, 481-9 (1996).

23. Heeger, D. J., Huk, A. C., Geisler, W. S. and Albrecht, D. G. Spikes versus BOLD: what does neuroimaging tell us about neuronal activity? *Nat. Neurosci.* **3**, 631-3 (2000).

24. Heid, O. H. Noniterative localized in vivo shimming in <15s. *Proc. of. Int. Soc. Magn. Res. Med.* **1**, 363 (1996).

25. Bandettini, P. A., Jesmanowicz, A., Wong, E. C. and Hyde, J. S. Processing strategies for time-course data sets in functional MRI of the human brain. *Magn. Reson. Med.* **30**, 161-173 (1993).

26. Cox, R. W. and Hyde, J. S. Software tools for analysis and visualization of fMRI data. *NMR Biomed.* **10**, 171-178 (1997).

27. Howard, R. J. et al. A direct demonstration of functional specialization within motion- related visual and auditory cortex of the human brain. *Curr. Biol.* **6**, 1015-1019 (1996).

28. DeYoe, E. A., Bandettini, P., Neitz, J., Miller, D. and Winans, P. Functional magnetic resonance imaging (FMRI) of the human brain. *J. Neurosci. Methods* **54**, 171-187 (1994).

29. Clark, V. P., Maisog, J. M. and Haxby, J. V. fMRI study of face perception and memory using random stimulus sequences. *J. Neurophysiol.* **79**, 3257-3265 (1998).

30. Gauthier, I., Tarr, M. J., Anderson, A. W., Skudlarski, P. and Gore, J. C. Activation of the middle fusiform 'face area' increases with expertise in recognizing novel objects. *Nat. Neurosci.* **2**, 568-573 (1999).

31. Kanwisher, N., McDermott, J. and Chun, M. M. The fusiform face area: a module in human extrastriate cortex specialized for face perception. *J. Neurosci.* **17**, 4302-11 (1997).

32. Sereno, M. I. and Allman, J. M. in *The Neural Basis of Visual Function* (ed. Leventhal, A. G.) 160-172 (Macmillan, London, 1991).

33. Sereno, M. I. Brain mapping in animals and humans. *Curr. Opin. Neurobiol.* **8**, 188-194 (1998).

34. McKeefry, D. J., Watson, J. D., Frackowiak, R. S., Fong, K. and Zeki, S. The activity in human areas V1/V2, V3, and V5 during the perception of coherent and incoherent motion. *Neuroimage* **5**, 1-12 (1997).

35. Zeki, S. et al. A direct demonstration of functional specialization in human visual cortex. *J. Neurosci.* **11**, 641-649 (1991).

36. Paxinos, G., Huang, X.-F. and Toga, A. W. *The rhesus monkey brain in stereotaxic coordinates* (Academic Press, London, 1999).

37. Boussaoud, D., Desimone, R. and Ungerleider, L. G. Visual topography of area TEO in the macaque. *J. Comp. Neurol.* **306**, 554-575 (1991).

38. Gattass, R., Gross, C. G. and Sandell, J. H. Visual topography of V2 in the macaque. *J. Comp. Neurol.* **201**, 519-539 (1981).

39. Gattass, R., Sousa, A. P. and Gross, C. G. Visuotopic organization and extent of V3 and V4 of the macaque. *J. Neurosci.* **8**, 1831-1845 (1988).

40. Ungerleider, L. G. and Desimone, R. Cortical connections of visual area MT in the macaque. *J. Comp. Neurol.* **248**, 190-222 (1986).

41. Coleman, T. F. and Li, Y. An interior trust region approach for nonlinear minimization subject to bounds. *SIAM J. Optim.* **6**, 418-445 (1996).

42. Wood, M. L., Bronskill, M. J., Mulkern, R. V. and Santyr, G. E. Physical MR desktop data. *J. Magn. Reson. Imaging.* **3 Suppl**, 19-24 (1993).

43. Zeki, S. M. Colour coding in rhesus monkey prestriate cortex. *Brain Res.* **53**, 422-7 (1973).

44. Felleman, D. J. and Van Essen, D. C. Receptive field properties of neurons in area V3 of macaque monkey extrastriate cortex. *J. Neurophysiol* **57**, 889-920 (1987).

45. Saito, H. et al. Integration of direction signals of image motion in the superior temporal sulcus of the macaque monkey. *J. Neurosci.* **6**, 145-57 (1986).

46. Tanaka, K. et al. Analysis of local and wide-field movements in the superior temporal visual areas of the macaque monkey. *J. Neurosci.* **6**, 134-44 (1986).

47. Gnadt, J. W. and Andersen, R. A. Memory related motor planning activity in posterior parietal cortex of macaque. *Exp. Brain. Res.* **70**, 216-20 (1988).

48. Barkovich, A. J. *Pediatric Neuroimaging* (Lippincott Williams and Wilkins, Philadelphia, 2000).

49. Carr, H. Y. and Purcell, E. M. Effects of diffusion on free precession in nuclear magnetic resonance experiments. *Phys. Rev.* **94**, 630 (1954).

50. Meiboom, S. and Gill, D. Modified spin echo method for measuring nuclear relaxation times. *Rev. Sci. Instrum.* **29**, 668 (1958).

3.8 Acknowledgment

We thank Chris Headrick for the illustration (Figure 3.1), Betty Gillikin for animal care assistance and Marty Sereno for enlightening discussion and assistance with data interpretation. This work is supported by grants from the Pasadena Neurosciences Fellowship of Huntington Medical Research Institutes (DJD) and the National Eye Institute (RAA).

Chapter 4 Enhancing fMRI Contrast in Awake-behaving Primates Using Intravascular Magnetite Dextran Nanoparticles

To make meaningful comparisons between fMRI and neuronal activity requires high-resolution imaging — ideally at the level of the cortical column or better. Technical improvements in the quality of MR hardware and strength of the applied imaging gradients help address this, but ultimately the resolution that can be achieved is limited by the available signal-to-noise. The small size of the monkey brain (relative to a human), the need for short imaging times and the relatively low magnetic field strength of a standard clinical MR system compound the signal-to-noise problem of monkey imaging. BOLD imaging is dependent on the paramagnetic deoxyhemoglobin as an intrinsic contrast agent. By using a stronger paramagnetic agent, the imaging sequences can be more sensitive to small hemodynamic perturbations. In this chapter, I describe a novel method I developed for rendering the circulating blood volume highly paramagnetic with an exogenous superparamagnetic T_2 contrast agent to improve functional MRI contrast.

4.1 Abstract

Functional MRI in awake-behaving primates is an emerging tool for bridging the gap between human functional MRI (fMRI) and neurophysiology information from nonhuman primates. We report the use of magnetite dextran nanoparticles (Feridex) as a

blood-pool agent to enhance fMRI contrast-to-noise (CNR) in primate fMRI. Intravascular half-life of the magnetite dextran was long compared to lanthanide chelates ($T_{½}$=198 minutes) with shortened T_2 relaxation observed in blood and cerebral cortex. Greater than 3-fold enhancement in the percentage MR signal change was observed using nanoparticles (13%) compared with conventional BOLD fMRI (4%). The calculated regional cerebral blood volume in macaque primary visual cortex increased 32% with photic stimulation. The increased CNR allows greater flexibility in the design of awake-behaving primate fMRI studies with the potential for improvements in resolution and significantly shortened imaging times.

4.2 Introduction

fMRI is a rapidly emerging tool in the study of primate physiology. Previous studies have addressed the potential value of fMRI in awake macaque monkeys for investigating visual neuroscience[1-5] and basal ganglia function[6]. One major limitation in performing monkey fMRI at 1.5 T is the limited signal-to-noise and consequently low contrast-to-noise ratio (CNR) from Blood Oxygen Level-Dependent (BOLD) contrast. As with all imaging techniques, there is a compromise between resolution and sensible imaging time. Monkeys are challenging subjects to study. They need to be meticulously trained to remain still for awake MRI studies (thus shorter imaging sessions facilitate behavioral compliance). However, the brain of a macaque monkey is approximately 1/5th of the size of a human brain[7], so there is also a need for higher resolution compared with human

fMRI studies. One approach to this has been to do macaque imaging at higher applied magnetic field[3]. While improving the CNR, this also increases the unfavorable susceptibility gradients and artifacts which scale proportionately with the applied magnetic field. Another approach has been to restrict imaging to anesthetized animals. This allows longer imaging times and reduces movement artifacts, but may also diminish BOLD effect due to the vasodilator effects by anesthetic agents, and consequent changes on cerebral blood flow (CBF)[8]. The use of anesthesia also excludes cognitive studies for which awake-behaving subjects are required.

We investigated the effect of a blood-pool T_2 contrast agent (i.e., a cerebral blood volume technique) on CNR compared with conventional BOLD contrast in awake-behaving primate fMRI experiments. Previous studies have demonstrated the utility of such agents for MRI in rats [9], cats[10] and human subjects[11].

The use of contrast agents has not found much favor in human cognitive studies because this makes the study more invasive, but holds promise for awake animal studies[12]. This is the first time this technique has been applied to awake primate imaging. Techniques that employ a T_2 contrast agent provide images sensitive to changes in regional cerebral blood volume (CBV). This has been shown in rats to change by 20% with neural activation[9,13] and by 25%[11] to 32%[14] in humans. Unlike deoxyhemoglobin susceptibility, the CBV change is not dependent on applied magnetic field[9], and thus this technique provides great scope for improved fMRI contrast even at conventional magnetic fields (1.5 T).

4.3 Materials and Method

4.3.1 Animal Subjects

Approval for this research was obtained from the Institutional Animal Care and Use Committee, and Epidemiology and Biosafety Committees. All imaging was done on a 1.5 T Siemens Vision MR scanner with 23mT/m gradients (300 μs rise time). Awake-behaving studies were done on a 8.5 kg male rhesus macaque monkey (*Macaca mulatta)* lying in a "sphinx" position within the scanner using a 19 cm circularly polarized knee coil. Contrast excretion measurements were done outside the MR scanner on the same animal. Relaxometry studies were also performed on this monkey and on two additional male macaque monkeys (5.5 kg and 10.5 kg) under isoflurane anesthesia. The technique has been previously described[1,2], but in brief: The animal was transported to the MRI facility in a custom designed cage. For awake studies he crawled into a short tube so that his legs were accessible for intravenous administration of T_2 contrast agent. The monkey was trained to present his leg to the animal handler and accept an intravenous line into a saphenous veins without sedation or general anesthesia. The monkey then crawled into a larger tube which was transferred to the MRI scanner. His head was secured to the transmit/receive coil and a screen placed 57.3 cm in front of him (providing a ±22° visual field of view). Eye-position tracking was performed using a custom-built shielded video camera placed at the bore of the scanner, which was sensitive in the infrared range, and eye illumination from a circular array of 28 MRI compatible IR light emitting diodes emitting at 810nm[15]. Digital signal processing involved a system from ISCAN (Iscan

Inc., Cambridge, MA) integrated into a computer running a custom program written with Labview software (National Instruments Corporation, Austin, TX). This setup allowed eye-tracking in complete darkness to an accuracy of within 1° of arc. The animal was trained to remain motionless in the scanner for the duration of the imaging experiment (i.e. while gradient noise was audible) and to fixate on a central fixation point to an accuracy of <4° visual angle for the duration of the stimulus. He was provided a fruit juice reward at the end of each imaging run.

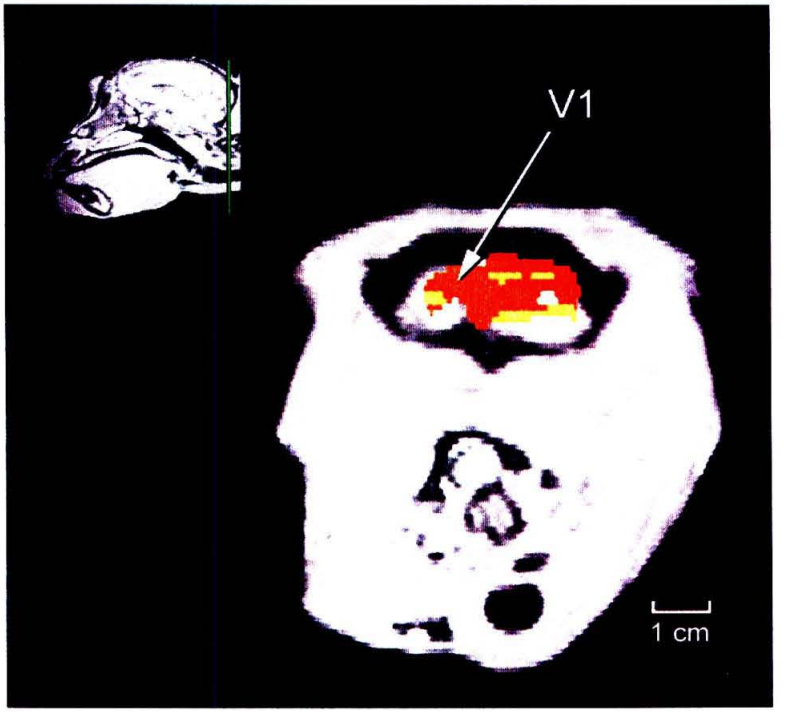

Figure 4.1 Coronal image showing functional activation in primary visual cortex (V1) during photic stimulation in a monkey following intravenous magnetite dextran T_2 contrast agent. The plane of section is indicated by the vertical bar on the sagittal image. The area of V1 used to plot MR signal responses is indicated. (Subject's right is on the left of the image).

For anesthetized studies, the animal was sedated with 10mg/kg ketamine and maintained on 2% isoflurane using an anesthetic setup modified for MRI compatibility.

4.3.2 Contrast Agent

For functional imaging studies with T_2 contrast agent, we used magnetite dextran nanoparticles (Feridex, Advanced Magnetics Inc., Cambridge, MA) infused intravenously. This was given as 4.2 mgFe/kg (750 μMol/kg) diluted into 25 ml and infused over 5 minutes through a 5 μm filter. Imaging was started within 10 minutes of completing the infusion (ensuring equilibrium state concentration). For assessment of whole blood clearance, a dose of 2.8 mgFe/kg (500 μMol/kg) was used.

4.3.3 MR Imaging

BOLD and magnetite-enhanced functional images were acquired using a gradient-echo echo-planar imaging (GE-EPI) mosaic sequence. The effective echo time (TE_{eff}) of 50 ms was chosen to approximate the T_2* of monkey cortex[2]. Isotropic 4 mm resolution was achieved with a FOV of 256 x 256 mm and a 64 x 64 matrix. Fourteen, 4 mm thick axial slices of the entire monkey's brain were acquired per repetition of 2000 ms (effective TR = 2000 ms). Forty-five repetitions of the 14 slices were acquired for BOLD experiments

and 60 repetitions for magnetite dextran experiments. The first repetition was not used in data analysis allowing 2 seconds to ensure steady state. Anatomical images used a 3D Magnetization Prepared Rapid Acquisition Gradient Echo sequence (3D-MPRAGE) with TR/TE = 11.4 / 4.4 ms, flip angle 12 degrees, inversion time (preparation time) 250 ms and delay time (magnetization recovery time) 600 ms. A 141 x 141 mm field of view (FOV) was acquired with a 128 x 128 matrix (zero-padded to 256 x 256), and 118 phase encode steps made through a 130 mm slab (1.1 mm isotropic resolution). Relaxometry measurements for T_2* (R_2*) in cortex used a 2D Fast Low Angle Shot (FLASH) sequence (TR 1000 ms, TE 5, 7, 10, 12, 15, 18, 20 ms) as previously described[2]. Relaxometry measurements on *in vitro* venous blood were performed using a CPMG spectroscopy sequence on a Bruker minispec mq60 at 60 MHz (Bruker Analytik GmbH, Rheinsteffen, Germany).

4.3.4 Stimulus Paradigm

The stimulus consisted of a six second black and white polar checker-board alternating at 8 Hz, which subtended a visual angle of ±20°. The stimulus was preceded by a 1° fixation point visible for 8 seconds. Following the fixation dot and chequer board stimulus the animal remained in the dark for a further 76–106 seconds to allow acquisition of the full recovery of the hemodynamic response.

4.3.5 Image Post-processing

Functional imaging data using BOLD and magnetite dextran contrast were analyzed off-line using AFNI software running on a unix workstation[16].

Functional images were co-registered using a volume-registration algorithm under AFNI. A weighted linear least squares fit of the images was employed with Fourier interpolation used for resampling[17]. Images with excessive motion artifact not corrected by the registration algorithm were excluded. The remaining runs were averaged together to create a single dataset for BOLD imaging and a single dataset for magnetite-enhanced imaging. A representative region of interest was chosen in primary visual area V1 (Figure 4.1). The time course of the percent change in MRI signal in this volume was plotted for BOLD and magnetite-enhanced fMRI (Figure 4.2).

For cerebral relaxometry measurements following magnetite dextran infusion, regions of interest were drawn around anatomically defined gray matter using Scion Image software (http:www.scioncorp.com). R_2* transverse relaxation rate was calculated by assuming an exponential relationship between the MR signal, S(TE), the echo time, TE, and the initial signal S(0) described by equation 1:

$$S(TE) = S(0)e^{-TE \cdot R_2^*} \qquad [1]$$

The fit optimization was implemented in Matlab (The Mathworks Inc., Natick, MA) using a proprietary large-scale subspace trust-region algorithm based on an interior-

reflective Newton method[18]. The algorithm allows specification of upper and lower bounds on each optimized parameter.

Relaxivity data on whole blood to assess clearance of contrast media was assumed to follow first order kinetics and was modeled with monoexponential decline described by equation 2.

$$[Fe]_{Blood} = C_0 \cdot e^{-bt} \qquad [2]$$

$[Fe]_{Blood}$ is the concentration of Fe in blood, C_0 is the instantaneous concentration at time zero. Dividing the injected dose by the instantaneous concentration of contrast media, C_0, yields the volume of distribution of the agent within the animal. The constant, b, is an excretion constant from which the half life of elimination from blood can be calculated. There is a linear relationship between the transverse relaxation rate of the magnetite dextran contrast media in blood and the concentration of Fe. The main components of the measured R_2* are components from blood itself, $R_2{}^*_{Blood}$, and from exogenous magnetite, $R_2{}^*_{Fe}$. (equation 3):

$$R_2{}^*_{Blood} + R_2{}^*_{Fe} = k \cdot [Fe]_{Blood} \qquad [3]$$

The unknown contribution to transverse relaxation rate from Fe, $R_2{}^*_{Fe}$, used in equation 3 was calculated by making serial dilutions of a known concentration of Feridex with water as described in equation 4 (Figure 4.3a).

$$R_2{}^*_{water} + R_2{}^*_{Fe} = k \cdot [Fe]_{water} \qquad [4]$$

Using equation 3 and 4, the actual concentration of Fe was quantified from measurements of R_2* for whole blood drawn at regular intervals following injection of the contrast agent (Figure 4.3b).

To compare the magnitude, duration and onset delay of the positive MR signal change for BOLD with the negative signal change for magnetite-enhanced fMRI, the data was fitted to a gamma-variate function of the form in equation 5 using the same Matlab routine described above.

$$S(t) = A(t - t_0)^r e^{-(t-t_0)/a} \qquad [5]$$

A, r, and a are fit constants and t_0 defines the onset delay following the neuronal stimulus. The maximum signal change was the peak of the curve. The duration of activity was compared during the period when the MR signal exceeded 10% of its maximal value.

We calculated the percentage change in the regional cerebral blood volume following photic stimulation. This model assumes that the effect of the decreased transverse relaxation rate due to BOLD is negligible compared to the increase due to CBV changes with the intravascular contrast agent. Previous studies have shown the rate of change in transverse relaxation rate with blood iron concentration is proportional to the cerebral blood volume (i.e., the cerebral blood volume CBV(t) can be calculated from the slope of a plot of R_2* change with $[Fe]_{blood}$ [11]) as described in equation 6.

$$\frac{R_2^*(t) - R_2^*(0)}{[Fe]_{blood}(t) - [Fe]_{blood}(0)} = K \cdot CBV(t) \qquad [6]$$

$R_2^*(t)$ is the transverse relaxation rate during activation or rest, $R_2^*(0)$ is the relaxation rate prior to injection of magnetite dextran, $[Fe]_{blood}(t)$ is the blood concentration of Fe during the photic stimulation experiment, $[Fe]_{blood}(0)$ is the blood concentration of Fe due to magnetite dextran prior to injection (i.e., zero) and K is a proportionality constant.

The fractional change in blood volume following photic stimulation, ΔCBV, can thus be calculated from the CBV during rest, CBV(r), and during activation, CBV(a), from equation 7.

$$\Delta CBV = \frac{CBV(a) - CBV(r)}{CBV(r)} = \frac{R_2^*(a) - R_2^*(r)}{R_2^*(r) - R_2^*(pre)} \qquad [7]$$

From Equation 1, this can be written in terms of the ratio of MR signal during photic stimulation and at rest.

$$\%CBV = \frac{\frac{-1}{TE}.\ln\left(\frac{S(a)}{S(r)}\right)}{R_2^*(r) - R_2^*(pre)} * 100\% \qquad [8]$$

R_2* in brain was measured before injection of magnetite dextran, R_2*(pre), and at regular time points during the experiment, R_2*(t). This value of R_2*(t) was interpolated to the actual time point of the photic stimulation measurement, R_2*(r), to allow for changes in R_2* due to hepatic elimination of Fe (see equation 2). The MR signal change, S(t), following photic stimulation was fitted to the gamma-variate function described by equation 5 (Figure 4.2). S(r) was the value of the function at t <5 seconds and S(a) was the maximum value of the function (t= 44 seconds).

4.4 Results

Nine runs of BOLD contrast and 5 runs of magnetite-enhanced contrast, which were free from any motion artifact, were acquired in an awake-behaving monkey with eye traces confirming he was fixating for the duration of the experiment. The distribution of fMRI activation for the checker-board stimulus is seen in visual cortex in the correlation map in Figure 4.1. The hemodynamic response curves for conventional BOLD fMRI and magnetite-enhanced fMRI are shown in Figure 4.2. The positive BOLD effect and negative magnetite-induced MR signal changes were fitted to independent gamma-variate functions. Following photic stimulation, the MR signal in macaque visual cortex is modulated by up to 4% for BOLD imaging and follows a characteristic time course – similar to that routinely described in human fMRI at 1.5 T. Increase in BOLD MR signal occurred in primary visual cortex almost immediately following stimulus onset.

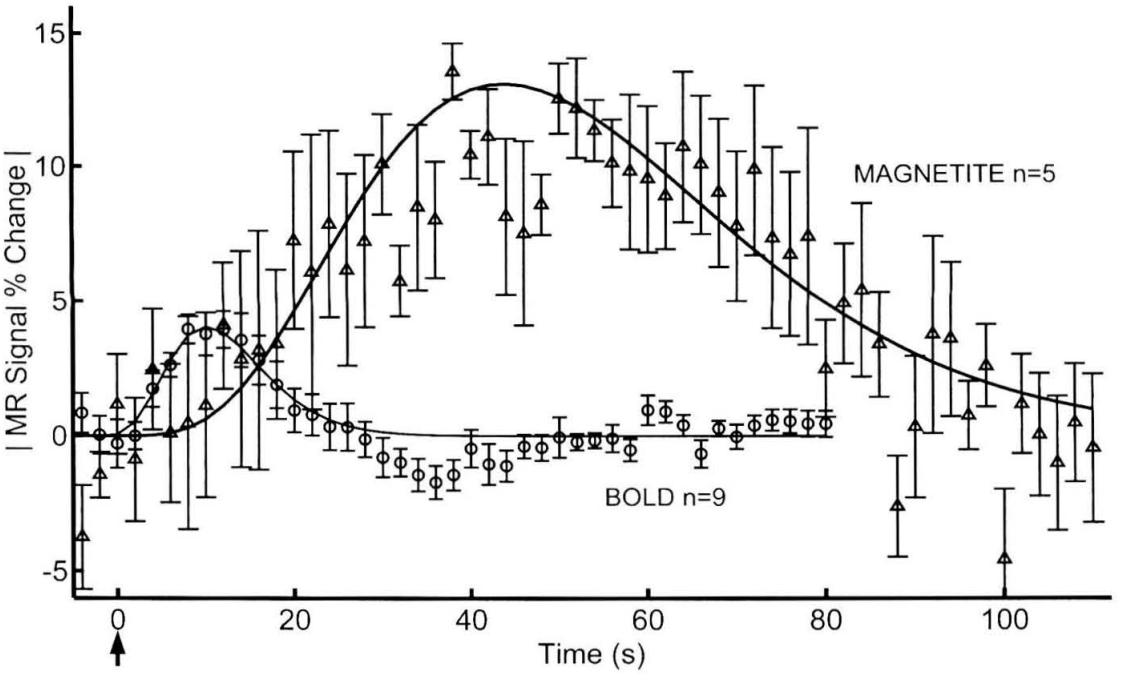

Figure 4.2 The time course of the percentage change in MR signal following 6 seconds photic stimulation is shown for BOLD (o) and magnetite-enhanced (Δ) fMRI. Stimulus onset is indicated by the arrow. Negative MR signal changes for magnetite-enhanced fMRI are shown as positive absolute changes for comparison. Error bars indicate ± 1 standard error for BOLD (n=9) and magnetite dextran (n=5) studies. Solid line is the gamma-variate function fitted to the data for the positive BOLD and negative magnetite dextran responses.

The peak BOLD signal change was observed 10 seconds following the stimulus onset. The response showed a typical rise followed by an undershoot, returning to baseline by 50 seconds. The duration of the positive BOLD change (measured between the rise above 10% maximum signal change to the fall below 10% maximum) was 22 seconds (1-23 seconds after stimulus onset). Using intravenous magnetite dextran, there is a 13.1% negative MR signal change in the same area of primary visual cortex following photic

stimulation. Maximum effect was seen at 44 seconds. The modulation in MR signal persisted for 90 seconds (15–105 seconds between the 10% of maximum points). The intravenous magnetite dextran increased the R_2* (and R_2) relaxation rates in resting gray matter. The change in transverse relaxation rate of blood over time was measured in the same animal used for the fMRI study, and is presented in Figure 4.3b. This shows an elimination $T_{½}$ from blood of 198 minutes. The volume of distribution (instantaneous blood concentration divided by dose injected) was 825ml. The percentage change in regional cerebral blood volume in macaque primary visual cortex following photic stimulation was 32%.

4.5 Discussion

Feridex (ferumoxide solution) is an aqueous colloid of magnetite iron oxide nanoparticles (60–150 nm diameter) associated with dextran having an average chemical composition of $FeO_{1.44}$. Excretion of Feridex is 98% hepatic (its primary use in diagnostic imaging is as a T_2 liver contrast agent). In this study we have used it as a blood-pool contrast agent, taking advantage of its slow excretion kinetics and prolonged blood half-life. The blood volume of a 8.5 kg macaque monkey is approximately 10% of body weight[19], thus the calculated volume of distribution (825 ml) confirms that Feridex is a true blood-pool agent.

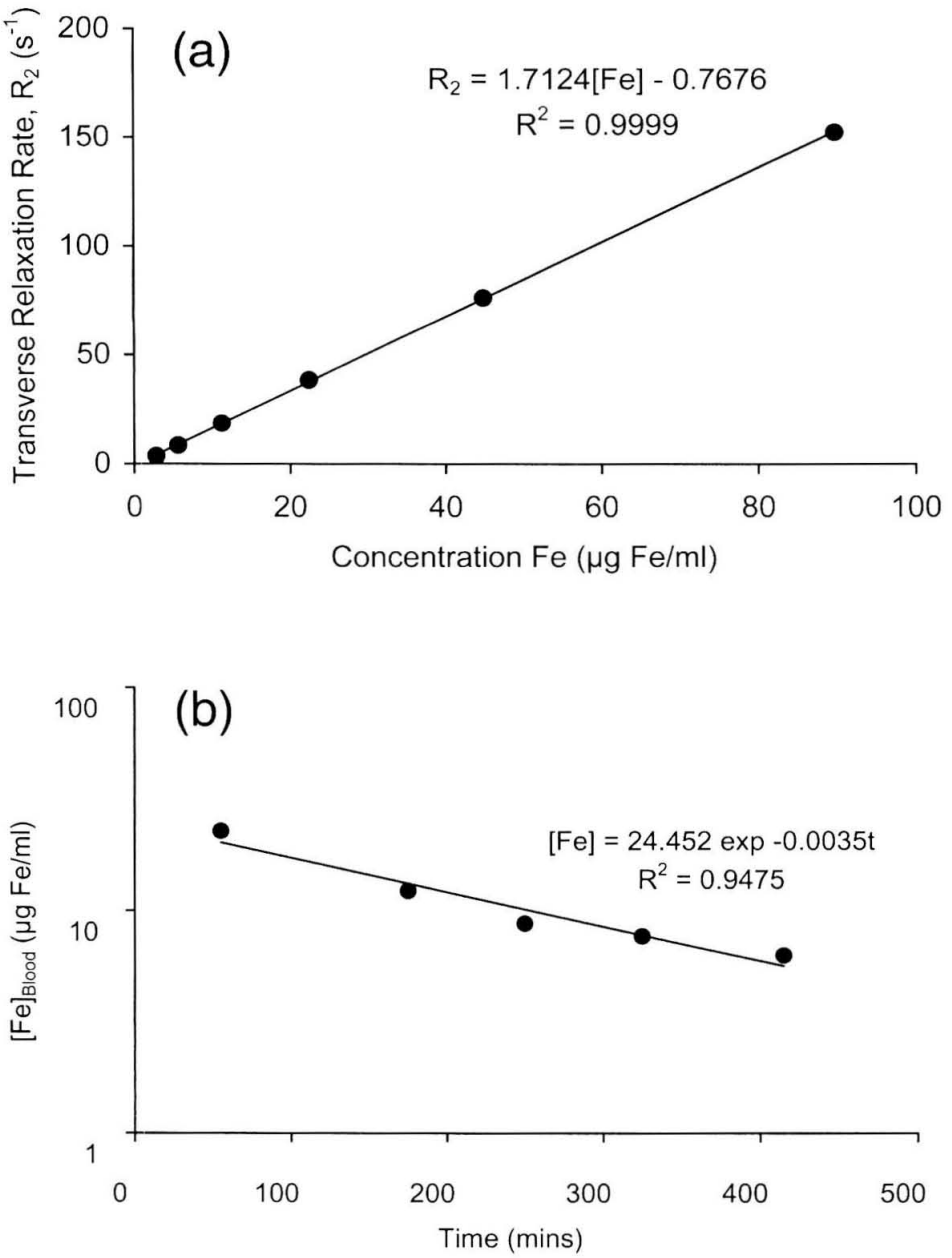

Figure 4.3

Figure 4.3a shows the linear relationship between magnetite dextran concentration in water and transverse relaxation rate used to calibrate the absolute blood concentration of Fe. Figure 4.3b shows the calibrated blood concentration of Fe (semi log scale) following administration of 2.8 mgFe/kg (750 µMol/kg) magnetite dextran. Excretion follows monoexponential kinetics with a blood half-life of 198 minutes.

Functional MRI provides an indirect map of neuronal activation by demonstrating changes in cerebral blood dynamics that accompany neural activity. These temporally correlated changes may be seen as changes in blood flow[20], blood volume[14] or changes in the deoxygenation of hemoglobin[21]. Imaging the changes in blood volume is well established — the first fMRI descriptions of neuronal activity in humans mapped changes in CBV[14]. For human studies, it has become more popular to use fMRI studies with endogenous contrast based on changes in the oxygenation of hemoglobin thus making the study entirely noninvasive. The use of iron oxide T_2 contrast agents with a long intravascular half-life has been shown to be a valid method to track CBV changes during neuronal stimulation in rats[9] and human subjects[11]. The increase in transverse relaxation rate ($\Delta R_2^* = 1/\Delta T_2^*$) due to increased blood volume competes with the decrease in relaxation rate due to changes in deoxyhemoglobin accompanying neuronal activation. It is necessary to use a sufficient intravascular concentration of contrast agent to ensure that the signal changes induced by the contrast agent and increased CBV dominate concurrent BOLD changes. At 1.5 T these relaxivity changes due to hemoglobin susceptibility effects are relatively small; however, the observed MR signal changes due to the T_2 agent are less than the theoretical maximum, as these competing effects reduce the magnitude of the MR signal change[9].

The calculated CBV change with stimulation was 32%. This is in good agreement with previous measurements of between 25%[11] and 32%[14] in human subjects. This concordance in CBV changes between human and macaque highlights a similarity in

their neurovascular physiology which underscores the value of macaque fMRI as a model for better understanding human neurophysiology.

It is important to consider the decay in R_2* over time due to hepatic elimination of contrast medium as well as the R_2* modulation due to changes in blood volume. The elimination half-life of Feridex (198 mins) is of the same order of magnitude as the duration of many primate physiology studies. Closer inspection of the intravascular iron concentration during a typical 3.5 hour primate imaging session using a dose of 4.2 mgFe/kg (750 μMol/kg) shows it ranged from 36.75 μgFe/ml (659 μMol) instantaneously following injection to 19.5 μgFe/ml (350 μMol). Comparison with previous studies using the same T_2 contrast agent in humans indicates that the BOLD effect due to auditory stimulation is completely negated by the iron-oxide enhanced CBV effect at a concentration of 8.4 μgFe/ml (150 μMol)[11]. Extrapolating our elimination curve (Figure 4.3) to this point where the BOLD effect completely opposes signal due to exogenous magnetite, indicates that signal would be lost 7 hours after injection. During prolonged studies, the contrast concentration will diminish, and the opposing BOLD effect will reduce the MR signal, causing reduced CNR and grater variability. During a typical primate study, the opposing effects on transverse relaxation from BOLD may be assumed to be negligible. Under ideal conditions, the signal change with neuronal stimulation could reflect the whole 32% increase in CBV, thus CNR improvements of 8-fold could theoretically be achieved over our 4% BOLD MR signal change. There is thus scope to improve the MR signal response above the 3-fold enhancement demonstrated here. The use of higher doses is under review. Our TE of 50 ms was initially set for maximum

tissue contrast during BOLD studies, and was held constant during the study. Reducing the TE to the T_2* of grey matter following magnetite dextran infusion would further improve SNR and the CNR observed during magnetite-enhanced fMRI. Additionally, using other iron oxide agents with smaller particle size than Feridex (and a longer elimination half-life and higher T_2 relaxivity characteristics[22]) would further improve the signal benefit over conventional BOLD imaging. The variability of the MR signal change in Figure 4.2 is larger for magnetite-enhanced fMRI than for BOLD. This is due to reduction of the resting MR signal by the addition of magnetite-dextran. Magnetite reduces the T_2* of tissue – thus measured signals for a given TE are lower. The MR signal is approximately halved by the addition of magnetite-dextran, thus decreasing the SNR.

In nonhuman primates, the temporal dynamics of the CBV changes are slower than the BOLD effect (similar to that described in rats[9]). This may place some constraints on paradigm design. For block design paradigms, the time-course of each state may need to be longer than the minimum times typically possible for BOLD studies, however superposition calculations may be used to reduce this increase in experimental time. The use of event-related techniques (currently used in BOLD fMRI to observe temporal changes which are fast relative to the prolonged hemodynamic response[23]) can potentially be applied to CBV imaging as well. The prolonged HRF using magnetite also needs to be considered when directly comparing fMRI with primate electrophysiology. The temporal resolution of MRI is already several orders of magnitude below that achievable with single electrode recordings. The advantages of functional MRI is the superior spatial

resolution it affords, thus the potential for added CNR (and hence spatial resolution) are likely to outweigh any loss in temporal resolution from CBV techniques. For most primate studies, the 3-fold increase in CNR (with theoretically further increase possible) outweighs many limitations that the slower return to baseline may place on the choice of paradigm. To achieve a comparable 3-fold increase in CNR using BOLD fMRI at 1.5 T would require a 9-fold increase in experiment time or 3-fold increase in voxel size.

The added CNR by using magnetite-enhanced fMRI can be used to improve resolution or shorten total experimentation time. Motion artifact is the major difficulty in imaging awake-behaving primates, and the ability to reduce the number of runs (and the overall length of an experiment) will have dramatic and positive benefits on experimental success. Nonhuman primate functional neuroanatomy has been used as a model for better understanding the human brain. The smaller brain size may equate to smaller functional units within the cortex for which higher resolution is required (although the exact scaling factor of functional units across species remains to be determined[24]). The ability to achieve higher resolution in primate fMRI also adds to its utility when comparing with neurophysiology data.

The BOLD effect scales between linearly and quadratically with applied field strength[25]. Thus high field imaging at 4.7 T^3 could be expected to afford at least a 3-fold increase in CNR. This theoretical gain needs to be offset by increased bulk-susceptibility artifacts at higher applied magnetic fields. Using magnetite-enhanced fMRI for primate imaging at 1.5 T allows a comparable increase in CNR (with further CNR improvement anticipated

with the use of alternate contrast agents), but without the increase in bulk susceptibility distortions induced by higher field. Similar improvements in resolution seen by increasing the applied field strength to 4.7T are thus achievable using magnetite-enhanced fMRI at 1.5 T.

4.6 Conclusion

We describe a modification of conventional BOLD fMRI applied to awake-behaving primates. Intravenous infusion of magnetite dextran nanoparticle T_2 contrast agent produces a 3-fold increase in CNR. Opportunities for further optimization are also discussed. Considerably faster overall experiments involving fewer sampling repetitions may now be performed, with the potential for higher resolution imaging compared with existing fMRI techniques at 1.5 T. Regional cerebral blood volume increases by 32% in macaque visual cortex, which is comparable to the neuronally induced vascular changes previously described in humans.

4.7 References

1. Dubowitz, D. J. et al. Functional magnetic resonance imaging in macaque cortex. *Neuroreport* **9**, 2213-2218 (1998).

2. Dubowitz, D. J. et al. Direct comparison of visual Cortex activation in human and nonhuman primates using functional magnetic resonance imaging. *Journal of Neuroscience Methods* **107**, 71-80 (2001).

3. Logothetis, N. K., Guggenberger, H., Peled, S. and Pauls, J. Functional imaging of the monkey brain. *Nat. Neurosci.* **2**, 555-62 (1999).

4. Paradiso, M. A. Monkey business builds a bridge to the human brain [news; comment]. *Nat. Neurosci.* **2**, 491-2 (1999).

5. Stefanacci, L. et al. fMRI of monkey visual cortex. *Neuron* **20**, 1051-7 (1998).

6. Zhang, Z., Andersen, A. H., Avison, M. J., Gerhardt, G. A. and Gash, D. M. Functional MRI of apomorphine activation of the basal ganglia in awake rhesus monkeys. *Brain Res.* **852**, 290-6 (2000).

7. Allman, J. M. *Evolving Brains* (Scientific American Library, New York, 1999).

8. Seifritz, E. et al. Effect of ethanol on BOLD response to acoustic stimulation: implications for neuropharmacological fMRI. *Psychiatry Res.* **99**, 1-13 (2000).

9. Mandeville, J. B. et al. Dynamic functional imaging of relative cerebral blood volume during rat forepaw stimulation. *Magn. Reson. Med.* **39**, 615-24 (1998).

10. White, D. L. et al. Iron-dextran as a magnetic susceptibility contrast agent: flow-related contrast effects in the T2-weighted spin-echo MRI of normal rat and cat brain. *Magn. Reson. Med.* **24**, 14-28 (1992).

11. Scheffler, K., Seifritz, E., Haselhorst, R. and Bilecen, D. Titration of the BOLD effect: separation and quantitation of blood volume and oxygenation

changes in the human cerebral cortex during neuronal activation and ferumoxide infusion. *Magn. Reson. Med.* **42**, 829-36 (1999).

12. Dubowitz, D. J., Bernheim, K. A., Chen, D. Y., Bradley, W. G., Jr. and Andersen, R. A. Magnetite-enhanced fMRI improves CNR relative to BOLD fMRI in awake-behaving macaque monkeys at 1.5 T. *Proc of Int Soc Magn. Res. Med.* **1**, 652 (2001).

13. Kennan, R. P., Scanley, B. E., Innis, R. B. and Gore, J. C. Physiological basis for BOLD MR signal changes due to neuronal stimulation: separation of blood volume and magnetic susceptibility effects. *Magn. Reson. Med.* **40**, 840-6 (1998).

14. Belliveau, J. W. et al. Functional mapping of the human visual cortex by magnetic resonance imaging. *Science* **254**, 716-9. (1991).

15. Dubowitz, D. J., Martinez, A. and McDowell, J. A simple setup for tracking eye position during fMRI. *Proc. Int. Soc. Magn. Res. Med.* **3**, 1691 (1999).

16. Cox, R. W. and Hyde, J. S. Software tools for analysis and visualization of fMRI data. *NMR Biomed.* **10**, 171-178 (1997).

17. Cox, R. W. and Jesmanowicz, A. Real-time 3D image registration for functional MRI. *Magn. Reson. Med.* **42**, 1014-8 (1999).

18. Coleman, T. F. and Li, Y. An interior trust region approach for nonlinear minimization subject to bounds. *SIAM J. Optim.* **6**, 418-445 (1996).

19. Butler, T. M. et al. in *Nonhuman Primates in Biomedical Research: Biology and Management* (eds. Bennett, C. R. and Abee, R. H.) 257-334 (Academic Press, London, 1995).

20. Kwong, K. K. et al. Dynamic magnetic resonance imaging of human brain activity during primary sensory stimulation. *Proc. Natl. Acad. Sci. USA* **89**, 5675-9 (1992).

21. Turner, R. et al. Functional mapping of the human visual cortex at 4 and 1.5T using deoxygenation contrast EPI. *Magn. Reson. Med.* **29**, 277-9 (1993).

22. Mandeville, J. B. et al. Dynamic liver imaging with iron oxide agents: effects of size and biodistribution on contrast. *Magn. Reson. Med.* **37**, 885-90 (1997).

23. Dale, A. M. Optimal experimental design for event-related fMRI. *Hum. Brain Mapp.* **8**, 109-14 (1999).

24. Ahrens, E. T. and Dubowitz, D. J. Peripheral Somatosensory fMRI in Mouse at 11.7 T. *NMR Biomed.* **14**, 318-24 (2001).

25. Gati, J. S., Menon, R. S., Ugurbil, K. and Rutt, B. K. Experimental determination of the BOLD field strength dependence in vessels and tissue. *Magn Reson Med* **38**, 296-302 (1997).

4.8 Acknowledgment

We gratefully acknowledge J. Michael Tyszka for enlightened discussion and Betty Gillikin for help with animal handling and health care. This work was funded in part by grants from National Institutes of Health (GM08042 and EY07492) and a James G. Boswell Professorship (RAA).

Chapter 5 Peripheral Somatosensory fMRI in Mouse at 11.7 T

As discussed in the previous chapter, deoxyhemoglobin is only weakly paramagnetic. The magnetic susceptibility effect is not large, but can be increased dramatically at high field. In this chapter I present a series of experiments to investigate the feasibility of fMRI at very high magnetic field (11.7 T) using very large applied gradients. These studies are the first demonstration of fMRI at 11.7 T, and are also the first successful fMRI in a mouse.

5.1 Abstract

The feasibility of performing extremely high resolution somatosensory fMRI in anesthetized mice using BOLD contrast at 11.7 T was investigated. A somatosensory stimulus was applied to the hind limb of an α-chlorolose anesthetized mouse resulting in robust ($p<4x10^{-3}$) BOLD changes in somatosensory cortex and large veins. Percent modulation of the MR signal in cortex exceeded 7%. Experiments that artificially modulated the inspired oxygen tension were also conducted; the results revealed large, heterogeneous, BOLD contrast changes in the mouse brain. In addition, T_1, T_2, and T_2^* values in gray matter at 11.7 T were evaluated. Discussion of the sensitivity limitations of BOLD fMRI in the tiny mouse central nervous system is presented. These methods show

promise for the assessment of neurological function in mouse models of CNS injury and disease.

5.2 Introduction

The proliferation of genetically altered mouse strains, particularly those that resemble models of human neurological disease, has stimulated the development of methods to noninvasively assay mouse neuronal function. Towards this goal, we explore extremely high-resolution MRI, or magnetic resonance microscopy (MRM), as a means of probing mouse neurofunction. MRM is proven to be highly effective in visualizing fine structures of the mouse central nervous system (CNS) in both fixed[1-4] and *in vivo*[5,6] subjects.

Functional MRI (fMRI) has emerged as a powerful tool for investigating functional organization in the mammalian brain[7]. fMRI does not detect neuronal activation directly, but instead probes secondary changes; these include regional changes in cerebral blood volume (CBV), cerebral blood flow (CBF), and blood oxygenation, which give rise to the widely used BOLD (Blood-Oxygen-Level-Dependent) contrast mechanism[8]. BOLD contrast originates from regional perturbations in the magnetic susceptibility of brain tissue due to changes in the relative amounts of oxyhemoglobin to deoxyhemoglobin in the capillary bed, venules, and veins. These perturbations strongly impact the MR parameters T_2 and T_2^* because deoxyhemoglobin is paramagnetic, whereas oxyhemoglobin is diamagnetic[9]. The relationships between changes in oxidative metabolism by activated neurons and the regional recruitment of excess blood oxyhemoglobin is an active area of investigation[7,10].

Although several groups have reported BOLD activation in rats,[11-18] mice are roughly an order of magnitude smaller in size. Consequently, extremely high signal-to-noise ratio (SNR) and resolution imaging capabilities are required, and this necessitates working at extremely high magnetic field strengths. In addition, anesthesia is required to immobilize the animals, however, its effects must not render cortical activity quiescent. Furthermore, reproducibility of the fMRI response demands that mouse physiology remain stable.

In this paper we investigate the feasibility of examining functional activation in anesthetized mice using MRM and intrinsic BOLD contrast mechanisms. These experiments were conducted at 11.7 T. First, we describe the results of *in vivo* measurements of the key magnetic resonance parameters T_1, T_2, and T_2^* in the mouse brain. Knowledge of these parameters allows for optimum BOLD imaging. Next, we describe experiments demonstrating that the magnitude of BOLD contrast in the mouse brain can reach dramatic levels at 11.7 T; these experiments involved artificial modulation of the inspired oxygen tension. From these data, a map of the relative sensitivity of various brain regions to controlled changes in blood oxygenation was derived. We then describe fMRI experiments in which a periodic somatosensory stimulus was applied to the mouse hind limb. Correlated functional maps were obtained indicating localized neuronal activation within cortical regions. Significant activation was also observed within large draining veins in subarachnoid regions. Our results demonstrate some of the limitations of using BOLD imaging for mouse-sized subjects at extremely high magnetic field strengths. We discuss these limitations in terms of the relationships

among the size of the neuro-anatomical functional unit, the SNR, and the spatial/temporal resolution.

5.3 Experimental

5.3.1 MRM Instrumentation

Image data were acquired using a Bruker AMX 500 microimaging system (Bruker Instruments Inc., Billerica, MA) with a 89 mm vertical bore 11.74 T magnet. An optimized laboratory-built 1 cm diameter surface coil imaging probe was utilized for the BOLD contrast imaging and the T_2^* measurements. This probe incorporates a stereotaxic head restraint in order to limit head motion and a mask that loosely fits over the animal's nose and mouth to administer inhalation gases. A 30 mm diameter birdcage volume coil was used for the T_1 and T_2 measurements in order to ensure a homogeneous RF refocusing pulse. The mouse temperature was regulated at 37 °C using a temperature regulated collet surrounding the animal connected to a closed-cycle water bath. These studies were conducted at the Biological Imaging Center at the California Institute of Technology, Pasadena, CA and were approved by the Institutional Animal Care and Use Committee.

5.3.2 MR Relaxation Times in the *In Vivo* Mouse Brain

Maps of the relaxation times T_1, T_2 and T_2^* were calculated within a single coronal brain slice. Adult female mice (~19 g, C57BL) were anesthetized using a intraperitoneal (IP) injection of a cocktail containing ketamine (0.07 mg/g) and xylazine (0.004 mg/g). The mouse was then mounted into the imaging probe and positioned into the magnet bore. After approximately 30 minutes, gaseous isoflurane (0.6% in air) was administered *in situ* in order to maintain the mouse under light anesthesia for the duration of the imaging session.

The T_1 and T_2 data were acquired using a saturation-recovery two-dimensional Fourier transform (2DFT) spin-echo protocol. All measurements were made on a single coronal brain slice. For T_1, seven images were collected with TR ranging from 0.3 to 13 s and TE=8 ms. The T_2 was obtained using ten single-echo images with TE-values ranging from 4.5 to 90 ms and TR=10 s. The T_2^* values were obtained using the same surface coil probe used for the fMRI experiments and using a 2DFT gradient-echo protocol using one line of k-space per excitation and a small tip-angle RF pulse; the TE-values were varied in 10 steps ranging from 4.5 to 50 ms and TR=50 ms. Field shimming was performed manually on the image slice. This was performed by turning off the read-out gradient and manually maximizing the integrated echo intensity by adjusting the shim currents on the eight lowest-order shims (based on the spherical harmonics). All data were acquired with 128×128 image points and a resolution of 117 μm in-plane, with a slice thickness of 1.5 mm.

For each data set we used a voxel-wise least squares fitting routine. The appropriate single-exponential recovery functions for T_1, T_2, and T_2^* were utilized[19]. From the maps of calculated relaxation times, regions of interest (ROI) were defined to obtain average relaxation time values in various brain regions. All measurements were repeated using the above procedures for N=4 mice.

5.3.3 Characterizing BOLD Contrast by Modulation of Inspired Oxygen Tension

Mice were anesthetized and prepared for imaging using the same methods as described above (Section 2b). Blood oxygen was modulated by alternating the inhalation gas between 100% O_2 and a mixture of 10% O_2 / 90% N_2. Previous studies[20] have shown that this gas combination perturbs the CBV and CBF by only a small amount (~10%). We assumed that the observed intensity changes are primarily due to modulation of blood oxygenation, and we ignored small contributions from CBV and CBF to the overall BOLD signal. Each gas was delivered for a period of one minute, and the gases were alternated for five cycles.

Gradient-echo images were acquired continuously within a single coronal brain slice during the five gas cycles. Images were primarily T_2^*-weighted, and multiple experimental runs were performed at various TE-values ranging from 4.5 to 12 ms. A small tip-angle excitation pulse (~3°) was utilized with TR=60 ms, two k-space averages,

and an imaging time of 15 s per slice. Thus, four imaging slices were acquired for each one-minute gas exposure, or 8 time-points per complete cycle. The image resolution was 98 μm in-plane, with a 1.0 mm slice thickness. These experiments were repeated in N=4 mice. Anatomical images were acquired using a 2DFT gradient-echo protocol with TR/TE=60/5.4 ms, an in-plane resolution of 98 μm, and a 1.0 mm slice thickness. The shimming method followed the same protocol used in the relaxation-time experiments.

The time-dependent image data were processed off-line using AFNI software[21]. In order to pick out voxels exhibiting significant intensity changes due to hypoxia, we performed a voxel-by-voxel cross-correlation analysis. A linear fit function of the form

$$x(t)=ar(t)+b \qquad [1]$$

was used, where $x(t)$ is the time-dependent voxel intensity, $r(t)$ is a trapezoidal model intensity function (or "stimulus" waveform), a is the fit coefficient, b is the baseline intensity in the hypoxic state, and t is time. The trapezoid model varied form 0 to 1 in amplitude, with a period of 8 time periods and one time period allotted to ramp up or down. To remove spurious pixels, the functional intensity map was threshold at a correlation-coefficient value of $|r| > 0.5$ (uncorrected $p < 0.01$). A map of the percent image intensity changes, given by $\Delta I=(a/b)\times 100\%$, was calculated and superimposed onto the anatomical image using AFNI. A rainbow color scale was used to represent the magnitude of the percent change (ΔI).

5.3.4 fMRI

Adult mice (~19 g, strain C57BL) were anesthetized with gaseous isoflurane (1.5% in 100% O_2). After approximately 10 minutes an IP injection of α-chlorolose was administered (0.08 mg/g) while under isoflurane anesthesia. After an additional 20 minutes, the isoflurane was removed and the mouse was mounted into the surface coil imaging probe.

Two electrodes consisting of a single turn of fine copper wire coated with conductive jelly were wound around the hind paw in order to apply a small somatosensory electrical stimulation (~50 μA). The periodic stimuli consisted of five 65-second pulses of 3 Hz stimulation interspersed by "off" periods of the same duration. The stimuli were far below the threshold needed to induce a visible motor response. A computer running a Labview software program (National Instruments Inc., Austin, TX) was used to orchestrate the stimulus and image acquisitions.

Para-sagittal images were acquired on a single slice offset approximately 2 mm from the midline using a gradient-echo method. The imaging parameters were TR/TE=17/7 ms, 64x64 image points, an in-plane image resolution of 180 μm, a 1.5 mm thick slice, and 10 averages. The TE-value was set to approximately the measured value of T_2^* in cortex (see Section 3a). The total imaging time for a single slice was approximately 11 seconds. Images were acquired continuously throughout the on and off stimulus periods. Spin-echo T_2-weighted anatomical images were acquired with TR/TE=1200/34 ms, an in-plane

resolution of 45 μm, and a 1.5 mm slice thickness. Shimming followed the same protocol described earlier

The time-dependent data were processed off line using a linear fit (Eq. 1) and the AFNI analysis software described above (Section 2c). Functional images were generated using a cross-correlation technique[22]. A series of phase-shifted trapezoids were used as the model stimulus reference waveforms; these were cross-correlated on a voxel-by-voxel basis with the MR signal time-course. A hot-body color scale was used to represent the magnitude of the fit coefficient. Spurious pixels were removed with a threshold set at a correlation-coefficient value of $|r| > 0.6$ ($p < 4x10^{-3}$ following a conservative Bonferroni correction for multiple comparisons). The anatomical image and the functional maps were co-registered using AFNI.

5.4 Results

5.4.1 MR Relaxation Times in the *In Vivo* Mouse Brain

From the maps of T_1, T_2, and T_2^*, ROI were defined in cortical gray matter in order to determine mean values. The results are T_1=1.9±0.1 s, T_2=31.4±1.1 ms, and T_2^*=7-28 ms. These results represent average values over ROIs containing approximately 50 voxels. For T_1 and T_2, the uncertainty represents the standard deviation of the mean for N=4

subjects. A calculated map of the T_2* values through a coronal slice is displayed in Figure 5.1. A substantial amount of T_2^* heterogeneity is observed, with values tending to increase smoothly in a dorsal-ventral fashion; values of order of 7 ms were observed near the dorsal-most cortical regions and increase to ~28 ms in ventral brain regions.

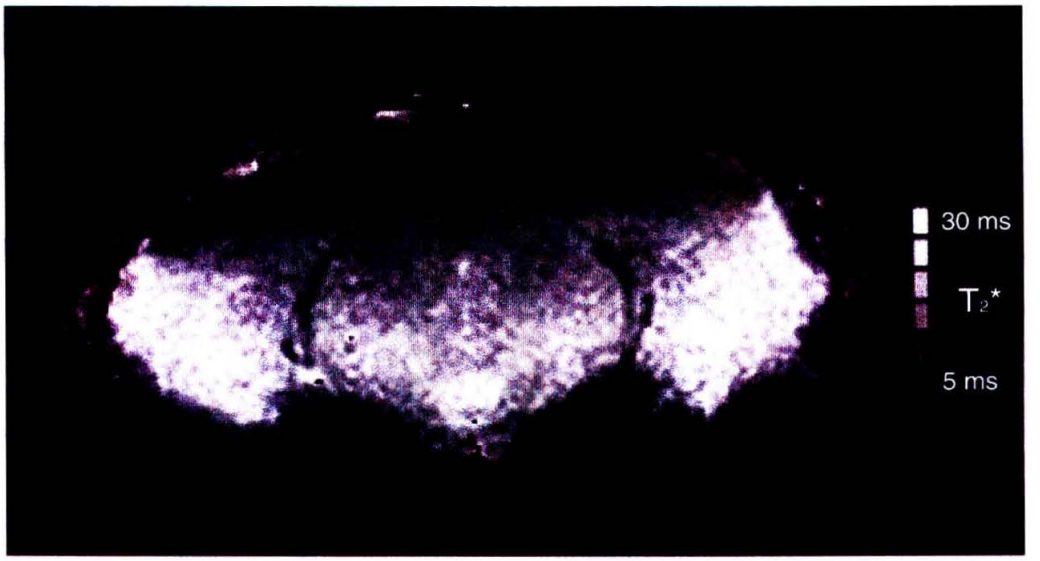

Figure 5.1 Calculated T_2^* map through a coronal brain slice. Data were acquired using a 2DFT gradient-echo sequence with a small tip-angle RF pulse; the TE values were varied in 10 steps ranging from 4.5 to 50 ms and TR=50 ms. Resolution is 117 μm in-plane, with a slice thickness of 1.5 mm. Note the large T_2^* heterogeneity observed across the slice.

5.4.2 BOLD Contrast by Modulation of Oxygen Tension

Figure 5.2 shows a coronal map of the percent changes in image intensity (ΔI) resulting from changes in blood oxygenation. Intensity changes in brain parenchymal tissue are of

order of 10–20%. Prominent signal changes are observed in proximity to large vessels, especially the sagittal sinus (~150%).

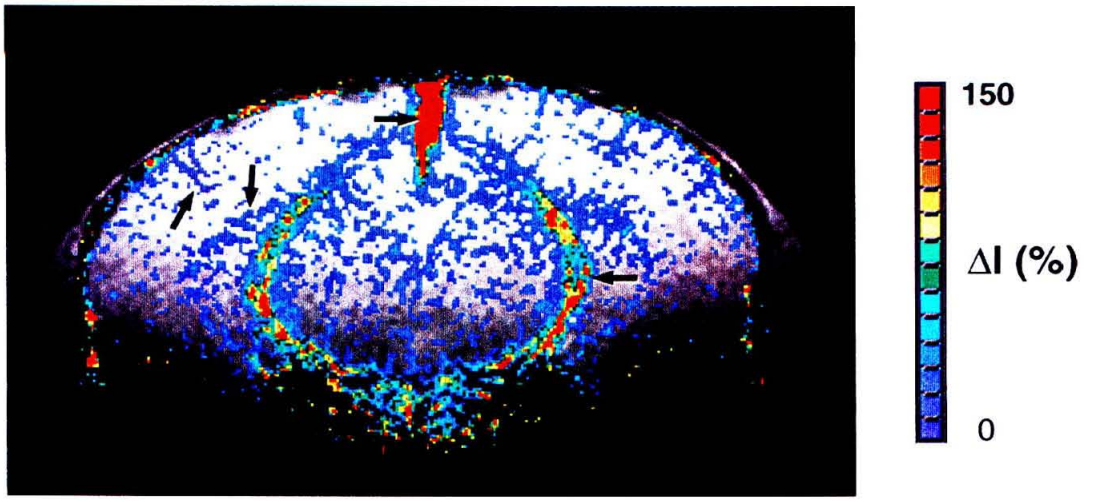

Figure 5.2 Coronal brain map of BOLD intensity changes due to hypoxia. Shown is a map of the percent intensity changes calculated from $\Delta\mu I=(a/b)\times 100\%$ (see text and Eq. [1]) and displayed in rainbow scale; the map is superimposed onto an anatomical image. These results demonstrate the heterogeneity of BOLD contrast in the brain and the potential high-sensitivity of this mechanism at 11.7 T. Blood-oxygen content was modulated in an anesthetized mouse by alternating the inhalation gas between 100% O_2 and a mixture of 10% O_2 / 90% N_2. T_2^*-weighted gradient-echo images were acquired continuously during multiple gas cycles. These data were acquired with TR/TE=60/6.8 ms, 98 μm in-plane resolution, and a 1 mm slice thickness. A cross-correlation analysis was used to threshold only those voxels exhibiting significant intensity changes (uncorrected $p<0.01$). The data was overlaid onto an anatomical image acquired in the same image plane. Substantial changes are observed in large draining veins, arteries, and parenchymal tissue. Black arrows indicate (from left to right) capillary networks in cortex and hippocampal regions, the sagittal sinus, and pial vessels.

5.4.3 fMRI

Figure 5.3 (center panel) shows a map of voxels exhibiting stimulus-correlated intensity changes; a para-sagittal anatomical image is also superimposed. The functional map shows robust activation ($p<4x10^{-3}$, corrected for multiple comparisons) in somatosensory cortex. Large draining veins in subarachnoid regions also exhibit a substantial modulation in intensity. The data shown are on the side contralateral to the stimulus. Data on the ipsilateral side (not shown) shows no significant activation.

Panels 3a-c display the time course of voxel intensities for various ROI. Shown are the somatosensory cortex (a), the transverse sinus (b), and the sagittal sinus (c). The model stimulus function is indicated by the solid red trace in the middle frame of each panel. The percent modulation of the ROI intensities were approximately 7%, 20%, and 15% for the somatosensory cortex, transverse sinus, and sagittal sinus, respectively. These values where calculated from $\Delta I=(a/b)\times 100\%$, where the parameters were obtained from the model fit of data (described by Eq. [1]).

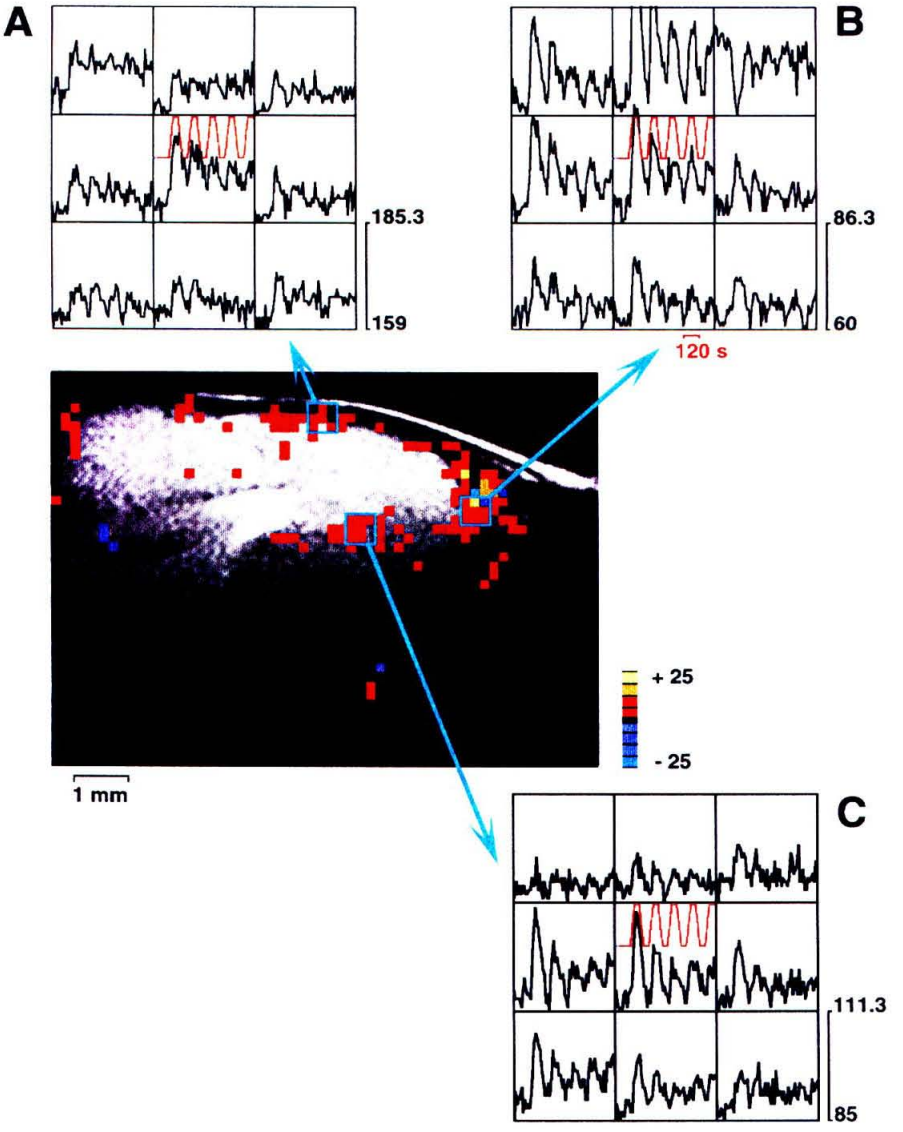

Figure 5.3 fMRI map in the mouse brain resulting from a somatosensory stimulus to the hind limb. The fMRI map (center panel) is overlaid onto a para-sagittal anatomical image. The slice is contralateral to the stimulated side. There is strong activation ($p<4x10^{-3}$) in somatosensory regions and in large draining veins. Figures 5.3a-c show the time course of the voxel intensities of the raw data for various ROI. Shown are the somatosensory cortex (a) and large draining veins (b-c). The model stimulus function is drawn in the middle frame of each panel. The percent modulation of the MR signal in the ROI, calculated from the second stimulus period, are approximately 7%, 20%, and 15% for the somatosensory cortex, transverse sinus, and draining vein, respectively.

For reference, Figures 5.4a-b show schematic diagrams of various aspects of mouse brain anatomy. Figure 5.4a shows a para-sagittal tracing in approximately the same location as the fMRI slice shown in Figure 5.3. The primary somatosensory areas are indicated. Figure 5.4b shows a dorsal view of the mouse superficial venous system; the approximate location of the fMRI slice of Figure 5.3 is indicated by a shaded bar. Note that the image plane intersects several large draining veins, especially the transverse sinus, which shows up in the correlation map (Figure 5.3).

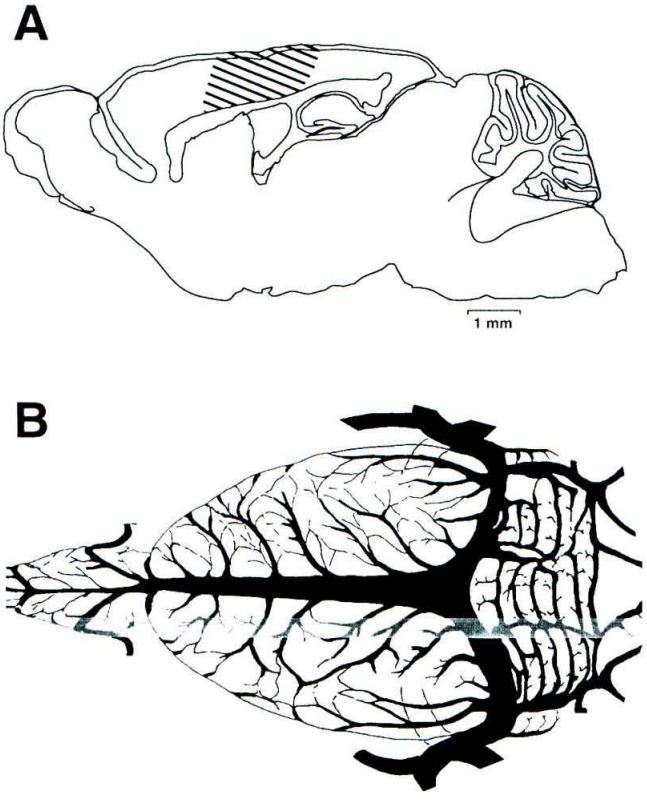

Figure 5.4 Anatomy of mouse brain. Figure 5.4a shows a diagram of a para-sagittal cross section. The limb somatosensory cortical regions are shaded. Figure 5.4b shows a dorsal view of the superficial venous system of a mouse. The approximate location of the image slice shown in Figure 5.3 is indicated in Figure 5.4b by a shaded bar. [Figure 5.4b is adapted from Paxinos[40]].

5.5 Discussion

5.5.1 Relaxation Times

The first step in the optimization of fMRI in mouse is the characterization of the longitudinal relaxation times T_1, T_2, and T_2^* in the brain which are magnetic field strength-dependent and may depend on species. The most important parameter for gradient-echo BOLD contrast imaging is T_2^* in parenchyma, where setting $TE \approx T_2^*$ maximizes the contrast-to-noise ratio[23]. The measured values of T_2^* varied by a factor of four (7-28 ms) across the brain slice (Figure 5.1). Presumably this heterogeneity is due to discontinuities in the magnetic susceptibility among different materials (i.e., air/bone/brain)[24] that give rise to macroscopic magnetic field gradients that cannot be removed with shimming. The spin-dephasing contribution to T_2^* due to susceptibility gradients is accentuated by working at extremely high magnetic fields[24]. In our fMRI and blood gas experiments, TE was set to a value of ~7 ms, which is approximately the T_2^*-value observed in the somatosensory cortex regions. The longest T_2^*-values (~28 ms) were observed in regions near the basal ganglia and are comparable to T_2 in parenchyma (31.4 ms).

The value of T_2=31.4 ms measured in parenchyma is significantly less than values obtained in other species at lower fields. For example, T_2-values in rat gray matter at 9.4 and 4.7 T are reported to be 40 and 50 ms, respectively[12,25], and in humans T_2=101 ms at 1.5 T[26]. Interestingly, at 11.7 T the ratio of T_1/T_2=60.5 is exceedingly large. By

comparison, T_1/T_2=9 at 1.5 T (in human gray matter)[26]. Because the imaging time increases monotonically with the parameter T_1/T_2[27], this observation highlights one of the fundamental difficulties associated with the implementation of rapid-imaging methods at extremely high magnetic field strengths.

5.5.2 Modulation of Oxygen Tension

In order to investigate the sensitivity and spatial distribution of apparent BOLD effects in the mouse brain at 11.7 T, we investigated image changes in response to the modulation of the inspired oxygen tension; the combination of gases used minimizes perturbations in CBF and CBV[20]. Theoretical analysis suggests that T_2^* and BOLD-contrast changes in proximity to vessels are strongly dependent on magnetic field strength[28].

Using the inhalation gas assay, the magnitude of BOLD intensity changes in parenchyma are at the 10-20% level and of order 150% in large vessels (Figure 5.2). Changes in parenchyma are presumably due to blood-oxygenation variations in the capillary bed. We note that the potential intensity changes may in fact be significantly larger than what we have described for two reasons. First, the changes in parenchyma did not completely saturate to a constant value after one minute exposure to hypoxic conditions. [This is in contrast to the large vessels (e.g., sagittal sinus) where intensity changes saturated in < 20s.] Exposure to hypoxic conditions was not continued beyond one minute in order to avoid harming the animal. Second, the experiments were repeated for a range of TE-values, but due to the shortness of T_2^* in dorsal-most brain regions only the TE=6.8 ms

data was used to ensure adequate SNR throughout the slice for the cross-correlation analysis; this TE-value does not optimize the BOLD-changes in all brain regions.

5.5.3 fMRI

The intent of these studies was to determine whether BOLD contrast fMRI is effective in analyzing mouse neurofunction. The results show significant cortical activation at the 7% level in limb somatosensory cortex (Figure 5.3); thus these methods show promise as a tool for elucidating normal neurofunction and neuropathology. We note that one other group has reported comparable magnitude BOLD signal changes in mouse in response to visual stimuli[29].

Our results also bring to light several limitations of the technique. These stem from ubiquitous SNR limitations of MRI and the temporal resolution limitations associated with working at extremely high magnetic field strengths. Furthermore, the need to work with anesthetized animals and the vertical orientation of the animal in the magnet bore may impact the results.

Performing fMRI in mouse is substantially more difficult than in rat, where robust BOLD signals have been observed by numerous groups. Consider the relative size of the cortical functional unit between these two species. Cortical somatosensory cytoarchitecture has a high degree of compartmentalization[30], and there is a similar organization in mouse and

rat[31]. For the sake of scaling arguments, consider the relative volume of a widely studied somatosensory unit, the whisker barrel cortex. From cytochrome oxidase-stained tangential sections of flattened cortex, the measured mean area ratio of mouse to rat barrels is of order of 0.2 (Woolsey, TA – Private communication), and an estimate of the volume ratio is of order of 0.09. Thus, the volume of the functional unit is approximately ten times smaller in mouse than in rat, and the voxel volume needs to be approximately ten times smaller to achieve the same degree of cortical localization. Because SNR is proportional to voxel volume, there is a substantial loss in sensitivity when attempting to resolve the mouse functional unit. Although the whisker barrel is used as an example here, we speculate that the same relative sizes apply to somatosensory limb regions.

Some of the loss in SNR can be recovered by working at a higher magnetic field strength. For example, increasing the imaging field strength from 9.4 T (the highest field fMRI results in rat reported to date) to 11.7 T provides a SNR gain of order of 50%. This assumes a $B_0^{7/4}$ -dependence of SNR on field strength (B_0) and all other parameters held constant[27]. In addition to the gains in SNR by going to higher field strength, one also gains in the sensitivity to BOLD contrast due to heightened local field gradients in proximity to vessels. Numerical simulations show the BOLD contribution to the transverse relaxation rate scales linearly with B_0 for large vessels and quadratically for small vessels (compared to the voxel size)[32]. Quantitative verification of these scaling relations in the brain is problematic due to partial volume contamination and uncertainties in numerous parameters[33]. Although there is a lack of quantitative data for the field strengths utilized in this study, on the basis of the theoretical estimates and extrapolation

of lower field results[33], going from 9.4 to 11.7 T yields an increase of less than a factor of two in the functional contrast-to-noise ratio (CNR). The upshot is that, although the image SNR (and resolution) and BOLD CNR is improved by moving to higher field strengths, the improvement may not be sufficient to offset the reduced sensitivity due to the very small size of the functional structures in mouse compared to rat. We have chosen a conservative Bonferroni correction for multiple comparisons even though this may increase the number of false negative observations. This was deemed preferable to having a larger number of false positive observations.

In addition to cortical activation, the fMRI results (Figure 5.3) show substantial correlated intensity changes in large draining veins that are distant from the activated neurons. At least two factors may play a role in this behavior. Changes in arterial and venous CBF may accompany the stimulus. This results in an "in-flow" effect where fully magnetized spins flow into the imaging plane and modulate the image intensity in a correlated fashion. In-flow effects may also provide a contribution to the large intensity changes observed in vessels in the blood-gas experiments (Figure 5.1), although the gas combination used was designed to minimize these effects. We have made no attempt to quantify in-flow contributions in the present studies, and this is a topic of future work.

A second consideration stems from the relatively low temporal resolution (~10 s per image) of the fMRI data; the long acquisition times are a consequence of the high spatial resolution and the necessity for signal averaging in order to obtain satisfactory SNR. Optical studies have examined the temporal relationships between CBF, CBV, and blood

oxygenation[34] of the BOLD response following neuronal stimulation. These studies show that the initial deoxyhemoglobin increase is well localized with the sites of elevated neuronal firing, and that the later oxyhemoglobin increase is less localized; also, increasing the stimulus duration reduces the signal-to-noise ratio of the activation maps[34]. Recent fMRI studies in cat[35] have shown that activation maps generated at different time points along a biphasic BOLD response display varying degrees of neuronal localization; maps from the initial negative dip show greater neuronal localization compared to those from the latter positive BOLD response which show substantial venous recruitment. Although a biphasic BOLD response in mouse has not been demonstrated using MRI, we speculate that mouse data acquired with better temporal resolution and with a shorter duration stimulus period may provide better localization of neuronal function and less involvement of large vessels.

Improving the temporal resolution requires implementation of rapid-imaging methods that work satisfactorily at 11.7 T. One is at a disadvantage at 11.7 T because of the large T_1/T_2 ratio[27]. Furthermore, the shortness of T_2^* and the persistence of B_0 inhomogeneities at these extreme field strengths makes implementation of artifact-free single-shot echo-planar imaging (EPI) problematic. The use of rapid spin-echo (SE) imaging methods (i.e., RARE[36]) may provide the best means of speeding-up acquisitions as well as reducing bulk susceptibility artifacts[37]. In addition, it is has been suggested that SE methods are less sensitive to dephasing of large vessels and more sensitive to microvasculature[12]. We also note that the use of bipolar diffusion gradients to attenuate

spins with high mobility in large vessels may also be useful in this regard[38]. These are topics for future work.

Two additional experimental considerations that may impact our results are the physiological effects of anesthesia and the vertical orientation of the mouse in the magnet bore. It is desirable to work with anesthetized animals in order to immobilize the animal and minimize stress during imaging. α-Chlorolose was used as the primary anesthesia for fMRI experiments because it does not significantly depress cortical activity[18], provides a stable CBF[39], and has been used successfully in numerous BOLD somatosensory studies in rat. Care must be taken when using this anesthesia because there is a tendency to induce seizures after an initial injection, and thus it was administered to the animal while it was under the influence of isoflurane.

The other potential complication originates from the orientation of the animal in a vertical position within the magnet bore. Maintaining a mouse in this unnatural orientation for extended time periods may lead to physiological changes, particularly blood pressure disturbances, incomplete blood-gas exchange due to respiratory difficulties, decreased cardiac output, and changes in cerebral perfusion. Furthermore, because anesthetic agents reduce vasoconstrictor tone, the adverse effects of the vertical posture may become exacerbated. Little is known about how these effects may alter the outcome of the fMRI experiment, and this area needs further investigation.

5.6 Conclusions

We demonstrate the feasibility of peripheral somatosensory fMRI in mouse utilizing BOLD contrast mechanisms. These results are the first step in defining the spatial and temporal signatures of the BOLD effect in mouse, which is largely unknown. The refinement of these fMRI methods will permit quantitative assessment of neurological function in mouse models of CNS injury and disease, particularly those involving genetically manipulated lines; the repertoire of such techniques that are noninvasive is currently limited. Challenges remain in developing these methods for true quantitative studies. The SNR is a concern even at the extremely high magnetic field strengths used in this study. Improved methods for artifact-free rapid imaging that are suitable for working at these field strengths are also needed. In addition, new tools for the precise control of mouse physiology in the confines of the magnet bore need to be developed and refined. Finally, further exploration is necessary into the effects of various anesthesia types on mouse neurofunction.

5.7 References

1. Ahrens, E. T. et al. MR microscopy of transgenic mice that spontaneously acquire experimental allergic encephalomyelitis. *Magn. Reson. Med.* **40**, 119-32 (1998).

2. Ahrens, E. T., Blumenthal, J., Jacobs, R. E. and Giedd, J. N. in *Brain Mapping: The Systems.* (eds. Toga, A. W. and Mazziotta, J. C.) 561-589 (Academic Press, San Diego, 2000).

3. Jacobs, R. E., Ahrens, E. T., Meade, T. J. and Fraser, S. E. Looking deeper into vertebrate development. *Trends Cell Biol* **9**, 73-6 (1999).

4. Benveniste, H., Kim, K., Zhang, L. and Johnson, G. A. Magnetic resonance microscopy of the C57BL mouse brain. *Neuroimage* **11**, 601-11 (2000).

5. Dubowitz, D. J. et al. High resolution magnetic resonance imaging of the brain in the dy/dy mouse with merosin-deficient congenital muscular dystrophy. *Neuromuscul. Disord.* **10**, 292-8 (2000).

6. Pautler, R. G., Silva, A. C. and Koretsky, A. P. In vivo neuronal tract tracing using manganese-enhanced magnetic resonance imaging. *Magn. Reson. Med.* **40**, 740-8 (1998).

7. Ogawa, S., Menon, R. S., Kim, S. G. and Ugurbil, K. On the characteristics of functional magnetic resonance imaging of the brain. *Annu. Rev. Biophy.s Biomol. Struct.* **27**, 447-74 (1998).

8. Ogawa, S., Lee, T. M., Kay, A. R. and Tank, D. W. Brain magnetic resonance imaging with contrast dependent on blood oxygenation. *Proc. Natl. Acad. Sci. USA* **87**, 9868-9872 (1990).

9. Pauling, L. and Coryell, C. D. The magnetic properties and structure of hemoglobin, oxyhemoglobin and carbonmonoxyhemoglobin. *Proc. Natl. Acad. Sci. USA* **22**, 210-216 (1936).

10. Hoge, R. D. et al. Investigation of BOLD signal dependence on cerebral blood flow and oxygen consumption: the deoxyhemoglobin dilution model. *Magn. Reson. Med.* **42**, 849-63. (1999).

11. Burke, M., Schwindt, W., Ludwig, U., Hennig, J. and Hoehn, M. Facilitation of electric forepaw stimulation-induced somatosensory activation in rats by

additional acoustic stimulation: an fMRI investigation. *Magn Reson Med* **44**, 317-21 (2000).

12. Lee, S. P., Silva, A. C., Ugurbil, K. and Kim, S. G. Diffusion-weighted spin-echo fMRI at 9.4 T: microvascular/tissue contribution to BOLD signal changes. *Magn. Reson. Med.* **42**, 919-28 (1999).

13. Lahti, K. M., Ferris, C. F., Li, F., Sotak, C. H. and King, J. A. Imaging brain activity in conscious animals using functional MRI. *J. Neurosci. Methods.* **82**, 75-83 (1998).

14. Yang, X. et al. Dynamic mapping at the laminar level of odor-elicited responses in rat olfactory bulb by functional MRI. *Proc. Natl. Acad. Sci. USA* **95**, 7715-20 (1998).

15. Mandeville, J. B. et al. Dynamic functional imaging of relative cerebral blood volume during rat forepaw stimulation. *Magn. Reson. Med.* **39**, 615-24 (1998).

16. Bock, C. et al. Functional MRI of somatosensory activation in rat: effect of hypercapnic up-regulation on perfusion- and BOLD-imaging. *Magn. Reson. Med.* **39**, 457-61 (1998).

17. Yang, X., Hyder, F. and Shulman, R. G. Functional MRI BOLD signal coincides with electrical activity in the rat whisker barrels. *Magn. Reson. Med.* **38**, 874-7 (1997).

18. Yang, X., Hyder, F. and Shulman, R. G. Activation of single whisker barrel in rat brain localized by functional magnetic resonance imaging. *Pro.c Natl. Acad. Sci. USA* **93**, 475-8 (1996).

19. Hendrick, R. E. and Raff, U. in *Magnetic Resonance Imaging* (eds. Stark, D. D. and Bradley, W. G., Jr.) 109-144 (Moseby Year Book, St Louis, 1992).

20. Kennan, R. P., Scanley, B. E. and Gore, J. C. Physiologic basis for BOLD MR signal changes due to hypoxia/hyperoxia: separation of blood volume and magnetic susceptibility effects. *Magn. Reson. Med.* **37**, 953-6 (1997).

21. Cox, R. W. and Hyde, J. S. Software tools for analysis and visualization of fMRI data. *NMR Biomed.* **10**, 171-178 (1997).

22. Bandettini, P. A., Jesmanowicz, A., Wong, E. C. and Hyde, J. S. Processing strategies for time-course data sets in functional MRI of the human brain. *Magn. Reson. Med.* **30**, 161-173 (1993).

23. Menon, R. S., Ogawa, S., Tank, D. W. and Ugurbil, K. 4 Tesla gradient recalled echo characteristics of photic stimulation-induced signal changes in the human primary visual cortex. *Magn. Reson. Med* .**30**, 380-6 (1993).

24. Yang, Q. X., Smith, M. B., Briggs, R. W. and Rycyna, R. E. Microimaging at 14 tesla using GESEPI for removal of magnetic susceptibility artifacts in T_2*-weighted image contrast. *J. Magn. Reson.* **141**, 1-6 (1999).

25. van Zijl, P. C. et al. Quantitative assessment of blood flow, blood volume and blood oxygenation effects in functional magnetic resonance imaging. *Nat. Med.* **4**, 159-67 (1998).

26. Wood, M. L., Bronskill, M. J., Mulkern, R. V. and Santyr, G. E. Physical MR desktop data. *J. Magn. Reson. Imaging.* **3 Suppl**, 19-24 (1993).

27. Callaghan, P. T. *Principles of Magnetic Resonance Microscopy* (ed.) (Oxford University Press, New York, 1991).

28. Ogawa, S. et al. Functional brain mapping by blood oxygenation level-dependent contrast magnetic resonance imaging. A comparison of signal characteristics with a biophysical model. *Biophys. J.* **64**, 803-12 (1993).

29. Huang, W. et al. Magnetic resonance imaging (MRI) detection of the murine brain response to light: temporal differentiation and negative functional MRI changes. *Proc. Natl. Acad. Sci. USA* **93**, 6037-42 (1996).

30. Woolsey, T. A. and Van der Loos, H. The structural organization of layer IV in the somatosensory region (SI) of mouse cerebral cortex. The description of a cortical field composed of discrete cytoarchitectonic units. *Brain Res.* **17**, 205-42. (1970).

31. Wallace, M. N. Histochemical demonstration of sensory maps in the rat and mouse cerebral cortex. *Brain Res.* **418**, 178-82. (1987).

32. Ogawa, S., Lee, T. M., Nayak, A. S. and Glynn, P. Oxygenation-sensitive contrast in magnetic resonance image of rodent brain at high magnetic fields. *Magn. Reson. Med.* **14**, 68-78 (1990).

33. Gati, J. S., Menon, R. S., Ugurbil, K. and Rutt, B. K. Experimental determination of the BOLD field strength dependence in vessels and tissue. *Magn. Reson. Med.* **38**, 296-302 (1997).

34. Malonek, D. et al. Vascular imprints of neuronal activity: relationships between the dynamics of cortical blood flow, oxygenation, and volume changes following sensory stimulation. *Proc. Natl. Acad. Sci. USA* **94**, 14826-31 (1997).

35. Kim, D. S., Duong, T. Q. and Kim, S. G. High-resolution mapping of iso-orientation columns by fMRI. *Nat. Neurosci.* **3**, 164-9 (2000).

36. Hennig, J., Nauerth, A. and Friedburg, H. RARE imaging: a fast imaging method for clinical MR. *Magn. Reson. Med.* **3**, 823-33 (1986).

37. Grieve, S. M., Blamire, A. M. and Styles, P. The effect of bulk susceptibility on murine snapshot imaging at 7.0 T: a comparison of snapshot imaging techniques. *Magn. Reson. Med.* **43**, 747-55 (2000).

38. Silva, A. C., Williams, D. S. and Koretsky, A. P. Evidence for the exchange of arterial spin-labeled water with tissue water in rat brain from diffusion-sensitized measurements of perfusion. *Magn. Reson. Med.* **38**, 232-7 (1997).

39. Lindauer, U., Villringer, A. and Dirnagl, U. Characterization of CBF response to somatosensory stimulation: model and influence of anesthetics. *Am. J. Physiol.* **264**, H1223-8 (1993).

40. Paxinos, G. *The Rat Nervous System* (Academic Press, Sydney, 1985).

5.8 Acknowledgment

We thank Drs. P. T. Narasimhan, Russell Jacobs, and Scott Fraser for valuable comments and Carlo Quinonez for assistance with Labview programming. This work is supported in part by a grant from the National Multiple Sclerosis Society (grant RG 3071A1/1) and the Human Brain Project (DA08944) with contributions from the National Institute on Drug Abuse and the National Institute of Mental Health, the NCRR (RR13625), and MH61223.

Appendix A Improving Behavioral Control in Monkey fMRI Studies

In comparing functional MRI studies between humans and animals, a key advantage of using a monkey as the animal model is the ability to study awake trained animals. This allows cognitive and perceptual tasks to be performed in the scanner and to observe the neuronal activation associated with them. For awake studies, the animal must be restrained within the scanner (in the interest of experimental compliance as well as safety and hygiene). The animal's behavior must also be carefully controlled. In this appendix, I will address three issues associated with the use of awake monkeys for functional MRI. These are: The design of MRI compatible restraints, strategies for behavioral training and reward, and a system for eye-tracking within the scanner.

A.1 Headpost Design

Functional MRI is very sensitive to gross head movement. Motion during the study by as little as half a voxel width will cause dephasing and misregistration of the signal. For human studies, the head is rigidly fixed with tight padding and often the use of a bite bar. For most animal studies, the animal is anesthetized and restrained with padding to reduce motion related to respiratory and cardiac pulsation. For awake monkey imaging, the same degree of rigid head fixation is needed, and cannot be achieved by training alone. The preferred method was to modify a plastic headcap for MR use — similar to those used for

conventional electrophysiology studies. Other methods were considered, e.g., applying a temporary "halo" with pins to the scalp under local anesthesia, constructing a tight-fitting helmet (similar to a motorcycle helmet), or training the animal to use a bite bar, but all were deemed to be less practical. Figure A.1 is a sagittal view of a monkey undergoing MRI for localization of a potential recording site. The animal had previously been trained for behavioral studies in an electrophysiology recording environment, and had a methylmethacrylate headcap attached with securing screws, grounding electrode, and connectors for eye-tracking using a scleral coil. The hardware associated with conventional electrophysiology experiments produces significant susceptibility artifacts, such that the entire brain is obscured (only the animal's snout and shoulders are clearly discernable). This highlights the need for customized hardware associated with MRI studies. To minimize these artifacts, the magnetic susceptibility of the materials must be similar to the sample under investigation (in this case brain).

Materials put into a magnetic field will become magnetized. The polarity and magnitude of this magnetic susceptibility, χ is a characteristic of the material, as described by equation 1.

$$\vec{M} = \chi \vec{H} \qquad [1]$$

where $\vec{M}$ is the induced magnetization, and $\vec{H}$ is related to the applied magnetic field. The susceptibility is negative ($\chi < 0$) for paramagnetic materials and positive ($\chi > 0$) diamagnetic materials. This induced magnetic field produces local gradients and in turn phase error which cause signal loss and distortion in the MRI image[1,2].

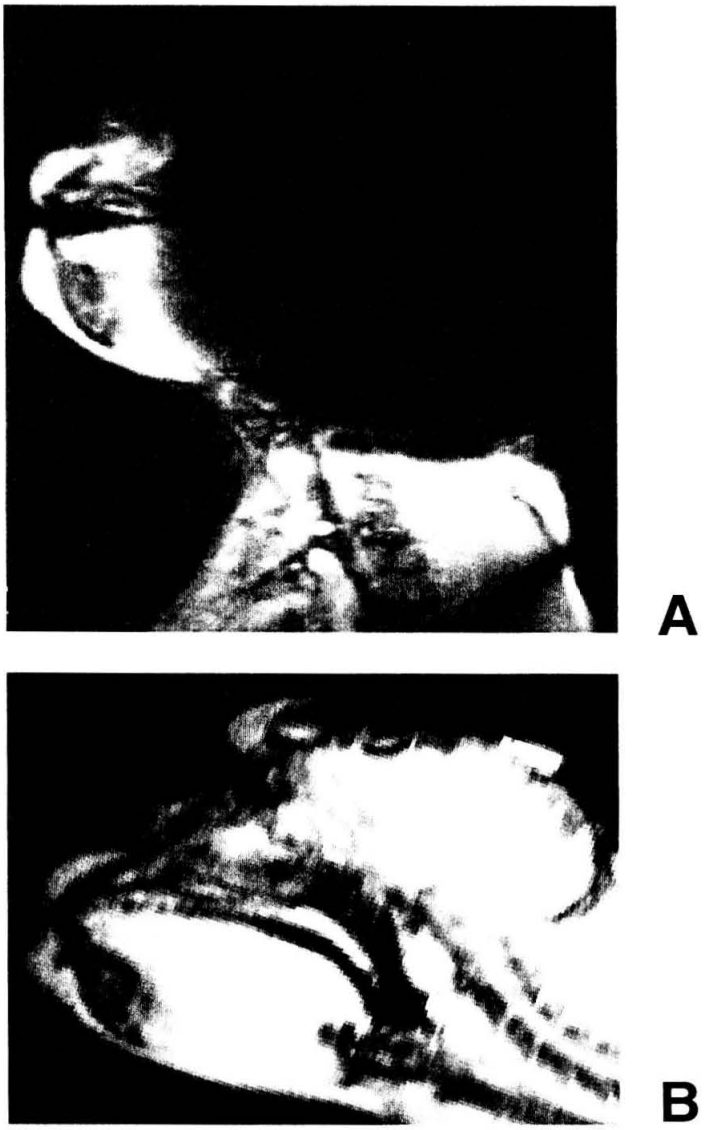

Figure A.1 Sagittal MRI of a macaque monkey (MPRAGE, see Table 3.1 for imaging parameters). Upper image (A) taken with a conventional headcap *in situ*. Note considerable signal loss and distortion in the MR image completely effacing the brain. Lower image (B) is the same monkey following replacement of the headcap with MR compatible components (non-ferrous screws and electrical connectors, and a plastic recording chamber).

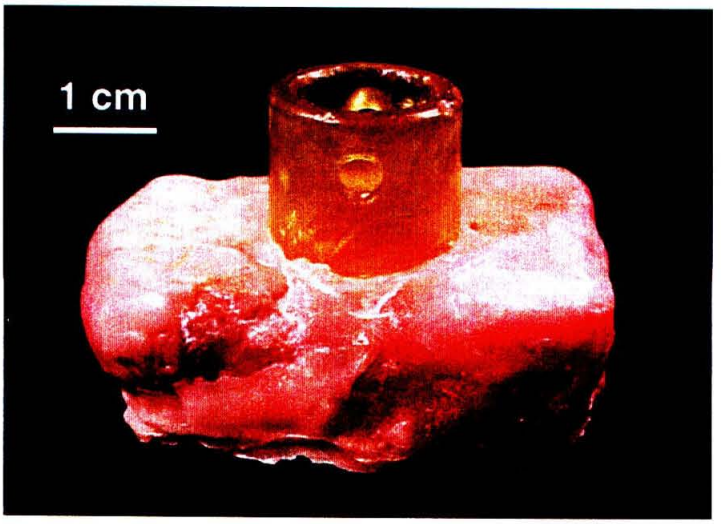

Figure A.2 Prototype MR compatible headcap made of polymethylmethacrylate with a polyetherimide post.

For the studies presented in Chapters 2, 3 and 4, the monkey needed to be restrained within the MR scanner. A combination of training and habituation were employed in addition to the use of a customized plastic head restraint. In designing the restraining headcap, a number of empirical designs were investigated, which are presented below. Polymethylmethacrylate is used for a number of orthotic devices (e.g., dentures) and has good biocompatibility and tensile strength making it ideal for use in a headcap. Figure A.2 shows a prototype design for a headcap using polymethylmethacrylate. The embedded post and the screws attaching the headcap to the skull were made of polyetherimide, which is inert, biocompatible and has susceptibility characteristics similar to biological tissues.

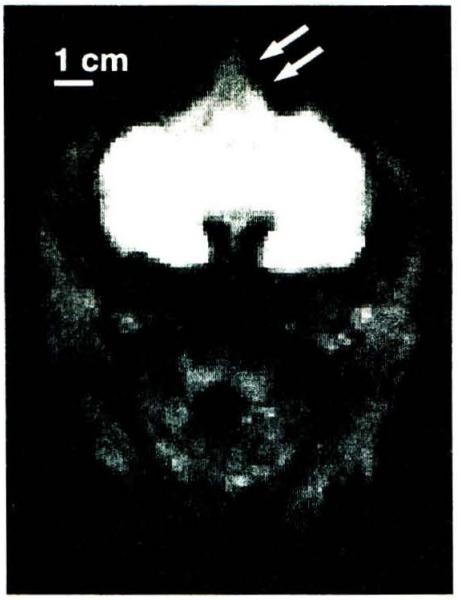

Figure A.3 Echo-planar coronal MRI (see Table 3.1 for imaging parameters). Susceptibility-induced distortion of the cortex (arrowed) due to polymethylmethacrylate in the headcap.

The magnetic susceptibility of polymethylmethacrylate is dissimilar to brain, and causes distortion of the echo-planar images (which are particularly sensitive to susceptibility gradients). These are demonstrated in Figure A.3. Areas of cortical activation occurring immediately adjacent to the polymethylmethacrylate would results in incorrect mapping of the cortical activation outside the calvarium. For the experiments presented in Chapter 2, the areas of interest in visual cortex were significantly posterior to the slice shown in Figure A.3 and were not distorted by the headcap — but this particular design has limitations for whole brain imaging. For the studies in Chapter 3, a new design of headcap was needed.

Reducing the polymethylmethacrylate in the headcap design removes much of the induced image distortion. To achieve this, a second headcap was designed, machined from a single piece of polyetherimide resin. The curvature of the undersurface of the cap was to match the convexity of the skull from measurements taken directly from anatomical MR images of the money's skull. Stronger screws were also used — immobilized with a minimum of polymethylmethacrylate. The headcap is shown in Figure A.4. This allowed whole brain imaging without significant distortion around the headcap. The use of polyetherimide screws imposed tensile limitations on the cap, as they were liable to shear under excessive force. To counter this, stronger screws were evaluated, in particular titanium and ceramic, which are commonly used in orthopedic procedures.

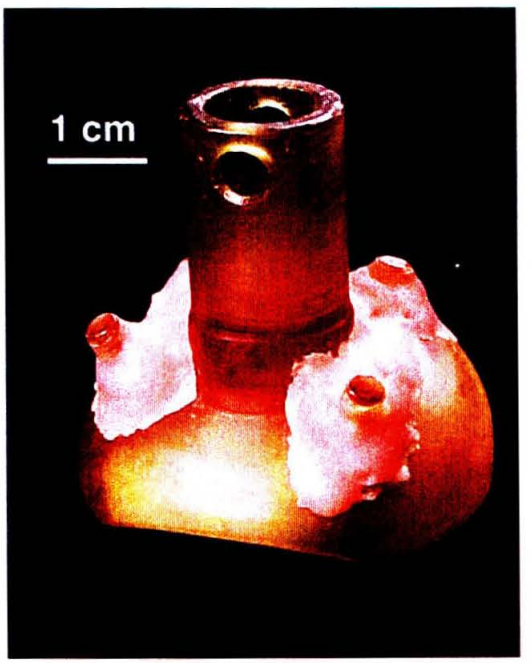

Figure A.4 Polyetherimide headcap with minimal polymethylmethacrylate.

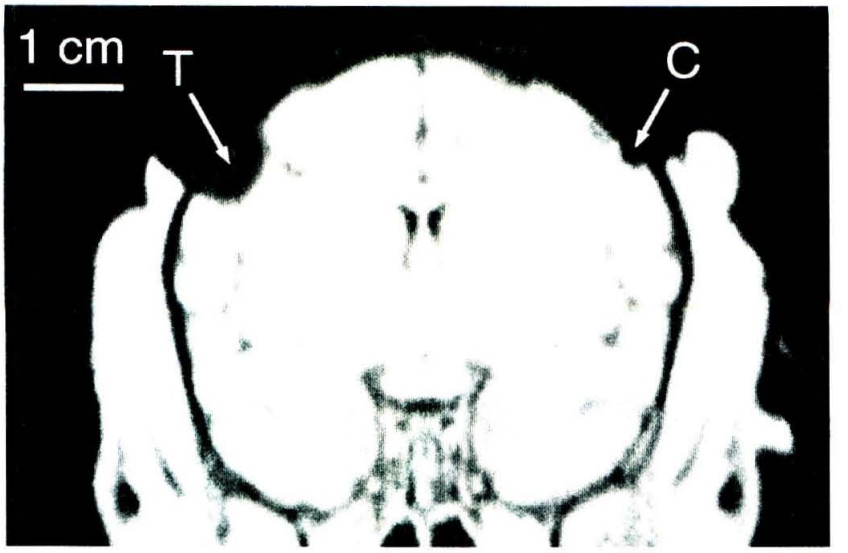

Figure A.5 Image distortion due to similar sized (2 mm) titanium (T) and ceramic (C) screws (MPRAGE imaging sequence, see Table 3.1 for parameters).

Ceramic screw do cause some susceptibility distortion, but the screw volume is small and the distortion is negligible. Although it is not ferromagnetic, titanium still causes substantial artifacts on fast gradient-echo imaging due to eddy currents. Figure A.5 shows the image distortion during an MPRAGE imaging sequence due to titanium and ceramic screws 2 mm in diameter. The titanium screws are inappropriate for functional MRI sequences where gradient switching is high and thus eddy currents are also large. They have a role for use in monkeys who require anatomical imaging, but not functional imaging.

Figure A.6 shows the modified headcap design. The ceramic screws were incorporated into the polyetherimide headcap design. They provide a stronger anchor than the

polyetherimide/polmethylmethacrylate screws. This allows whole head MR imaging with negligible susceptibility artifact. It also provides a robust anchor to position the monkey in the MR scanner. Details for anchoring the headcap inside the MR scanner are shown in Figure 2.3. The main disadvantage of this design is the time needed to individually machine the undersurface to the curvature of the monkey's head. A new headcap needs to be manufactured as the animal's head grows.

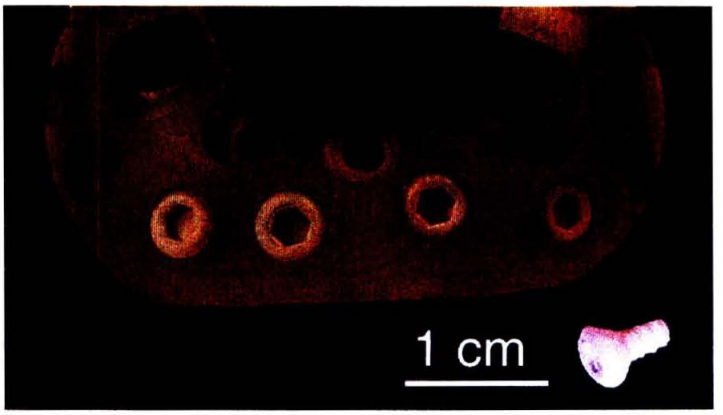

Figure A.6 Detail of polyetherimide headcap with ceramic screws.

A.2 Behavioral Training / Reward

The headcap described above provides good but not absolute immobilization. To achieve the high level of immobilization and co-operation necessary for functional MRI studies, the monkey still requires considerable training. For training purposes a simulator was built that incorporated many of the elements of the MR scanner. This allows the animal to become habituated and comfortable in the noisy MR environment and to train him for the

task under investigation. The monkey was trained to remain motivated for the studies by rewarding him with fruit juice at regular intervals during the study.

Monkeys used for electrophysiology studies typically receive fruit juice rewards every 1-2 seconds, however, the duration of a typical functional MRI experiment is several minutes. To assess if rewarding the monkey during acquisition of functional MRI data was detrimental, a study was performed in which the monkey took a sip of water once every 20 seconds while sitting motionless in the dark. The MR signal time course in visual cortex is shown in Figure A.7. There is significant motion-induced modulation in the MR signal in visual cortex due to motion of the pharynx and muscles of mastication.

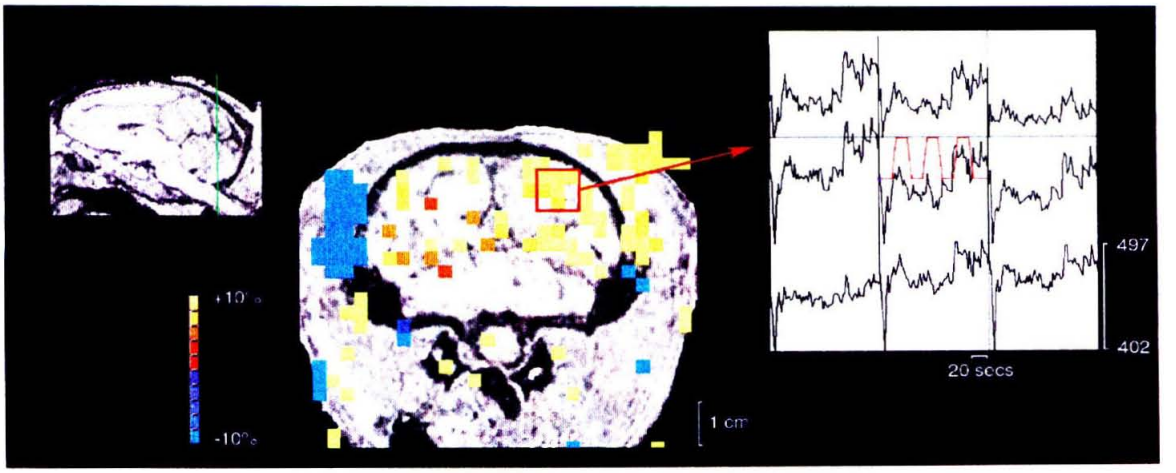

Figure A.7 Functional MRI study of a monkey taking a sip of water every 20 seconds while in the dark. The pharyngeal motion associated with swallowing produces gross motion-correlated artifact simulating activation in the visual cortex. The plane of section is indicated by the green line on the sagittal image. The inset graph shows the time-course of the MR signal for 9 voxels in visual cortex.

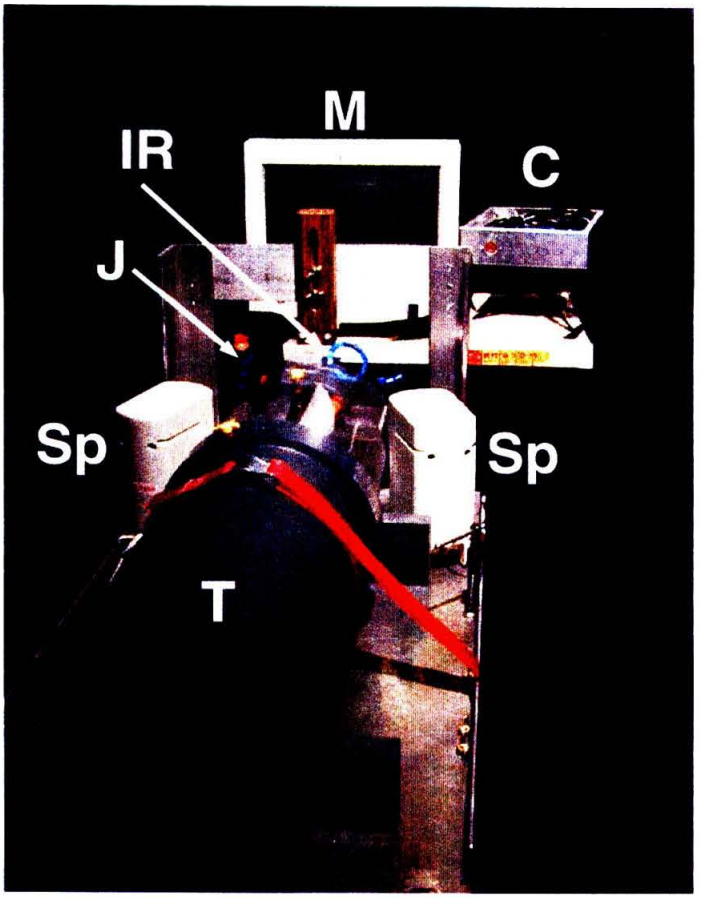

Figure A.8 Training rig for monkey functional MRI. The monkey lies in the same tube (T) used in the MRI and views a visual stimulus on the monitor (M). Eye position is tracked by means of an infrared eye illuminator (IR) and video camera (C). Gradient noises identical to those used in the scanner are played through the loud speakers (Sp). At the end of each simulated imaging run, the gradient noise ceases and the monkey is rewarded via the juice tube (J) for a successful task.

This highlights the need to withhold the juice reward until the conclusion of each functional MRI experiment. The monkey also needs to be trained not to salivate and swallow during the study. To achieve this the training rig was equipped with speakers to

play the gradient waveform noise from the MRI study. The monkey was trained only to expect a juice reward for a correctly executed trial when the gradient noise finished.

A.3 Eye-tracking Design

For the experiments described in Chapters 2 and 3 the monkey was free to view the stimulus without the need for fixation. These highlighted a number of key visual cortical areas that are shared between monkeys and humans. For more detailed studies (including the study presented in Chapter 4) more rigorous behavioral control is needed. At its simplest, this may just involve ensuring that the monkey is fixating where he is expected to. As most functional MRI studies last a minute or longer, it is necessary to train the monkey to fixate for extended periods of time. To achieve this, a feedback system was designed that monitored the animals eye position and provided him a fruit-juice reward if he maintained fixation for the duration of the study. To implement this inside the MR scanner it was necessary to design an eye-tracking system that could operate in a strong magnetic field, that was contained inside a Faraday cage (to limit radio frequency noise), and that illuminated the eye in the near infrared range (so that the illumination itself was invisible to the animal and would not confound any visual stimulus). Video eye-tracking was done using a commercially available video charged coupled device (CCD) camera with good sensitivity in the infrared range (λ = 880 nm). Processing of the video signal was done using a commercially available digital signal processing card (Iscan, Cambridge, MA). The video camera could not operate in the strong magnetic field within

the scanner bore, so additional optics were designed to allow it to operate some distance away. Three 2x converter lenses were added to the optical path to allow the camera to be sited at a safe distance 4 feet from the bore of the scanner. The camera and power supply were housed in a copper box to screen RF interference generated by the camera. Illumination of the eye needs to be imperceptible to the experimental subject. Lighting in the visible range could not achieve this, so I designed a system for remote illumination in the near infrared range.

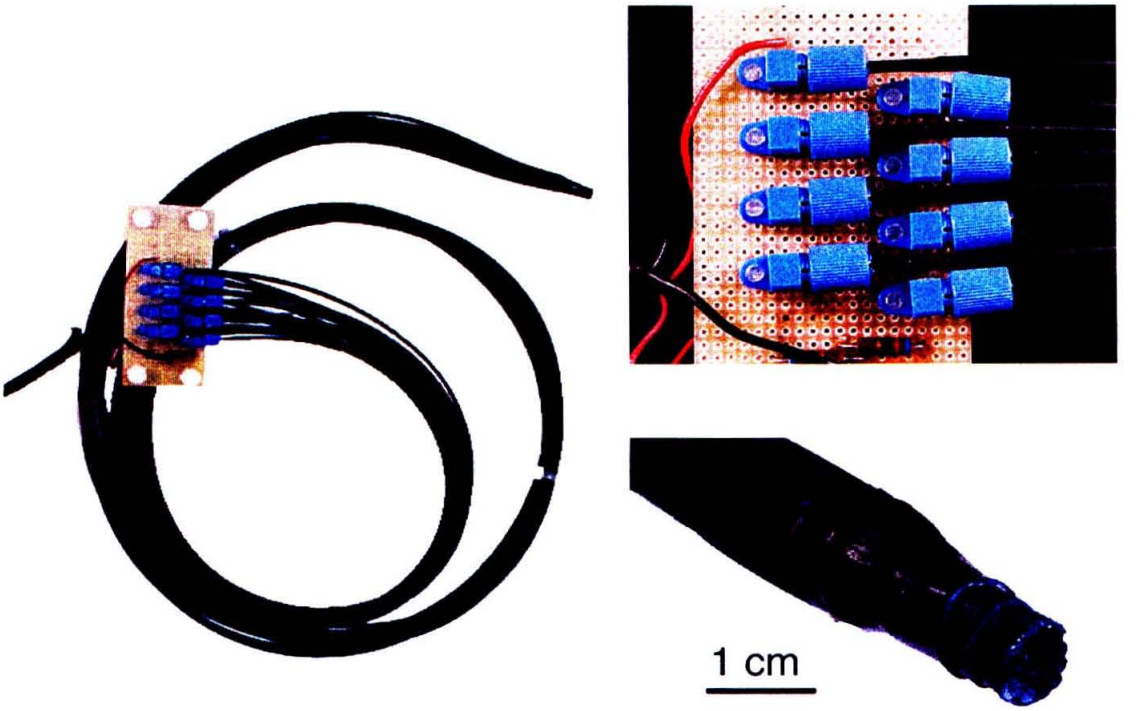

Figure A.9 Sixteen-core fiberoptic eye illuminator. Each fiberoptic cable is illuminated by a single 880 nm infrared LED driven at 50 mA. Inset (upper panel) are details of one side of the LED-fiber interface and (lower panel) of the final fiber bundle.

The initial design used fiberoptic delivery of the light to the eye via telecommunication infrared light-emitting diodes (LED). Housing the LED's outside the bore of the scanner allows more scope over the choice of LED (as only a very limited number are free from ferromagnetic parts and are safe inside the MR scanner). An early design based on a fiberoptic bundle of sixteen 1 mm cables illuminated via 16 880 nm telecommunication LED's is shown in Figure A.9. The lighting of the cornea was not optimal. The illumination was heterogeneous, and provided only limited contrast for the digital signal processing hardware (strong illumination is needed as there is an 8-fold attenuation in luminance by the three 2x converter chain in the CCD camera). For training the monkey accurate data was needed from the eye-tracking system so that the animal could be appropriately rewarded. Any errors or ambiguities by the eyetracker made training the monkey impossible. The inhomogeneous and low illumination was not adequate for monkey eye-tracking, although this system was sufficient for use in human subjects, particularly where the eye-tracking is only needed to confirm a correct response[3,4] — not as part of a training feedback loop (Figure A.10).

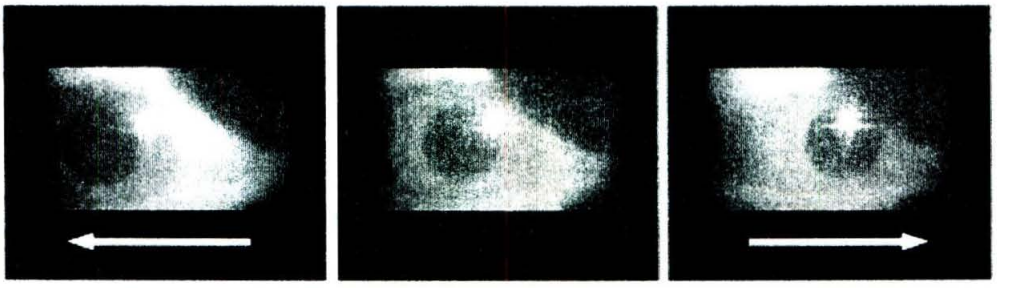

Figure A.10 Eye illumination of a human subject using the fiberoptic illuminator in Figure A.9. Note inhomogeneous illumination of sclera (varies with direction of gaze) and obscured view of the eye medially by the fiber bundle.

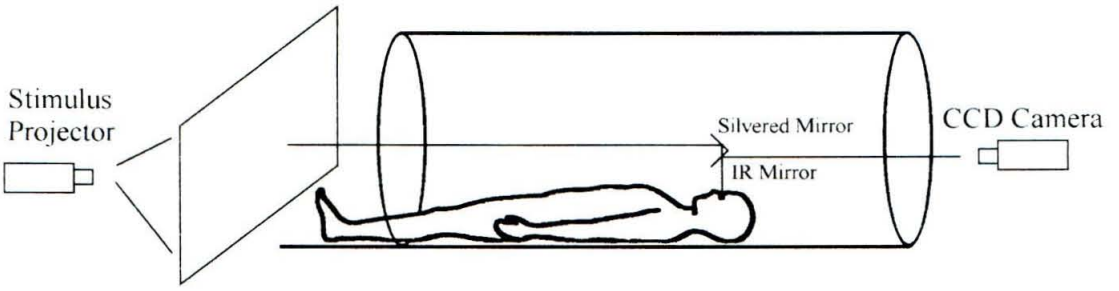

Figure A.11 Co-mounted fully silvered and semi-silvered mirrors 90° apart for human eye-tracking inside an MRI scanner.

For human eye-tracking, a dedicated mount was made to fit onto the 26 cm birdcage receive/transmit coil used for MRI. This contained co-mounted semisilvered and fully silvered mirrors fixed 90 degrees to each other, which ensured that the infrared and visual light shared a common optical path through the scanner (see Figure A.11). The fully silvered mirror reflected the visual stimulus so it could be readily viewed by a supine subject. The semisilvered mirror was imperceptible to the subject, and transmitted the visible light of the stimulus but reflected the infrared light of the illuminated eye (Figure A.12).

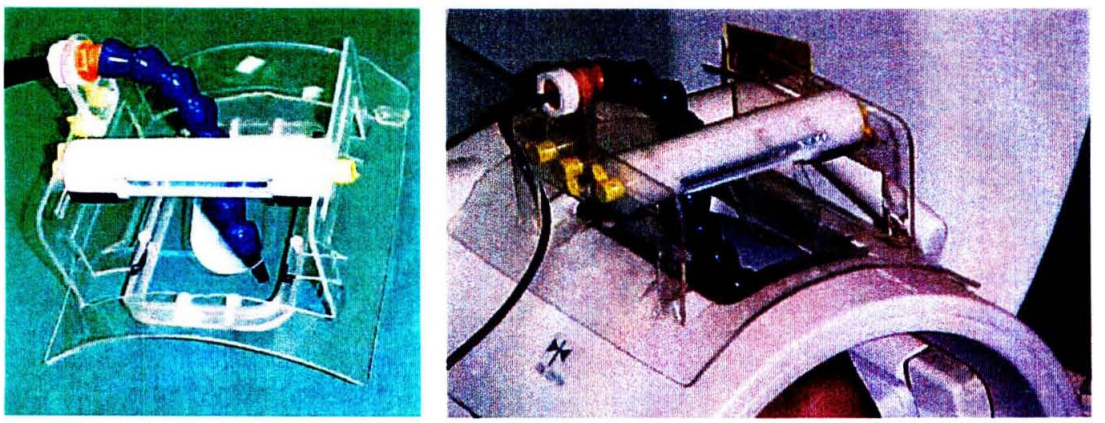

Figure A.12 Details of co-mounted mirrors, and fiberoptic illuminator (left). Attachment of mirrors to the 26 cm head coil in MR scanner (right).

The CCD camera was positioned at the head of the scanner and the visual stimulus was positioned at the foot (Figure A.11). At the start of the experiment, a central fixation dot was illuminated on the screen and a second light illuminated on the video camera (which was just visible as a reflection in the semi-silvered mirror). The subject adjusted the pair of mirrors until the two illuminated dots were superimposed. No further adjustment of the viewing stimulus, or the camera was then necessary.

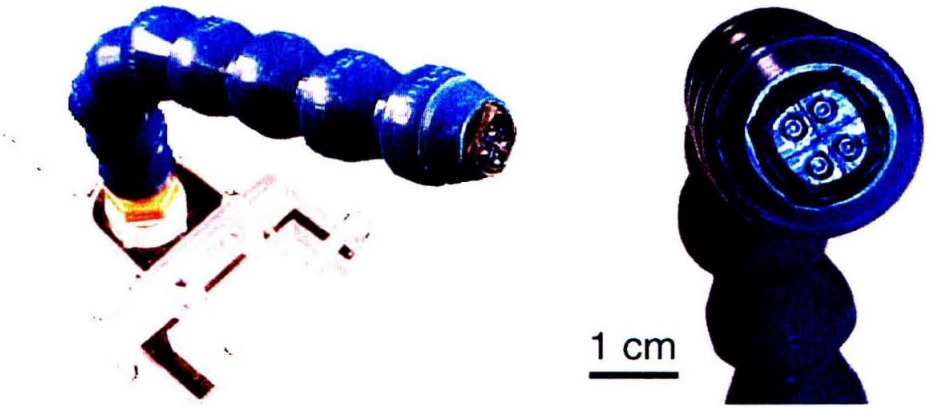

Figure A.13 Intermediate design using direct illumination with four LED's

For monkey training, a brighter and more homogeneous light source was needed. A preliminary design is shown in Figure A.13. Four MRI compatible infrared LED's were mounted on a flexible arm. This provided much better illumination that the fiberoptic array, but illumination was still inhomogeneous.

Figure A.14 shows the final design for illuminating the monkey's eye. A ring of 28 MRI-compatible LED's surround the eye. This provides good luminance and homogeneous

illumination (Figure A.15) allowing eye-tracking to a resolution of 1° of arc. One problem with a ring it that is does limit the animal's visual field of view to about ± 25°. For the experiments presented here, this was not a constraint.

Figure A.14 Ring arrangement of infrared LED's for homogeneous illumination

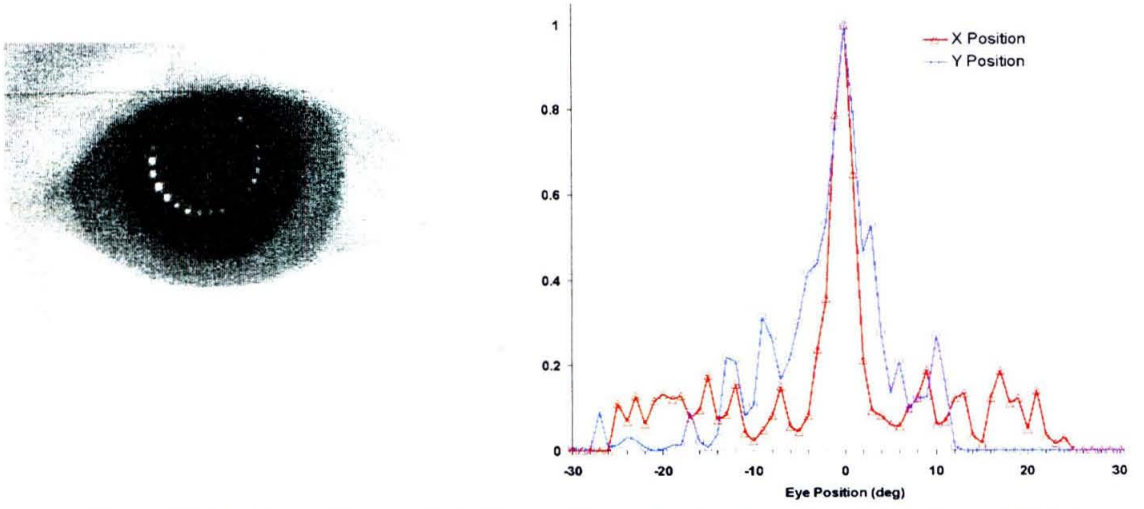

Figure A.15 (Left) Good quality homogeneous illumination of a monkey eye. (Right) Histogram of eye position during 25 second fixation task (note good fixation to within 4° of arc). Some jitter persists in the y direction which is exacerbated by eyelid drooping.

A.4 References

1. Schenck, J. F. The role of magnetic susceptibility in magnetic resonance imaging: MRI magnetic compatibility of the first and second kinds. *Med. Phys.* **23**, 815-50 (1996).

2. Van Kylen, J., Jesmanowicz, A., Wong, E. C. and Hyde, J. S. Material influenced susceptibility-induced phase shifts. *Proc. of Int. Soc. Magn. Res. Med.* **1**, 762 (1995).

3. Dubowitz, D. J., Martinez, A. and McDowell, J. A simple setup for tracking eye position during fMRI. *Proc. of Int. Soc. Magn. Res. Med.* **3**, 1691 (1999).

4. McDowell, J. E. et al. Neural correlates of refixation saccades and antisaccades in normal and schizophrenia subjects. *Biol. Psychiatry.* **51**, 216-23 (2002).

Appendix B Towards Combined Functional Magnetic Resonance Imaging and Electrophysiology

One critical step in comparing electrophysiological recordings with either functional or anatomical MRI is to ensure accurate co-registration of the recording electrode and MR images. One approach to this is to perform the two investigations contemporaneously[1]. This has the advantage of directly visualizing the position of a recording electrode on the MR images, but as discussed earlier, puts tremendous technical constraints on both the MR imaging and the electrophysiology.

A more straightforward approach which ensures the cleanest possible electrical signals for electrophysiology and minimizes susceptibility artifacts on MR imaging is to perform both measurements under similar behavioral conditions — but independently. For this to succeed, accurate co-registration is critical.

For precise localization, a number of stereotaxic references and frames exist for both human and primate work[2,3]. A first step in co-registering the MRI and electrophysiology techniques is to get the MR images into a standard stereotaxic co-ordinate frame. The method for this, based on bony landmarks, has changed little since its initial description in the early 1900s[4]. Previous investigators have simply remanufactured conventional stereotaxic frames out of plastic materials for MR compatibility[5,6]. While simplistic in its approach, the necessity for rigid bony fixation of the head requires deep anesthesia,

which is incompatible with functional MRI. In the first section of this appendix, I describe a frameless method I have developed for this, in which the position of the animal within the MRI is arbitrary, and the images are rotated into the correct plane. This allows localization of MRI landmarks onto the animal's surface anatomy, thus facilitating accurate surgical placement of recording hardware. Accuracy of MRI co-ordinates was compared with traditional stereotaxic frame co-ordinates using MR compatible fiducial markers.

The next requirement is to ensure accurate co-registration of recording hardware and MR images. The second section describes a novel frameless stereotaxic method localized on the electrophysiology recording chamber. Using a custom-designed cap for the chamber which is filled with gadolinium contrast agent, the images can be rotated to align exactly with the brain as viewed by an advancing recording electrode.

B.1 Frameless Stereotaxic Alignment of MR Images

The co-ordinate frame for stereotaxic positioning is based on having the animal head oriented so that Reid's plane is horizontal. Reid's plane (also referred to as the Frankfurt plane or the anthropological baseline) is a plane joining the inferior orbital margin and top of the bony external auditory canal. These osseous landmarks are readily visible on MRI, so it is possible to transform the MR image into his orientation with simple 3-dimensional rotation (irrespective of the animal's actual orientation in the MR scanner). The standard position for stereotaxic zero is then defined midway between the external

auditory meati (where Reid's plane intersects the mid-sagittal plane). Reid's plane seen on a sagittal MR image and on a corresponding skull, which is shown in Figure B.1

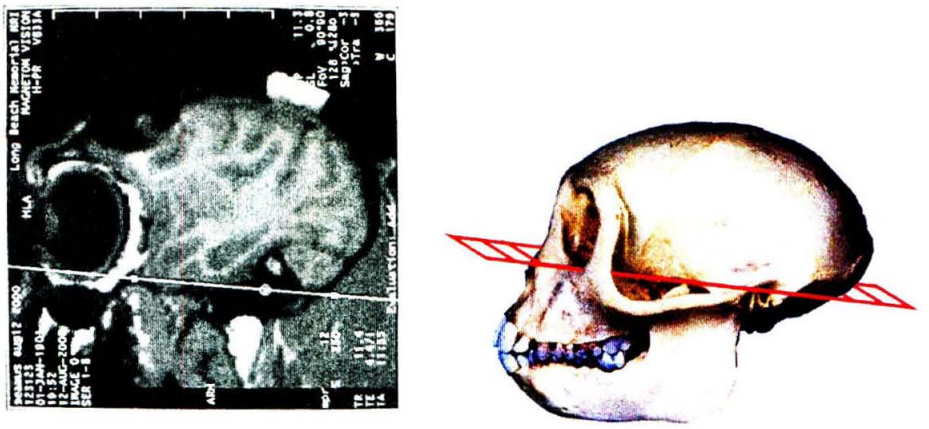

Figure B.1 The left image is Reid's plane joining the inferior orbital margin and bony external auditory meatus as seen on MRI. The MR image is then rotated so that this plane is horizontal. The plane is superimposed on a macaque monkey skull on the right.

The bony external auditory meatus has an oblique orientation. The position along the external auditory meatus, which is used to define stereotaxic zero, needs to correspond to the tips of the meatal ear bars – so that measurements made using a traditional frame and MRI would coincide. The meatal bars barely protrude beyond the opening of the bony canal, but this can be a difficult anatomical position to define. Plain film radiography of the bars insitu was used to define this end point more accurately. Figure B.2 shows a skull radiograph and the position of the bars indicated on the skull base. The temporo-mandibular joint is readily visible on MRI and is a robust anatomical landmark. The medial portion of the bars corresponds to the junction of the lateral third/medial two-thirds of the temporo-mandibular joint. This was found to be a much easier landmark to identify on MRI than the opening of the bony canal.

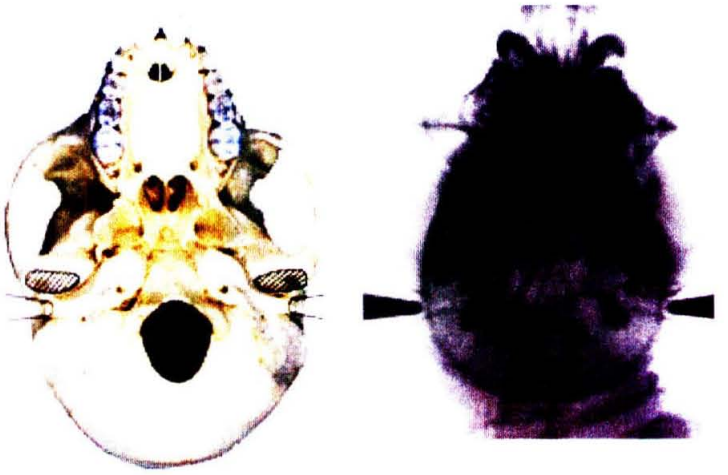

Figure B.2 The left image shows the position of the meatal bars of the stereotaxic frame relative to the temporo-mandibular joint (indicated by the shaded area). The position of the tip of the meatal bars is determined from the skull radiograph on the right. The medial ends of the bars lie just inside the opening of the bony external auditory meati. This corresponds to the junction of the lateral third/medial two-thirds of the temporo-mandibular joint.

The accuracy of the frameless MRI stereotaxic technique was assessed by comparing the position of a number of fiducial markers, and custom-blown glass beads (filled with 5 mm gadopentate dimeglumine MR contrast agent). The markers are shown in Figure B.3.

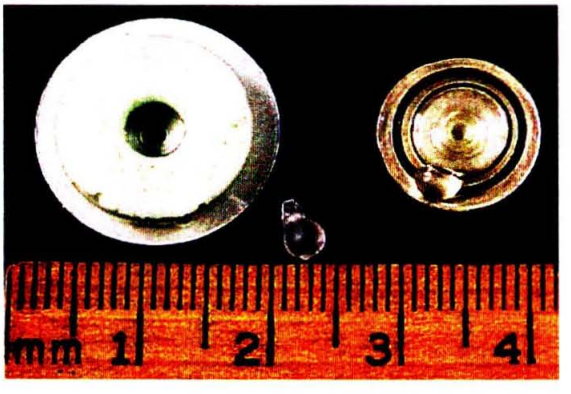

Figure B.3 Fiducial markers filled with gadopentate dimeglumine MR contrast agent. Conventional adhesive stereotaxic fiducial markers were used as skin markers and hand-blown glass bead were embedded in the polymethylmethacrylate headcap.

These were attached to the monkey's head or embedded in the polymethylmethacrylate headcap. The position of 7 fiducial markers (in 2 monkeys) was measured using a standard neurosurgical stereotaxic frame (Kopf Instruments, CA) and the MRI technique described above. The difference in stereotaxic measurement between the stereotaxic frame and MRI images is shown in Figure B.4. The errors (in mm) between the two techniques are shown for the 3 cardinal planes.

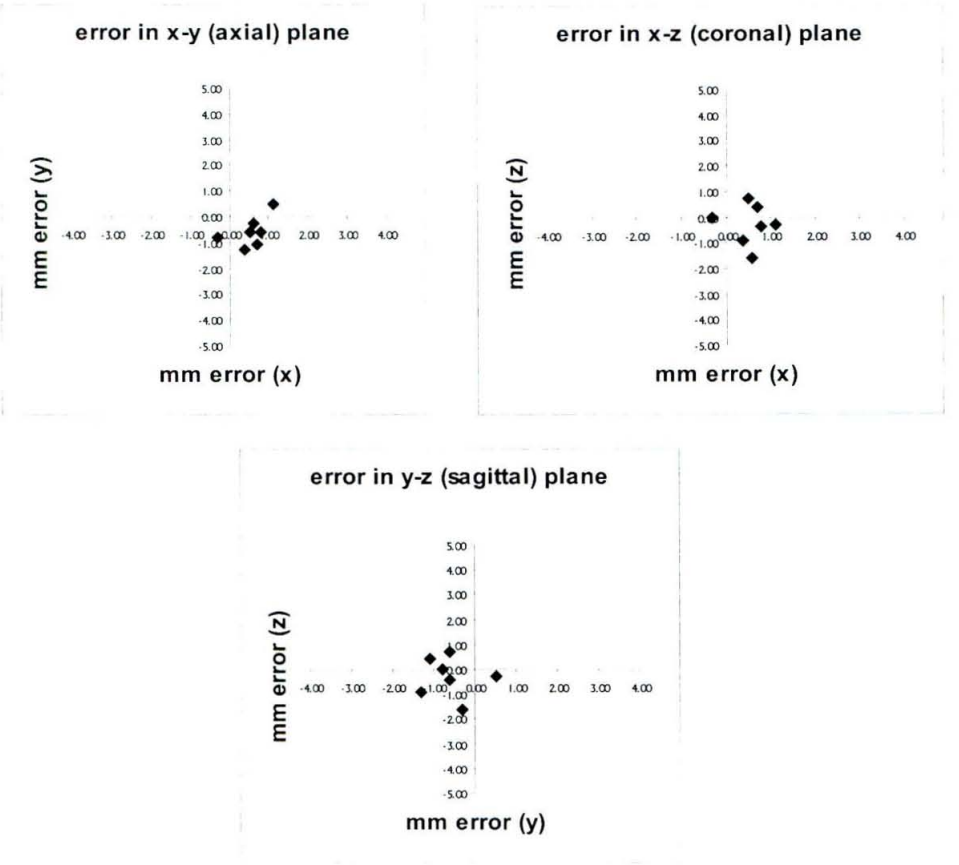

Figure B.4 Error in stereotaxic measurement in the 3 cardinal planes between a conventional stereotaxic frame and the frameless MRI technique for 7 fiducial markers. Mean error (expressed as the Euclidean distance of the offset) was 1.3 mm (S.D. 0.3 mm).

The Euclidean distance was calculated for each error measurement. Mean Euclidean offset was 1.3 mm (standard deviation 0.3 mm). This provides accurate MR localization for surgical placement of imaging and recording hardware. The recording chambers used have an internal diameter of 17 mm, so an accuracy of 1.3 mm provides ample precision with which to ensure the recording electrodes will lie over a predetermined area of cortex. The (0,0,0) origin of the MR image is set to align with the origin of the stereotaxic frame. Stereotaxic co-ordinates for any part of the brain can thus be read straight off the MR image (Figure B.5)

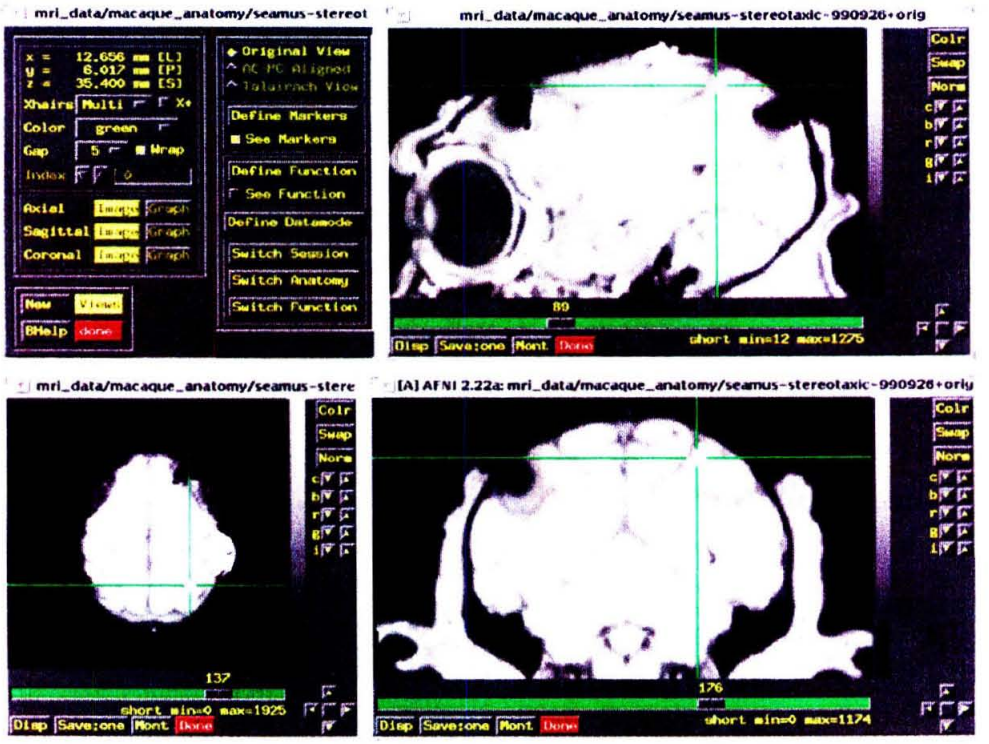

Figure B.5 AFNI[7] display of MRI of macaque brain oriented in stereotaxic co-ordinates. Cross hairs indicate lateral intraparietal area. Stereotaxic co-ordinates (12.7, 6.0, 35.4) can be read directly off the image (at top left corner). Susceptibility artifacts are from titanium screws used in the monkey's headcap (see Figure A.5)

B.2 Co-registration of Electrophysiology Recordings and MRI

For comparing electrophysiological recordings with MRI, higher fidelity is needed than can be achieved using bony landmarks. For this we need to define a new co-ordinate frame. For simplicity, I chose this relative to the recording chamber. This has the advantage that the recording electrode micro-positioning vernier already uses this as a reference, and only the rotation about the recording chamber needs to be controlled. This co-ordinate frame is shown in Figure B.6. *Z* is electrode depth, *X* is left-right and *Y* is anterior-posterior. It is not necessary for the co-ordinate frame to align to true stereotaxic co-ordinates, as this is not needed for electrode placement. However, in practice any area of cortex can be represented in both co-ordinate frames.

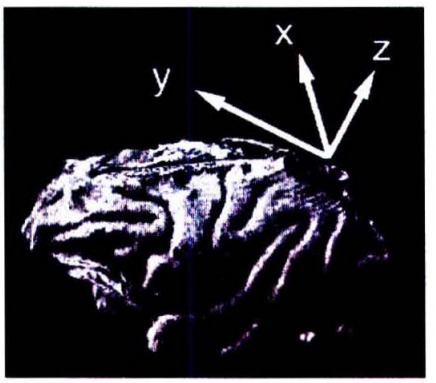

Figure B.6 The co-ordinate frame for MRI positioning of electrodes is defined relative to the recording chamber.

To allow rotation of the MR dataset cardinal axes into the same orientation as the recording chamber, a fiducial indicator was built into the cap of the recording chamber. A

preliminary design for this used a single blind-ending channel adjacent to the central hole of the cap. Both the chamber and central hole as well as the blind channel were filled with 0.5 mm gadopentate dimeglumine for MRI conspicuity. The polar orientation of the electrode positioning head as well as the cap use the same scribed detent on the recording chamber, so that both are aligned in the same orientation. This is shown in Figure B.7

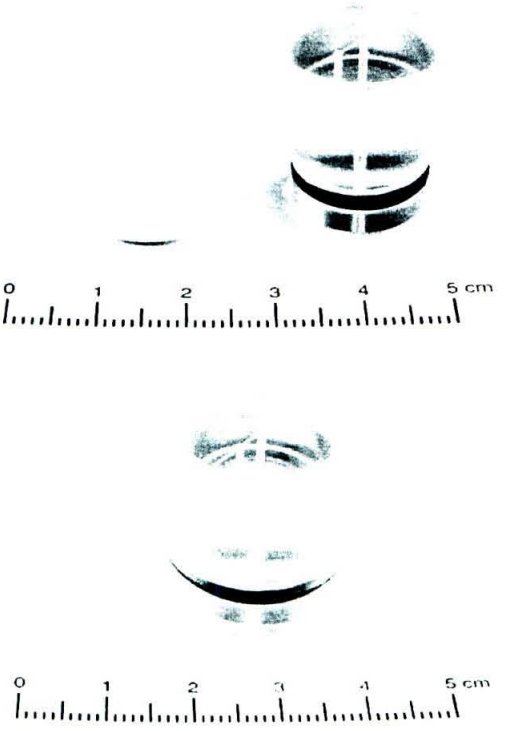

Figure B.7 Chamber and cap used to co-align the electrode positioning head and MR images. The polar orientation is fixed by the détente on the chamber rim.

In Figure B.8, an orange is used as a phantom to image the chamber and cap. The interior of the chamber, central channel and offset blind channel are highlighted by the MR contrast agent. With time the contrast agent dissipates from the chamber (see pooling of contrast agent on the undersurface of the orange). This leaves some ambiguity as to the orientation of the cap.

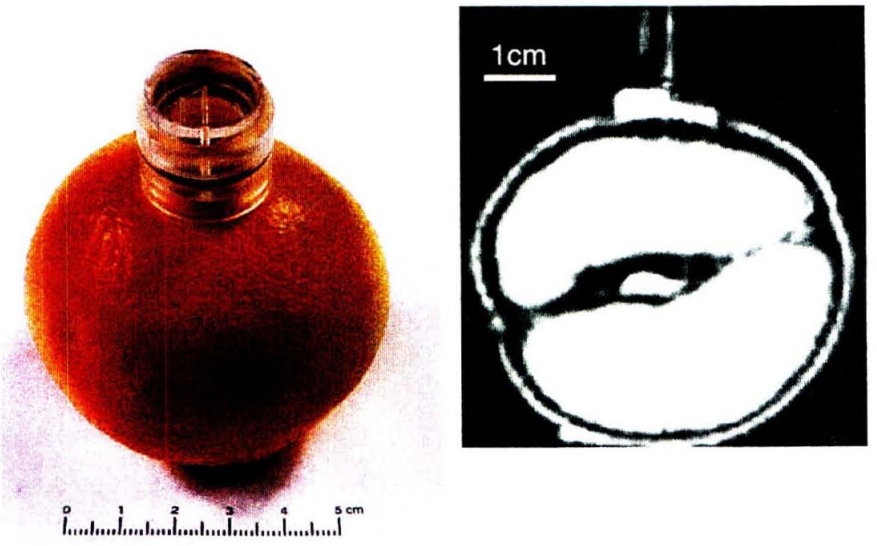

Figure B.8 Orange phantom and gadolinium-filled chamber and cap. The interior of the chamber as well as the central and blind channels of the cap are outlined with contrast agent. The image has been rotated to align with the cap. This is itself aligned with the chamber, thus the image is a true sagittal relative to the chamber. Some ambiguity of the orientation of the image exists once the contrast agent dissipates from the central channel. (MPRAGE image — see Table 3.1 for imaging parameters.)

A more reliable design is shown in Figure B.9, which used 2 blind channels, whose orientation remained unambiguous even when the central channel emptied.

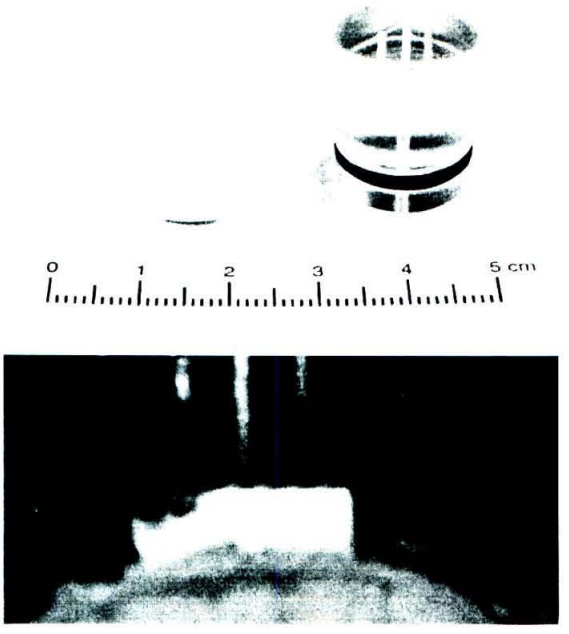

Figure B.9 Improved design using 2 blind channels. The lower image is a MPRAGE image (see Table 3.1 for imaging parameters) of the chamber positioned over parietal cortex. The image has been rotated to align with the chamber and is thus a true sagittal image in chamber co-ordinates.

As with the frameless stereotaxic method, the (0,0,0) origin of the MR image is set to align with the center of the chamber. The z-origin is defined at the dural surface. Stereotaxic co-ordinates can thus be read straight off the MR image.

To assess the accuracy of this technique, comparative measurements of electrode position were made using the electrode positioning head, and by reconstructing the electrode tract

visible on T_2* weighted images (Figure B.10). Accuracy in the z-direction (depth) was not compared, as the MR image of electrode tract provides no indication of z-position.

Figure B.10 Electrode tract visible on T_2*-weighted MRI 24 hours after electrode recording in parietal cortex. (MPRAGE image — see Table 3.1 for imaging parameters.)

The electrode position within the chamber was recorded from the vernier gauge of the positioning head (confirmed by allowing the electrode to pass through a sheet of paper covering the recording chamber opening and directly measuring the *x-y* position). The MRI position was read directly off the images. Errors between the electrode position and MR images was plotted in the *x-y* plane for 11 electrode penetrations in 2 monkeys. The mean offset (expressed as a Euclidean distance) was 0.5 mm (S.D. 0.2 mm).

For practical purposes, the accuracy of this frameless co-registration is limited only by the imaging pixel resolution (for the MPRAGE sequences, this was 0.7 mm in-plane). This is considerably smaller than the pixel sizes used for functional MRI.

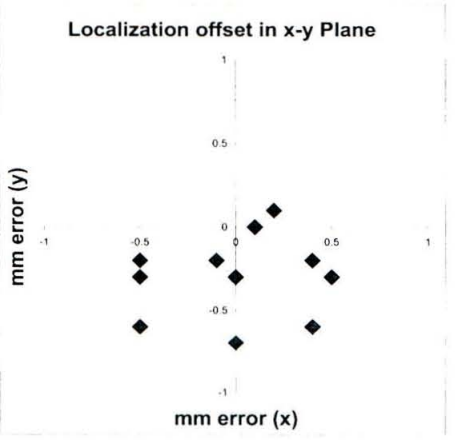

Figure B.11 Error in measurement of electrode position relative to the recording chamber in the *x-y* plane between the position of the electrode head and the frameless MRI technique. Mean error (expressed as the Euclidean distance of the offset) was 0.5 mm (S.D. 0.2 mm).

The method described here has been used for planning surgical placement of an electrophysiology recording chamber, and for accurately positioning recording electrodes in a specific area of cerebral cortex. It has also been used to reconstruct the location of electrode recording tracts from the small amount of hemoglobin left in the tract acutely, or the gliosis associated with prolonged electrode recordings. For more accurate reconstruction of the exact position of the electrode tip, a method was developed using a steel electrode, in which a small amount of iron is deposited into the brain following passage of a small current through the electrode. The position of the electrode tip is then readily apparent on susceptibility weighted imaging sequences due to the iron deposition. An example of this is shown in Figure B.11. The small deposits (about 100–200 μm in diameter) cause a blooming artifact on fast gradient echo MR images, and are apparent following 4–8 μA current for 20–80 seconds. Electrode tracts were successfully reconstructed using this method *ex vivo* in bovine brain and *in vivo* in rabbit and monkey brain[8].

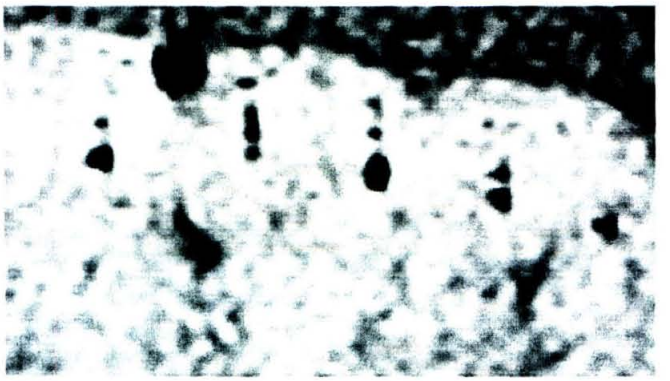

Figure B.12 Iron deposition in ex vivo bovine brain at 1 mm intervals along the electrode tract using 3D-FLASH MRI. Imaging parameters: TR = 25 ms, TE = 11 ms $\alpha = 20°$, 0.4 mm isotropic resolution. Current was generated by a stable unipolar current source. Current and times are given below.

Tract	1	2	3	4	5
Current (μA)	4	4	4	4	4
Time (s)	160	80	4	20	10

Table B.1 Parameters for iron deposition lesions 1–5.

B.3 References

1. Logothetis, N. K., Pauls, J., Augath, M., Trinath, T. and Oeltermann, A. Neurophysiological investigation of the basis of the fMRI signal. *Nature* **412**, 150-7 (2001).

2. Talairach, J. and Tournoux, P. *Co-planar stereotaxic atlas of the human brain* (Thieme, New York, 1988).

3. Paxinos, G., Huang, X.-F. and Toga, A. W. *The rhesus monkey brain in stereotaxic coordinates* (Academic Press, London, 1999).

4. Horsley, V. A. H. and Clarke, R. H. The structure and function of the cerebellum examined by a new method. *Brain* **31**, 45-124 (1908).

5. Rebert, C. S., Hurd, R. E., Matteucci, M. J., De LaPaz, R. and Enzmann, D. R. A procedure for using proton magnetic resonance imaging to determine stereotaxic coordinates of the monkey's brain. *J. Neurosci. Methods.* **39**, 109-13 (1991).

6. Alvarez-Royo, P., Clower, R. P., Zola-Morgan, S. and Squire, L. R. Stereotaxic lesions of the hippocampus in monkeys: determination of surgical coordinates and analysis of lesions using magnetic resonance imaging. *J. Neurosci. Methods.* **38**, 223-32 (1991).

7. Cox, R. W. and Hyde, J. S. Software tools for analysis and visualization of fMRI data. *NMR Biomed* **10**, 171-178 (1997).

8. Pezaris, J. S. and Dubowitz, D. J. MRI Localization of Extracellular Electrodes Using Metallic Deposition at 1.5 T. *Proc. of Int. Soc. Magn. Res. Med.* **2**, 968 (1999).

B.4 Acknowledgment

I am grateful to Will Higgs for kind permission to use his skull database (http://www-users.york.ac.uk/~wjh101/hedbone/index.htm) for Figures B.1 and B.2

Appendix C List of Abbreviations

α Flip Angle

λ Wave Length

3D FLASH 3-Dimensional Fast Low Angle Shot

BOLD Blood Oxygen Level-Dependent

CBF Cerebral Blood Flow

CBV Cerebral Blood Volume

CCD Charge Coupled Device

CNR Contrast-to-Noise Ratio

CPMG Carr Purcell Meiboom Gill

EEG Electroencephalogram

EPI Echo-planar Imaging

ERP Event Related Potential

fMRI Functional Magnetic Resonance Imaging

FOV Field of View

GE Gradient Echo

Hb Hemoglobin

im Intramuscular

IR Inversion Recovery

iv Intravenous

LED Light Emitting Diode

LIP Lateral Intraparietal Area

MEG Magnetoencephalogram

MPRAGE Magnetization Prepared Rapid Gradient Echo

MR Magnetic Resonance

MRI Magnetic Resonance Imaging

MRM Magnetic Resonance Microscopy

MST Medial Superior Temporal

MT Middle Temporal

MT+ Middle Temporal Complex

PET Positron Emission Tomography

R_1 Longitudinal Relaxation Rate

R_2 Transverse Relaxation Rate

RF Radio Frequency

ROI Region of Interest

S.D. Standard Deviation

S.E. Standard Error

SE Spin Echo

T Tesla

T_1 Longitudinal Relaxation Time Constant

T_2 Transverse Relaxation Time Constant

TE Echo Time

TE_{eff} Effective Echo Time

TEO Temporo-occipital Area

TI Inversion Time

TR Repetition Time

V1 Primary Visual (Striate) Cortex

V2, V3, V3A, V4, VP Supplementary Visual Cortical Areas